RICE UNIVERSITY

Autocorrelation Analysis of the Seismic Data Recorded on Mars

By

Sizhuang Deng

A THESIS SUBMITTED
IN PARTIAL FULFILLMENT OF THE
REQUIREMENTS FOR THE DEGREE

Doctor of Philosophy

APPROVED, THESIS COMMITTEE

ALAN LEVANDER

Alan Levander
Carey Croneis Professor, Department of Earth,
Environmental and Planetary Sciences

Adrian Lenardic
Professor, Department of Earth,
Environmental and
Planetary Sciences

Fenglin Niu
Professor, Department of Earth,
Environmental and
Planetary Sciences

Colin Zelt
Professor, Department of Earth,
Environmental and
Planetary Sciences

David Alexander
Professor, Department of Physics and Astronomy
Director, Rice Space Institute

HOUSTON, TEXAS

October 2022

RICE UNIVERSITY

Autocorrelation Analysis of the Seismic Data Recorded on Mars

by

Sizhuang Deng

A THESIS SUBMITTED
IN PARTIAL FULFILLMENT OF THE
REQUIREMENTS FOR THE DEGREE

[Doctor of Philosophy]

APPROVED, THESIS COMMITTEE

Alan Levander, Chair
Carey Croneis Professor, Department of Earth, Environmental and Planetary Sciences

Fenglin Niu
Professor, Department of Earth, Environmental and Planetary Sciences

Colin A. Zelt
Professor, Department of Earth, Environmental and Planetary Sciences

Adrian Lenardic
Professor, Department of Earth, Environmental and Planetary Sciences

David Alexander
Professor, Department of Physics and Astronomy

HOUSTON, TEXAS
October 2022

ABSTRACT

Autocorrelation Analysis of the Seismic Data Recorded on Mars

by

Sizhuang Deng

Mars, unlike Earth, lacks tectonic events since ~4 billion years ago, which indicates the understanding of Mars can provide more information about the planet formation and early history of the solar system. The InSight (Interior Exploration Using Seismic Investigations, Geodesy and Heat Transport) spacecraft landed on Mars on November 26, 2018 and installed the seismograph SEIS (Seismic Experiment for Interior Structure) to record continuous seismic data for approximately 3 years, providing opportunities to investigate this red planet's interior. Since only one seismic station is deployed on Mars, some seismological methods that require dense arrays cannot be used for SEIS data analysis. In this thesis, we employed autocorrelation method to analyze the continuous ambient noise data recorded by SEIS to recover two types of seismic phases, body-wave reflection response and Mars orbiting surface waves (R_2). Based on the two-way traveltimes of several reference 1-D velocity models, the reflection signals can be mapped to depth domain to estimate the depths of these seismic boundaries, including Moho (crust-mantle boundary), olivine-wadsleyite transition and core-mantle boundary. The reference upper mantle velocity model of Mars was updated iteratively by the Monte Carlo method to minimize the differences between synthetic and observed R_2 waveforms.

Chapter 1 is the introduction to show the ideas and summarize the results of this thesis.

Chapter 2 is edited, reformatted and reprinted from a paper published on *Geophysical Research Letters*.

Deng, S., & Levander, A. (2020). Autocorrelation Reflectivity of Mars. *Geophysical Research Letters*, *47*(16). https://doi.org/10.1029/2020GL089630

Chapter 3 is based on the manuscript that will be submitted to *Geophysical Research Letters*.

Chapter 4 is edited, reformatted and reprinted from a paper published on *Geophysical Research Letters*.

Deng, S., & Levander, A. (2022). Autocorrelation R2 on Mars. *Geophysical Research Letters*, *49*(17), e2022GL099580. https://doi.org/10.1029/2022GL099580

Chapter 5 is the conclusions to make the final statements about the seismic interior structures of Mars discovered in this thesis.

Acknowledgments

First, I would like to thank my advisor Dr. Alan Levander for his valuable comments and helpful guidance on my Ph.D research projects. I've acquired useful knowledge in many different areas, including computer programming, data processing, seismic interpretation, tectonic settings et al, from him. I remembered one afternoon in April or May 2019, he went to my office and told me that the InSight mission released the single-station seismic data recorded on Mars, which could be used to unveil the subsurface structures of Mars by autocorrelation methods. I have to say his short notice is the starting point of this long thesis. I would also like to thank my thesis committee member, Dr. Fenglin Niu, Dr. Colin A. Zelt, Dr. Adrian Lenardic and Dr. David Alexander for becoming my thesis committee member and providing constructive comments on my thesis.

I would like to express my gratitude to all colleagues at Rice University, including Ao Cai, Neng Xiong, Wenpei Miao, Hongrui Qiu, Benxin Chi, Jiayuan Han, Minglong Pan, Qinci Li, Luan C. Nguyen, John Cornthwaite, Mei Chien, Liwei Liu, Yangtianli Zhou, Boda Li, Wenbin Jiang, Yiying Wu, Chen Chen, Julin Zhang, Chenliang Wu, Yen Sun, Jonathan R. Delph. I enjoyed the research discussions with you and appreciated generous help on my personal life. I will always remember the great memories in these years. I would like to give a special thanks to Zhaoying Li and wish you all the best for the bright future. If I missed some names, please don't feel angry on me. It's just because of limited words in the acknowledgement session.

I would like to appreciate my manager Yuli Zhang, and four mentors, Huafeng Liu, Min Yang, Jane Huang and Ying Tan at Chevron. I enjoyed my life during my summer internship at Chevron. I am looking forward to starting my career at Chevron and working with you again. I also want to thank two Chevron recruiters Amanda Guzofski and Devon Verellen for their recommendations.

Lastly, I would like to appreciate my beloved family for their great support across the Pacific ocean during this long Ph.D journey. I am grateful for the help from my cousin Shun Liu and his wife Jie Li from UT-Southwest (UTSW) during my early career in United States.

This research was funded by Department of Earth, Environmental and Planetary Sciences at Rice University. The InSight seismic data recorded on Mars was collected from IRIS (Incorporated Research Institutions for Seismology) data center (https://www.iris.edu/hq/sis/insight).

Contents

List of Figures

List of Tables

List of Equations

Chapter 1

Introduction

There are eight planets in our solar system, which can be divided into two categories, terrestrial planets and Jovian planets (Figure 1.1a). Mars, the last terrestrial planet away from sun, is the target we want to investigate in this thesis. Mars has very thin atmosphere and ice caps in its polar areas (Figure 1.1b). Knowledge of the Martian interior informs theories for the formation and dynamic evolution of another terrestrial planet, hence providing information on the history of the solar system. The subsurface velocity structures of Mars have been investigated by thermodynamic modeling (Panning et al., 2017; Yoshizaki & McDonough, 2020) and the joint inversion of multiple geophysical datasets (Khan et al., 2018). These velocity models will be utilized for time-to-depth conversion of autocorrelation reflectivity series. The Martian dichotomy is observed on Mars by gravity inversion (Figure 1.2), where the Moho depth is shallower in the northern hemisphere (30-50km) and deeper in the southern hemisphere (70-90km) (Zuber, 2000). The InSight (Interior Exploration Using Seismic Investigations, Geodesy

and Heat Transport) spacecraft was landed near the Martian equator at the end of 2018, near the boundary between two distinct hemispheres (Figure 1.2). On Earth, subsurface structure is discovered by analysis of seismic signals recorded by large seismograph arrays deployed worldwide. The InSight lander carried one seismic station, named SEIS (Seismic Experiment for Internal Structure), to Mars, providing the opportunity to investigate the internal seismic structure of Mars (Figure 1.3). SEIS is equipped with six axes covering the seismic periods from 0.02s to 100s, three for long-period very broadband (VBB) recordings, and another three for short-period (SP) recordings (Lognonné et al., 2019). The seismometer is installed on the Martian surface by a robotic arm and protected by a wind and thermal shield (Lognonné et al., 2019). As only one station is deployed on Mars to record seismic vibrations, some tomographic and imaging methods based on seismic array analysis are not suitable to investigate Mars' data. In this thesis, we applied the autocorrelation method to retrieve two types of seismic phases, body-wave reflection signals and Mars orbiting surface wave signals. The body-wave reflection signal originated from subsurface interfaces of Mars can inform the depth range of these seismic boundaries, including Moho, olivine-wadsleyite transition and core-mantle boundary. As for Mars orbiting surface waves, it can be used to improve the velocity models of Martian upper mantle.

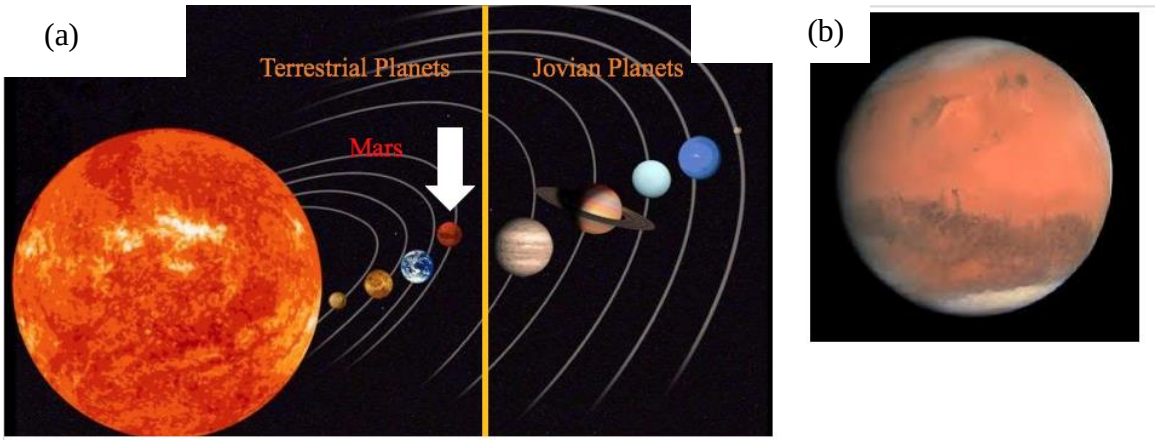

Figure 1.1 – (a) Schema of the solar system. The white arrow marks Mars. (b) A picture of Mars (from https://en.wikipedia.org/wiki/Mars)

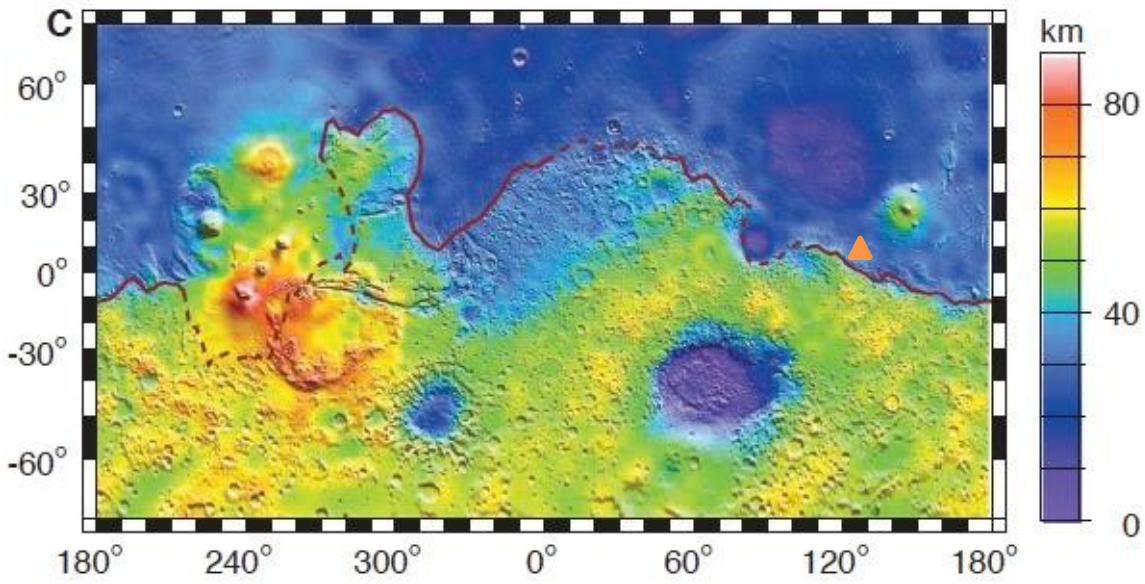

Figure 1.2 – Crustal thickness from gravity inversion (Zuber, 2000). The northern hemisphere has relatively thinner crust compared with southern hemisphere. The orange triangle marks the location of InSight spacecraft.

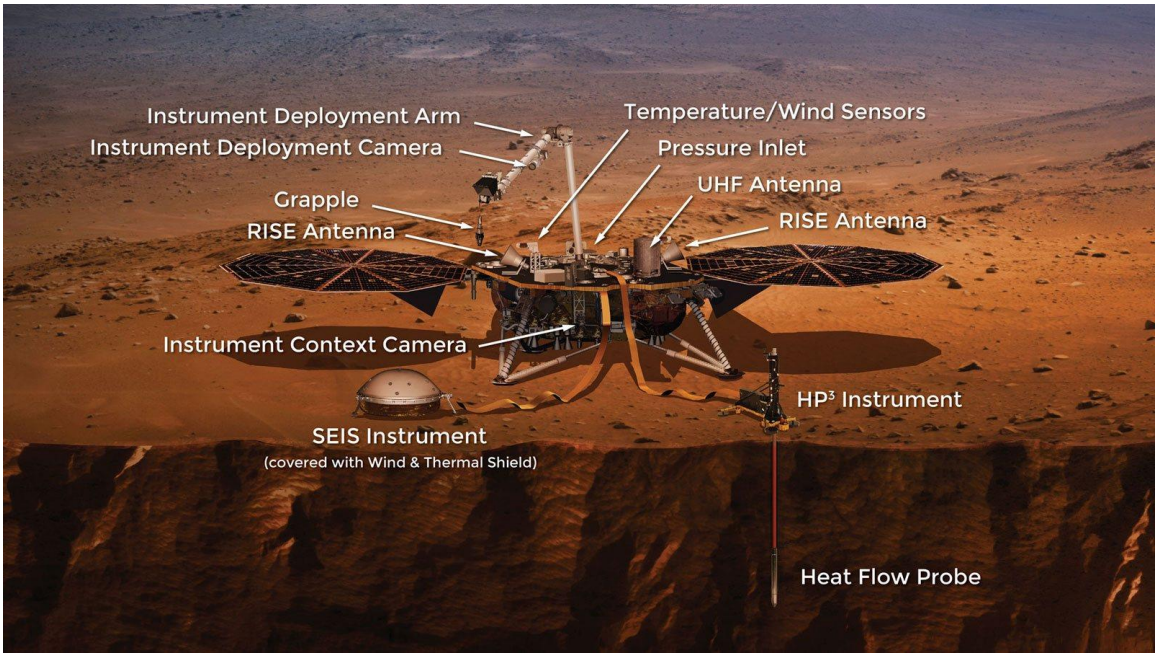

Figure 1.3 – A picture of InSight lander (from https://mars.nasa.gov/insight/spacecraft/instruments/summary/). It mainly contains three projects: (1) SEIS (Seismic Experiment for Internal Structure (2) HP^3 (Heat Flow and Physical Property Package) (3) RISE (Rotation and Interior Structure Experiment). This study analyzed the seismic data collected by SEIS

In Chapter 2, we autocorrelated ambient noise from the available seismic data to investigate the subsurface discontinuities of Mars. In the raw seismic data, we observe the long-period signals with a period of ~1 Martian sol (~3% longer than an Earth day), which are related to the diurnal variation in weather and tides. After the removal of instrument response, remaining high-amplitude peaks are likely caused by the daily

operations of the InSight lander. We preprocessed the raw data and used different frequency bands to detect discontinuities at different depths. We identify prominent signals in the stacked autocorrelation reflectivity as likely originating from the Martian Moho, the olivine-wadsleyite transition in the Martian mantle, and the core-mantle boundary. These results are consistent with other observations and measurements.

However, some analysis suggested that the arrival times of olivine-wadsleyite transition and core-mantle boundary coincide with the recurrence time of high-amplitude glitches within raw seismic data, leading to the bias interpretation of low-frequency autocorrelation results. In Chapter 3, to resolve the contradiction, we detected and removed these high-amplitude glitches before further processing of ambient noise data. The autocorrelation analysis of deglitched continuous vertical-component waveforms can still recover the signals originating from olivine-wadsleyite transition and core-mantle boundary, but glitch-only waveforms cannot, which indicated the observed signals from low-frequency autocorrelation are from real seismic discontinuities rather than high-amplitude glitches within raw data. We found a 1-layer transition zone model with 60km thick at Martian core-mantle boundary can better fit the observed PcP phase.

In Chapter 4, we preprocessed the continuous vertical-component seismic data, and by autocorrelation retrieved a Rayleigh wave, one class of seismic surface wave, that orbits Mars. The Rayleigh wave group velocities between 115 and 200s period were extracted from the observed Mars orbiting Rayleigh waves. Synthetic seismograms were calculated using current estimates of the velocity structure of Mars for comparisons to the observation. The spherically symmetric model was updated with a Monte Carlo algorithm, an inversion method that randomly perturbs the velocity model and determines

the model that best matches the Mars orbiting surface waves through trial and error. An S-wave low-velocity zone is observed to the depth of ~400km beneath the Martian surface, consistent with other InSight seismic observations and velocity models measured from geophysical modeling and high-pressure laboratory experiments.

Chapter 2

Autocorrelation Reflectivity of Mars

The seismic structure of the Martian interior can shed light on the formation and dynamic evolution of the planet and our solar system. The deployment of the seismograph carried by the InSight mission provides a means to study Martian internal structure. We used ambient noise autocorrelation to analyze the available vertical component seismic data to recover the reflectivity beneath the Insight lander. We identify the noise that is approximately periodic with the Martian sol as daily lander operations and the diurnal variation in Martian weather and tides. To investigate the seismic discontinuities at different depths, the autocorrelograms are filtered and stacked into different frequency bands. We observe prominent reflection signals probably corresponding to the Martian Moho, the olivine-wadsleyite transition in the mantle, and the core-mantle boundary in the stacked autocorrelograms. We estimate the depths of these boundaries as ~35km, 1110-1170 km, and 1520-1600 km, consistent with other estimates.

2.1. Introduction

The InSight seismograph, SEIS (Seismic Experiment of Internal Structure), gives us the ability to investigate the interior structure of another inner planet in the solar system (Smrekar et al., 2019). Martian subsurface structures have been studied at different scales during past decades by gravity anomaly inversion (Kiefer et al., 1996; Neumann et al., 2004; Parro et al., 2017; Zuber, 2000), solar tide detection (Yoder et al., 2003), high-pressure experiments (Bertka & Fei, 1997; Fei, 2013; Stewart et al., 2007) and thermoelastic model calculation and inversion (Khan et al., 2018; Khan & Connolly, 2008; Rivoldini et al., 2011; Sohl & Spohn, 1997; Zharkov et al., 2009). Mars, with a similar interior structure to Earth, can be divided into crust, mantle and core (Smrekar et al., 2019). The Viking 2 seismic recordings provided modest information on the interior structure of the planet (Anderson et al., 1977) which has led to numerical and theoretical estimation of seismic properties prior to the InSight mission (Lognonné et al., 2019; Panning et al., 2017). Hundreds of Mars-quakes have been recorded by the SEIS instrument (Banerdt et al., 2020; Giardini et al., 2020; Lognonné et al., 2020). Estimates of crustal thickness have been made from gravity observations, which among other observations suggests a dichotomy between the northern and southern hemispheres (Genova et al., 2016; Parro et al., 2017; Zuber, 2001). Evidence that Mars' core is largely liquid has been demonstrated by the large k_2 Love number (Rivoldini et al., 2011; Yoder et al., 2003), and high-pressure experiments using assumed core properties (Stewart et al., 2007), while the existence of a solid inner core is still unknown.

The autocorrelation $A(t)$ of a time series $s(t)$ represents the correlation of the signal with a delayed copy as a function of delay time lag, which is defined as

$$A(t) = \int_{-\infty}^{\infty} s(\tau + t)s(\tau)d\tau$$

Equation 1 – The equation for autocorrelation calculation

Claerbout (1968) showed that the reflectivity series of an acoustic media can be recovered by taking the autocorrelation of the normal-incidence transmission response, a form of seismic interferometry, that was subsequently extended to elastic media and non-normal incidence angles by Frasier (1970). Body-wave reflection phases have been successfully extracted by crosscorrelating (Clayton, 2020; Feng et al., 2017; Lin & Tsai, 2013; Tkalčić & Pham, 2018; Zhan et al., 2010) and autocorrelating (Becker & Knapmeyer-Endrun, 2018, 2019; Phạm & Tkalčić, 2018; Romero & Schimmel, 2018) the seismic wavefield. Most recent studies have focused on the extraction of Moho-reflected phases (e.g., PmP and SmS) to determine crustal thickness by autocorrelating and stacking the ambient noise record (Gorbatov et al., 2013; Oren & Nowack, 2017; Tibuleac & von Seggern, 2012) or teleseismic earthquake data (Delph et al., 2019; Phạm & Tkalčić, 2017). Besides the Moho discontinuity, stacked ambient noise autocorrelations have been used to study the reflectivity of the lithosphere and lithosphere-asthenosphere boundary (LAB) (Kennett, 2015; Kennett & Sippl, 2018). The cross-correlation of continuous noise data (Lin et al., 2013) and autocorrelation of earthquake coda waves (Wang et al., 2015) have been used to identify core phases.

The successful applications of single-station-based autocorrelation to studying Earth's interior show its potential for determining subsurface structures using the single seismometer available on Mars. In this work we calculated and stacked the Z-component autocorrelograms to determine the depth of subsurface interfaces beneath the SEIS station using the continuously recorded ambient noise data. The reflection responses at different depths are identified by applying different bandpass filters to the seismic data. We depth convert the reflection sequence in time using theoretical models of the 1D Martian interior to provide approximate depths to Martian seismic discontinuities.

2.2. Data and Methods

The InSight ambient noise seismic data were downloaded from IRIS (Incorporated Research Institutions for Seismology) data center in BHU-V-W channels. The U-V-W are three non-orthogonal directions, where the dip and azimuth information can be found in Compaire et al. (2021). The data, sampled at 10 Hz, were collected by SEIS from February thru August 2019, where the instruments were protected by the wind and thermal shield to reduce noise (Lognonné et al., 2019). Preprocessing included removing the instrument response from the raw continuous data followed by bandpass filtering from 0.01 to 3.5 Hz. The data were then cut into ~1100 2-hour windows and rotated into Z-N-E (Vertical-North-East) components based on the dip and azimuth information of U-V-W channels. We removed the mean and trend and tapered each 2-hour-long window using the Tukey window with cosine fraction of 0.02. Figure 2.1a shows the ~3.7-sol long raw Z-component waveform sample, where the low-frequency

signals may correspond to the diurnal weather and tidal variation. Figure 2.1b is the Z-component waveform after the removal of instrument response and filtering from 0.01 to 3.5Hz. The high-amplitude spikes (Figure 2.1b) are probably generated by lander operations during a Martian sol. To suppress these features, we applied a temporal balance (Bensen et al., 2007) using a running absolute mean normalization to eliminate the effects of non-stationary noise before making the autocorrelograms. The weighting function w(t) used to normalize the trace s(t) is defined as

$$w(t) = \frac{1}{\frac{1}{2N+1}\sum_{t-N\Delta t \le \tau \le t+N\Delta t} |s(\tau)|}$$

Equation 2 - Weighting function for temporal balance.

where 2NΔt is the parameter to control the length of moving-average windows. In this paper, we will calculate the weighting function using 100s moving-average window to normalize the seismic data. The Z-component waveform with temporal balance is shown in Figure 2.1c, illustrating that the energetic peaks are significantly diminished compared with the original trace in Figure 2.1b.

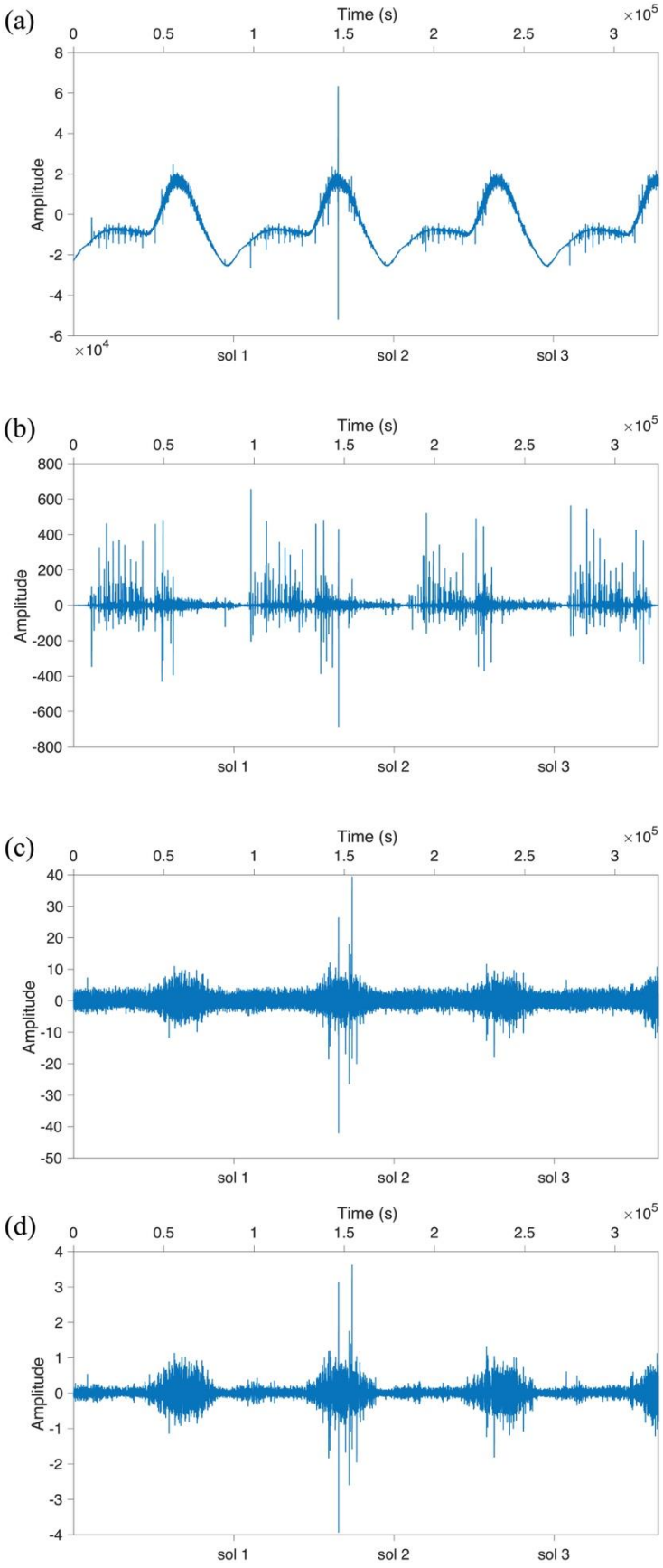
(a)
Time (s)
×10^5
Amplitude
×10^4
sol 1
sol 2
sol 3
(b)
Time (s)
×10^5
Amplitude
sol 1
sol 2
sol 3
(c)
Time (s)
×10^5
Amplitude
sol 1
sol 2
sol 3
(d)
Time (s)
×10^5
Amplitude
sol 1
sol 2
sol 3

Figure 2.1 – (a) The raw Z-component data with instrument response. The data are recorded from 4/26/2019 to 4/29/2019 (~3.7 sols). (b) The Z-component data after the removal of instrument response and bandpass filter between 0.01 and 3.5Hz. (c) The Z-component data at the same period after temporal balance. (d) The Z-component data at the same period after spectral whitening.

Compared to broadband seismic data on Earth, the InSight data contains much more low-frequency energy. A spectral whitening method (Bensen et al., 2007; Oren & Nowack, 2017; Phạm & Tkalčić, 2017, 2018) is applied to each two-hour long data window to remove the low-frequency bias and boost the high-frequency component (Figure 2.1d), where the whitening width is empirically determined as 0.5Hz (Phạm & Tkalčić, 2017). The processing for spectral whitening is similar as the temporal balance shown above but is applied in frequency domain (Phạm & Tkalčić, 2017). The application of spectral whitening will make the reflection phases more pronounced and interpretable (Delph et al., 2019; Phạm & Tkalčić, 2017). The autocorrelograms are computed and normalized by the maximum amplitude at zero lag for each trace. In order to boost the coherent signals of each trace and suppress the noise, a linear phase-weighted stacking (PWS) method (Schimmel & Paulssen, 1997) was applied to the sum of autocorrelation windows. We chose the linear weight empirically, based on the trade-off between the coherency measure and waveform distortion. Lastly, we sum all of the two-hour autocorrelation windows, producing two autocorrelation estimates, one with and one without phase-weighting.

In order to recover the seismic discontinuities throughout the depths of Mars (ranging from 10’s km to > 1000 km), we applied different bandpass filters: overlapping

butterworth bandpass filters in the high-frequency range (0.625-3.0Hz) show what we interpret to be the Moho discontinuity whereas low-frequency (0.05-0.2Hz) overlapping filters show what we interpret to be the mantle olivine-wadsleyite transition and the core-mantle boundary. We also examined different frequency bands to determine the robustness of the observed seismic phases. In order to assess the robustness of the phases we identified, we performed bootstrap calculations on the 2-hour ambient noise autocorrelograms filtered in both low and high frequency bands. We randomly selected several subsets from the whole dataset and repeat the same processing method to construct the reflectivity response. We set the size of each subset with respect to the size of whole dataset as 0.8, and randomly choose 30 different subsets. After stacking and filtering, we converted the resulting autocorrelograms from time to depth using the P-wave velocity models derived from the joint inversion of multiple geophysical data (Khan et al., 2018) and mineralogical simulations (Panning et al., 2017; Yoshizaki & McDonough, 2020).

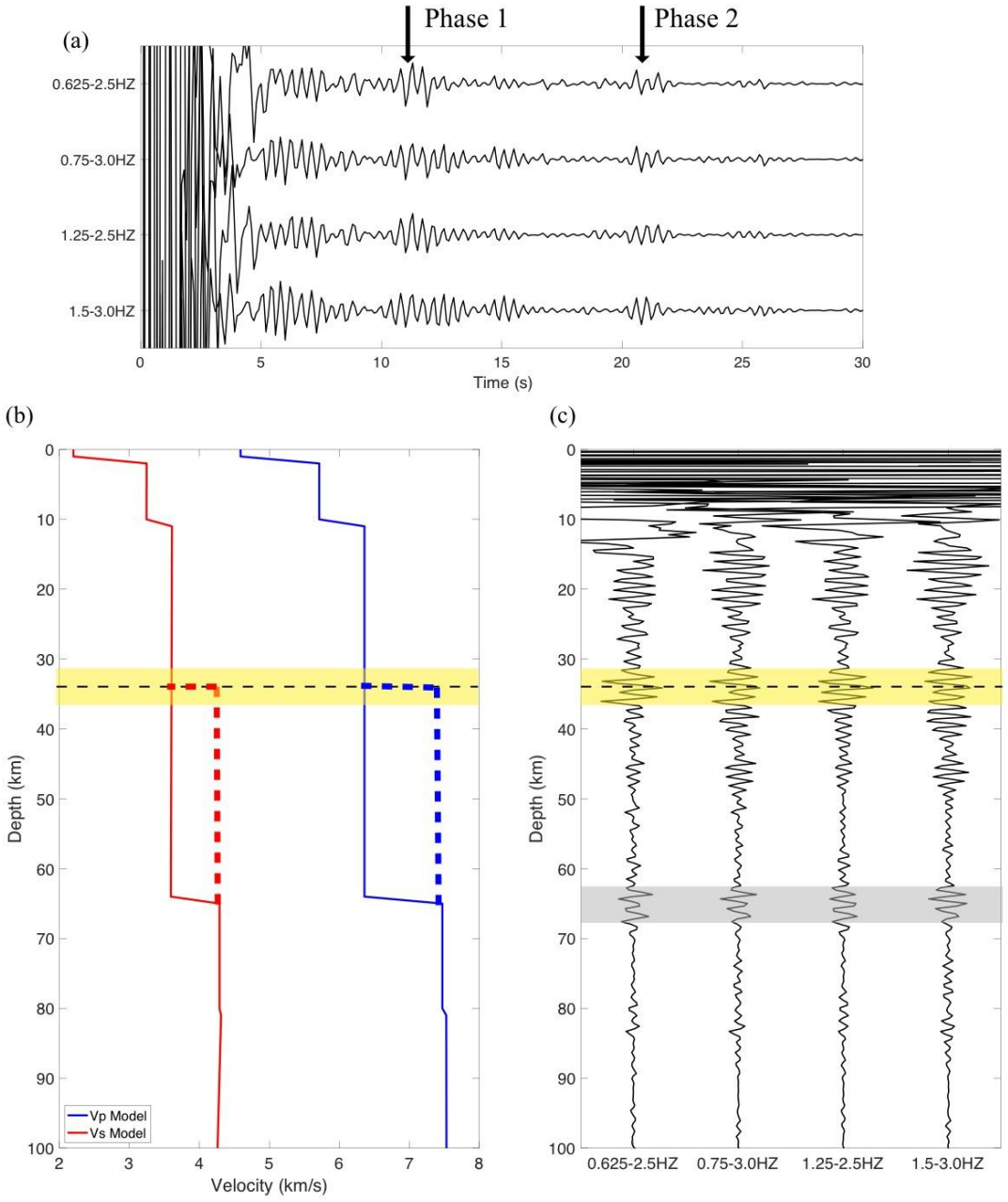

Figure 2.2 – (a) The PWS stacked autocorrelograms filtered into different high frequency bands. Arrivals at ~11.5s (Phase 1) and at ~21s (Phase 2) are marked as black arrows. The arrivals can be interpreted as the Moho reflections PmP and SmS (model 1), as PmP and PmP2 (model 2), as PmP, and an upper mantle discontinuity (model 3), or as an intracrustal event and PmP (model 4). (b) The P- (blue solid line) and S-wave (red solid line) velocity model (LFAK) (solid line) derived from the joint inversion of multiple geophysical data (Khan et al., 2018). The dashed lines at

~35km represent the crustal thickness beneath the InSight lander derived from autocorrelation reflectivity series if models 1), 2) and 3) are assumed. (c) Depth conversion of the autocorrelation reflectivity using the P-wave velocity model in (b). The yellow shaded area at ~35km represents the interpreted Martian Moho for model 1), 2) and 3) or the intracrustal discontinuity for model 4). The gray shaded area does not have physical meaning if Phase 2 is interpreted as SmS for model 1) or PmP2 for model 2). The gray shaded area at ~68km corresponds to the depth of upper mantle discontinuity for model 3) or the Martian Moho for model 4). We prefer model 1).

2.3. Results and Discussion

2.3.1. Moho Discontinuity

The high frequency filtered ambient noise data show prominent reflection phases at ~11.5 sec (Phase 1) and ~21.0 sec (Phase 2) across several frequency bands in both the PWS stack (Figure 2.2a) and the linear stack (Figure 2.3). The signal at ~6s blends into the autocorrelation 0-lag side lobes (Figure 2.2a), so we will not interpret this event as a reflection phase from Martian interior. Bootstrap calculations suggest the phase identification is robust (Figure 2.4). These events can be interpreted a number of different ways. 1) The first phase could be PmP, the P-wave Moho reflection and the second the SmS phase, the S-wave Moho reflection (Figure 2.2a). SmS can be observed on a vertical component, because the recorded noise incidence angles actually form a narrow cone around vertical rather than arriving only vertically (Gorbatov et al., 2013; Oren & Nowack, 2017; Phạm & Tkalčić, 2017). 2) Phase 1 could be PmP while the second phase could be the multiple of the first event, PmP2, since the arrival of the second event is close to double the time of Phase 1. 3) Phase 1 could be PmP, with Phase 2 an event from

the upper mantle. 4) The first phase might be an intracrustal event analogous to the Conrad discontinuity and the second phase the Moho.

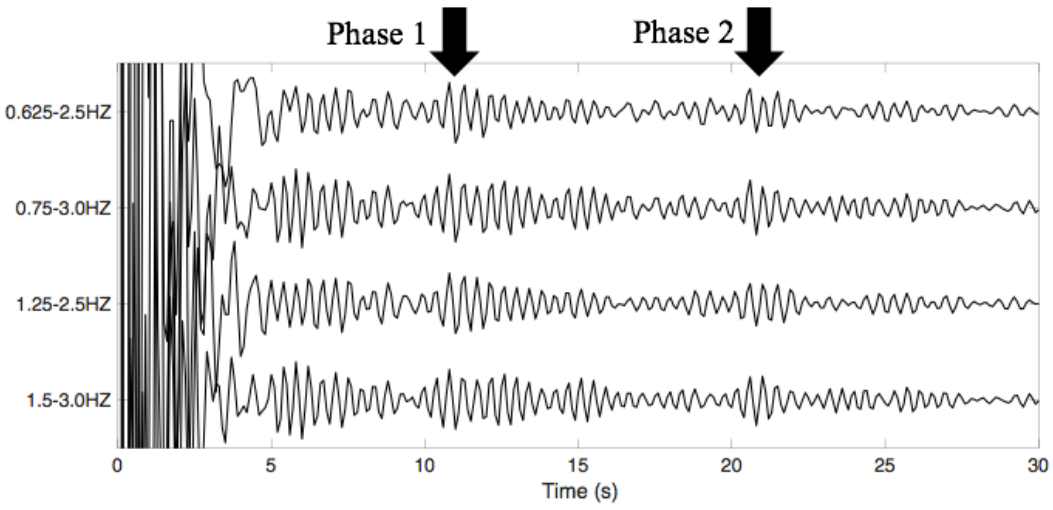

Figure 2.3 – Same as Figure 2.2a but for linear stacking

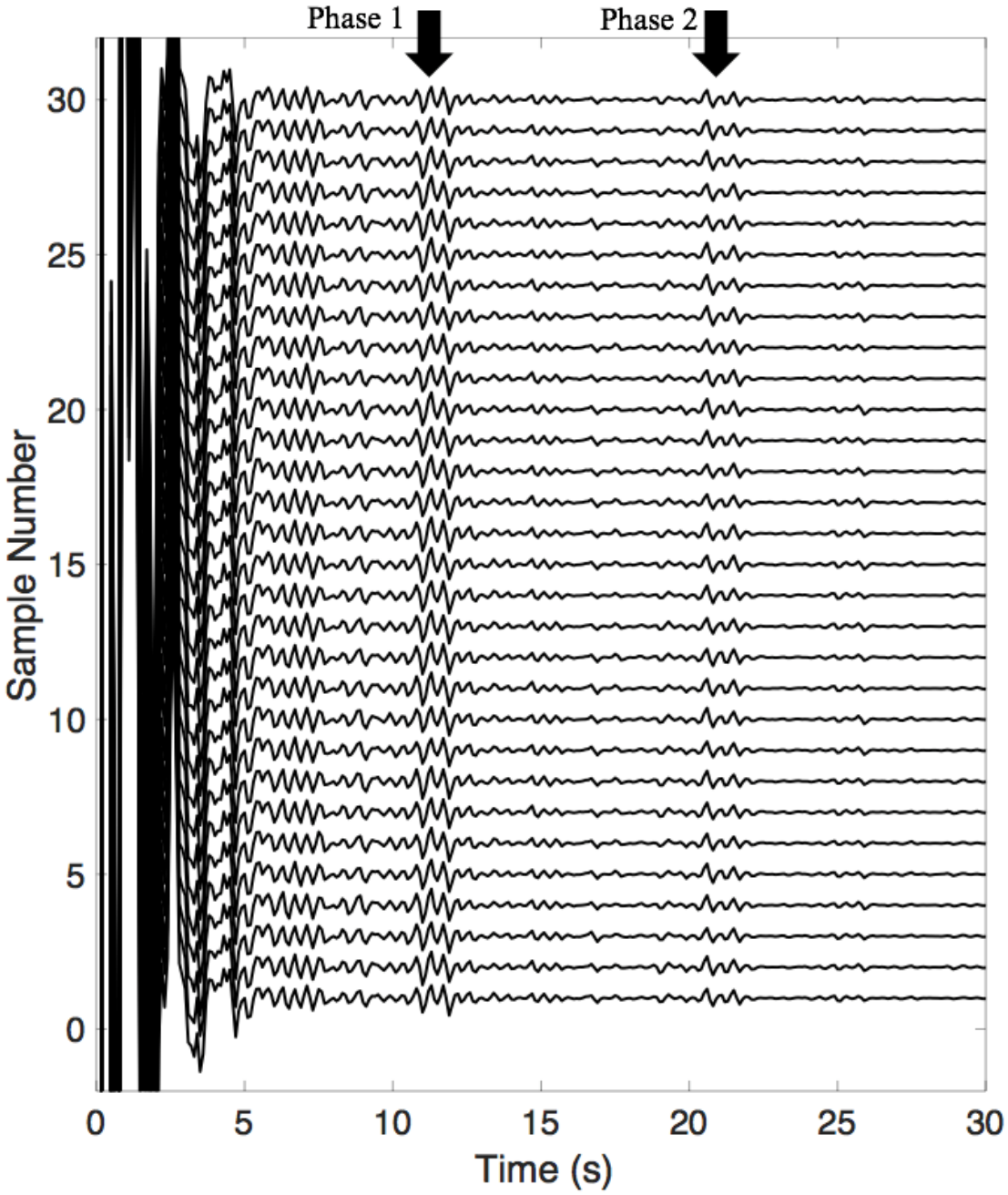

Figure 2.4 - Bootstrap calculation for the autocorrelograms filtered between 0.625 and 2.5Hz

Using a P-wave crustal velocity model (LFAK) for a gabbroic crust shown in Figure 2.2b (Khan et al., 2018), the first three models give a crustal thickness of ~35km depth (Figure 2.2c). The crustal thickness of ~35km is 30 km shallower than that in the LFAK velocity model (Figure 2.2b). One possible interpretation is that the Moho depth (~65km) of LFAK velocity model represents the average of the thin crust of Martian northern hemisphere (~30-40 km) and the thick crust (~70-80 km) of the southern hemisphere while the autocorrelation reflectivity series in our study measure local crustal thickness beneath the InSight lander. The global Martian crustal thickness map inverted from gravity data (Genova et al., 2016; Parro et al., 2017; Zuber, 2000), shows a crustal thickness of 30-35 km at the InSight lander site, close to the 35km estimated for the first event being PmP.

Assuming the second event is SmS, the Vp/Vs (Vp: P-wave velocity; Vs: S-wave velocity) ratio of the Martian crust is estimated from the S- and P-wave reflection traveltimes, namely,

$$\frac{V_p}{V_s} = \frac{T(SmS)}{T(PmP)} \approx 1.83$$

Equation 3 - The calculation of Vp/Vs ratio of Martian crust

which is compatible with the Vp/Vs ratio for basaltic and andesitic rocks (~1.84) (Christensen, 1996). Thermal emission spectral analysis of the Martian surface (McSween et al., 2003, 2009) and geological observations (Golombek et al., 2020) suggests that the Martian crust is andesitic and basaltic. The Vp/Vs ratio we measure is consistent with that result.

Assuming the second event is from a mantle interface gives a depth of ~68 km, or 33 km into the mantle. This could represent an intra-lithospheric boundary remnant from basalt extraction. The Martian lithosphere has been estimated to be greater than 150 km based on elastic modelling (Grott & Breuer, 2010; Schumacher & Breuer, 2006; Thurber & Toksöz, 1978), hence the second event is unlikely to represent the Martian lithosphere-asthenosphere boundary.

The fourth interpretation gives a crustal thickness of ~68 km, and an intracrustal horizon at ~35 km. We would interpret the first event as the boundary between an intermediate and mafic crust.

Given the gravity estimates of crustal thickness and the Vp/Vs ratio being close to that expected for a gabbroic crust, we favor the interpretation that the 11.5 s event is PmP and the 21s event is SmS.

2.3.2. Olivine-Wadsleyite Transition and Core-Manle Boundary

We observe two prominent events in the low-frequency band of both the PWS (Figure 2.5a) and the linear stack (Figure 2.6) autocorrelograms, the first at ~280s and the second at ~375s. These two phases are also clearly observed in bootstrap calculations (Figure 2.7), further demonstrating the reliability of the phase identification. That lower frequency signals from deep within Mars are observable is not too surprising, as Mars is a cold, dry planet, and seismic attenuation is strongly dependent on temperature and on the fluid content of rocks. We use four P-wave velocity models (Figure 2.5b) to depth-convert the stacked autocorrelograms, one is the LFAK model (Khan et al., 2018), three

are from theoretical calculation of shear wave velocity for various bulk composition and thermal state models (Panning et al., 2017) where we assume a Vp/Vs ratio of 1.82 (Sohl & Spohn, 1997), and one is from a theoretical calculation of Vp (Yoshizaki & McDonough, 2020).

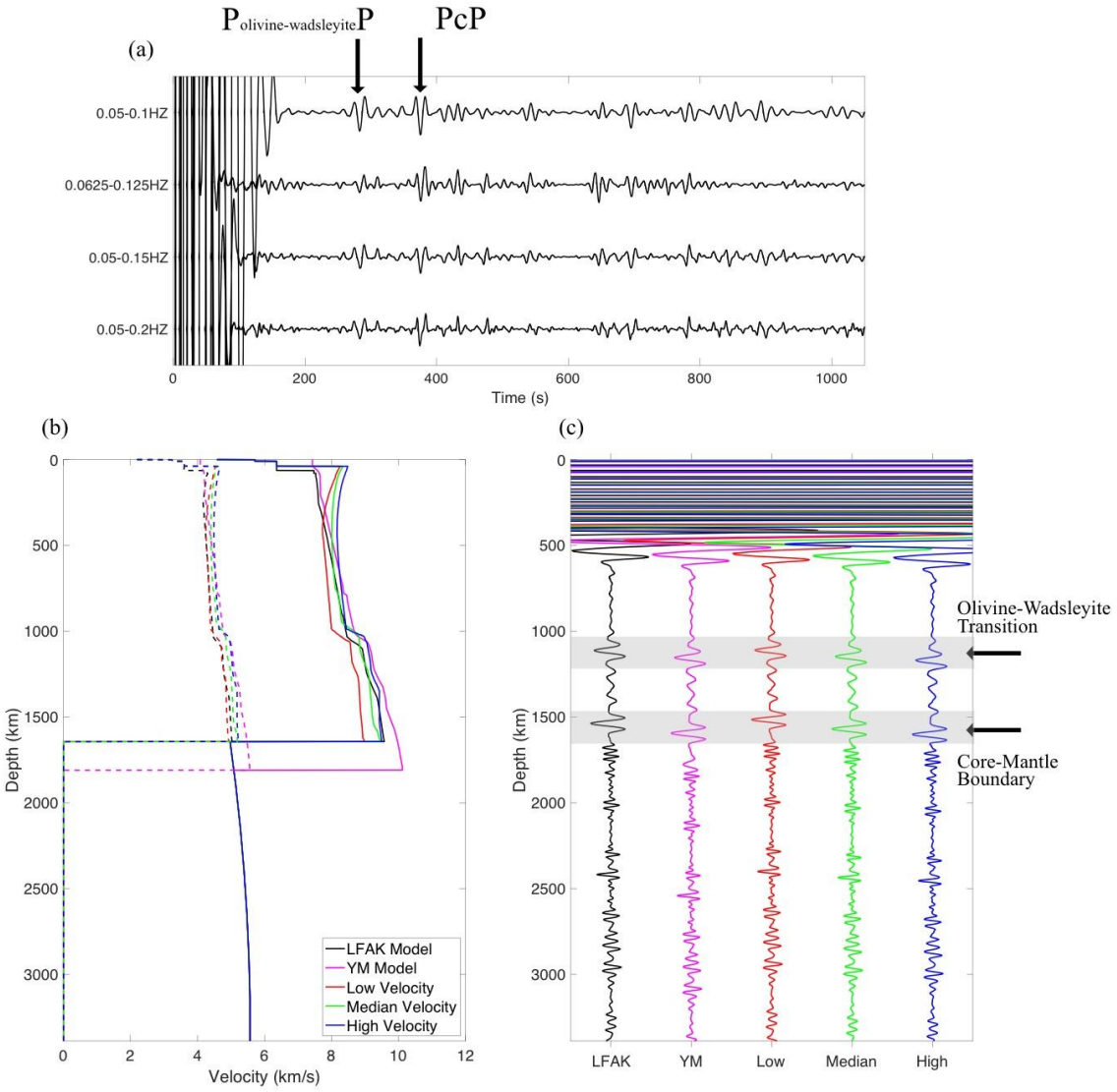

Figure 2.5 - (a) The PWS stacked autocorrelograms filtered into different low frequency bands. The arrival times expected of the reflection signals from olivine-

wadsleyite transition and core-mantle boundary are marked as black arrows. (b) The P- (solid line) and S-wave (dashed line) velocity model, LFAK model from the joint inversion of multiple geophysical data (Khan et al., 2018), YM model from theoretical calculation (Yoshizaki and McDonough, 2020) and three representative velocity models from mineralogical simulation (Panning et al., 2017). (c) Depth conversion of stacked autocorrelation reflectivity series filtered between 0.05-0.1Hz using all P-wave velocity models in (b). The gray shaded area represents the interpreted Martian olivine-wadsleyite transition and core-mantle boundary.

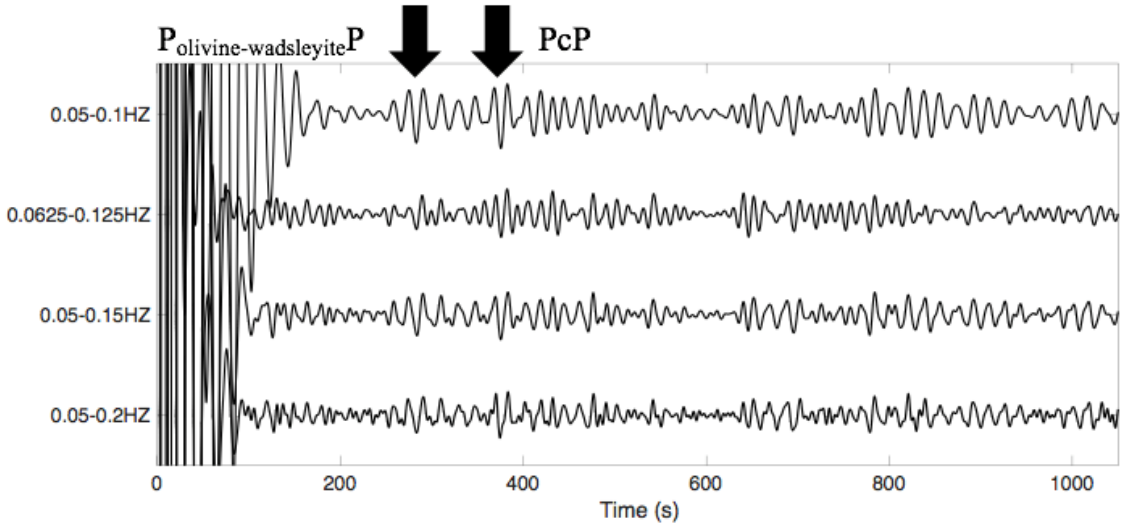

Figure 2.6 – Same as Figure 2.5a but for linear stacking.

Figure 2.5c shows the depth conversion of the reflectivity series filtered between 0.05 and 0.1Hz using the four models shown in Figure 2.5b. We interpret the phase at ~280s as the reflection from the olivine-wadsleyite transition. Depth conversion using the different Martian seismic velocity models put this boundary at depths ranging from 1110 to 1170km. The depth of the olivine-wadsleyite phase transition on Mars is expected to be ~2.8 times greater than the corresponding discontinuity on Earth (~410km), a result of

the low gravity and mean density on Mars (gravity: 3.71m/s^2; mean density: 3.93g/cm^3) and lower internal temperatures compared with Earth (gravity: 9.81m/s^2; mean density: 5.51g/cm^3). The phase we identify as from the olivine-wadsleyite transition matches the results derived from thermodynamic and mineralogical inversion, where the depth of this transition is estimated to be at ~1100km (Khan et al., 2018; Khan & Connolly, 2008; Verhoeven et al., 2005; Yoshizaki & McDonough, 2020).

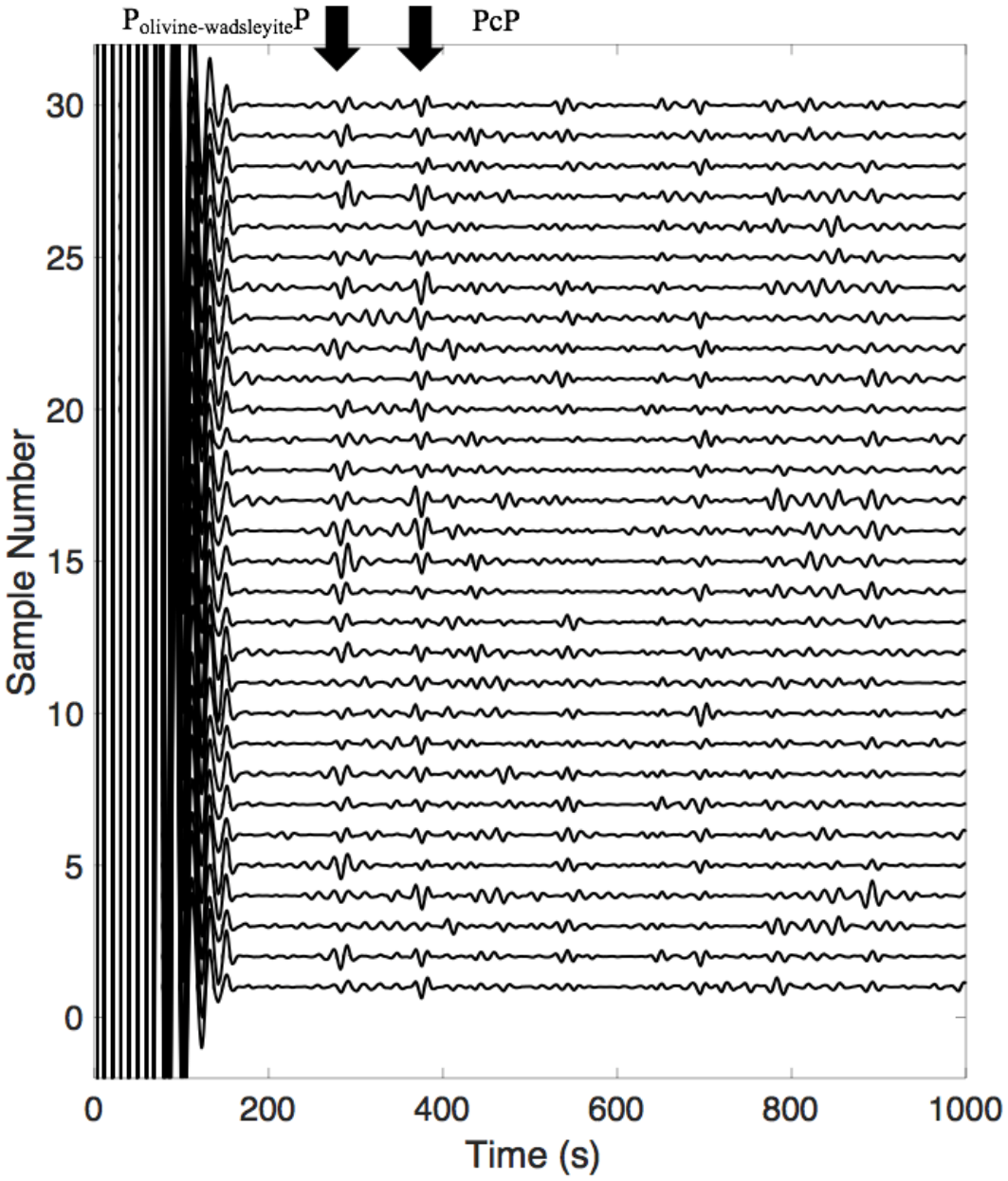

Figure 2.7 - Bootstrap calculation for the autocorrelograms filtered between 0.05 and 0.1Hz.

A second prominent event at ~375 s depth converts to 1520-1600 km (Figure 2.5c). A thermal model of the mantle (Khan & Connolly, 2008) predicts the Martian

mantle would not reach the temperatures and pressures necessary for the ringwoodite-perovskite transition, referred to as the 660 discontinuity on Earth. The mineralogical model suggests that the theoretical depth of the ringwoodite-perovskite transition would occur at ~1900km (Breuer et al., 1996), therefore we interpret the second deep event as the body-wave reflection from the Martian core-mantle boundary, PcP (Figure 2.5a). Depth conversion with the four velocity models shown in Figure 2.5b, puts the core-mantle boundary in the depth range 1520-1600 km (Figure 2.5c). Since the average radius of Mars is ~3390km, we estimate the core radius to be 1790-1870 km.

Yoder et al. (2003) estimated the potential Love number k_2, which represents the solar tidal deformation of Mars, to constrain the Martian core radius to be 1520 to 1840km. Rivoldini et al. (2011) inverted geodetic data assuming various mineralogic models and thermal conditions, giving a core radius between 1700 and 1900km. Khan et al. (2018) explored several geophysical observations, such as moment of inertia, mean mass and tidal response of Mars, to recover the bulk composition and thermal state, and estimated the core radius to be 1730–1840 km. In general, our measurement of depth to the core-mantle boundary and the core radius is consistent with the results from other types of geophysical data.

2.4. Conclusion

Using ambient noise autocorrelation of Martian InSight seismic data, we constructed the reflectivity series beneath the lander. We observe two prominent events

from shallow in the Martian interior and two more prominent events from the deeper interior (Figure 2.8). Crustal, and possibly upper mantle, reflections could be observed in the high-frequency filtered autocorrelation function. Our preferred interpretation is a Martian Moho discontinuity at ~35km, and a Martian crust with Vp/Vs ~1.83, suggesting that the Martian crust beneath the lander is mainly basalt or andesite, consistent with the analysis of thermal emission spectra (McSween et al., 2003). To recover the deeper seismic discontinuities in Mars, we examined low-frequency filtered autocorrelograms which show reflection signals at times consistent for the Martian olivine-wadsleyite transition and the Martian core-mantle boundary. Using different velocity models simulated for various compositional and thermal models (Khan et al., 2018; Panning et al., 2017; Yoshizaki & McDonough, 2020), the olivine-wadsleyite transition and core-mantle boundary of Mars would be at 1110-1170km and 1520-1600km, respectively.

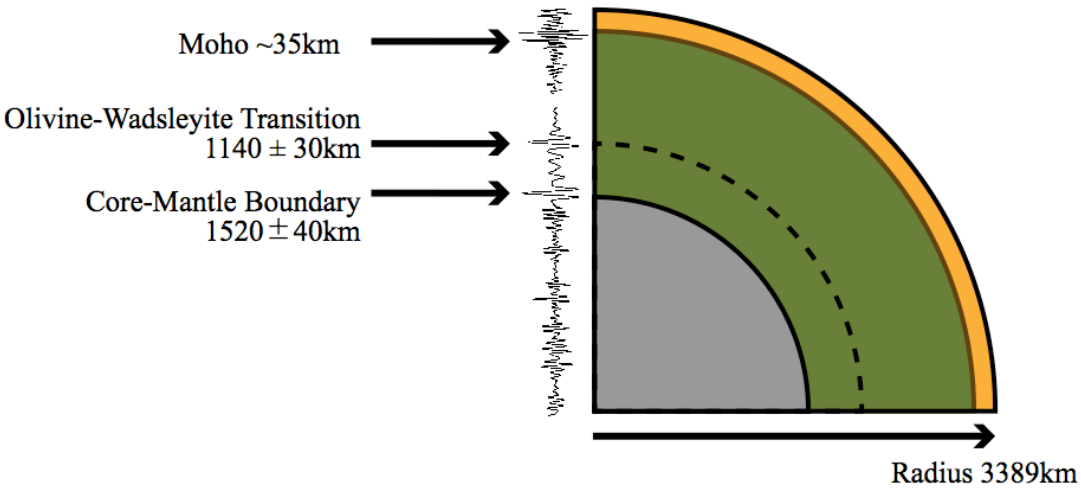

Figure 2.8 - Schema of the Martian interior based on the depth of seismic discontinuities from autocorrelation analysis and assumed velocity models. The yellow, green and gray regions represent Martian crust, mantle and core respectively. The depths of interpreted Moho, olivine-wadsleyite transition and core-mantle boundary are indicated.

Chapter 3

Seismic Autocorrelation Analysis of Deep Mars

The InSight mission deployed one seismic station on Mars at the end of 2018 to measure the interior structure of another terrestrial planet. Some recent studies correlated the InSight ambient noise seismic data with themselves to retrieve the reflection signals from subsurface discontinuities. The seismic signals reflected from deep Mars, such as the olivine-wadsleyite transition, a pressure-temperature dependent mineral phase change in the mantle, and the core-mantle boundary were detected by the low frequency ambient noise autocorrelation. However, some analysis suggested that the arrival times of these signals coincide with the recurrence time of high-amplitude glitches within raw seismic data, leading to an incorrect interpretation of the autocorrelation. To resolve the contradiction, we detected and removed these high-amplitude glitches before further processing of the ambient noise data. The autocorrelation analysis of deglitched

continuous vertical-component waveforms still recovers the signals originating from olivine-wadsleyite transition and core-mantle boundary, whereas autocorrelation of glitch-only waveforms does not. This suggests that the observed signals on the low-frequency autocorrelation are from seismic discontinuities rather than a noise artifact. The velocity layering near Martian core-mantle boundary is improved to match with the observed PcP phase in the autocorrelation of deglitched dataset.

3.1. Introduction

The spacecraft of the InSight mission landed on Mars at the end of 2018. In early 2019, it deployed the only seismic station, named SEIS, to record the seismic vibrations on Mars (Lognonné et al., 2019). The InSight seismometer successfully detected 951 Marsquake events by October 2021 (Horleston et al., 2022), providing indications on the tectonic activities within Mars (Giardini et al., 2020; Jacob et al., 2022; Sun & Tkalčić, 2022). The Martian seismic data have been used in research to understand the interior structures of the red planet at different scales using autocorrelations (Compaire et al., 2021; Deng & Levander, 2020, 2022; Schimmel et al., 2021), receiver functions (Knapmeyer-Endrun et al., 2021; Lognonné et al., 2020), anisotropy analysis (J. Li et al., 2022), attenuation modeling (Karakostas et al., 2021) and geophysical inversion (Khan et al., 2021; Stähler et al., 2021).

Claerbout (1968) showed that the reflectivity response for a coincident surface source and receiver in an acoustic medium can be reconstructed by autocorrelation of the normal-incident plane wave response due to a source incident from below recorded by a surface receiver. This was extended to elastic media and non-normal incidence cases (Frasier, 1970). Autocorrelation analysis of single-station seismic recordings (e.g., ambient noise, coda waves) has been widely employed to extract body-wave reflection phases to reveal the subsurface structures of Earth (Delph et al., 2019; Gorbatov et al., 2013; Kennett, 2015; Oren & Nowack, 2017; Phạm & Tkalčić, 2018, 2021; Qin et al., 2020; She et al., 2022; Tibuleac & von Seggern, 2012; Zhou & Zhang, 2021) and Moon (Nishitsuji et al., 2016, 2020). Recent autocorrelation analysis on Mars detected a strong P-wave reflection phase at ~11 s two-way traveltime (Compaire et al., 2021; Deng & Levander, 2020; Schimmel et al., 2021). This ~11 s signal can be interpreted as the reflection from a mid-crust discontinuity or Martian Moho at approximately 35 km (Deng & Levander, 2020). To examine deeper seismic structure of Mars, Deng and Levander (2020) filtered the stacked autocorrelations in the low-frequency 0.05 and 0.1 Hz band, and identified signals at ~280 s and ~375 s as P-wave reflections from the Martian olivine-wadsleyite transition and core-mantle boundary, respectively. Depth conversion using different reference velocity models determined the Martian core radius in the range of 1790-1870 km (Deng & Levander, 2020), consistent with the core radius estimation from other studies (Khan et al., 2018; Rivoldini et al., 2011; Yoder et al., 2003). However, Scholz et al. (2020) identified high-amplitude seismic glitches within raw SEIS data which probably originate from stress relaxation within the InSight seismometer,

which may contaminate the final results of seismic analysis if not removed (Compaire et al., 2021). Barkaoui et al. (2021) analyzed the quasi-periodic recurrence time of these seismic glitches and found it coincides with the arrival times of identified phases in low-frequency autocorrelations in Deng and Levander (2020). Kim et al. (2021) did the autocorrelation tests and further suggested that the signals interpreted as olivine-wadsleyite transition and core-mantle boundary in Deng and Levander (2020) may result from the quasi-periodic high-amplitude glitches rather than the real seismic boundaries of Martian interior.

In this work, we designed tests to resolve whether the low-frequency autocorrelation signals in Deng and Levander (2020) are real seismic reflection signals or result from instrumental noise. The high-amplitude glitches in raw SEIS data were first detected to generate three datasets for further analysis: (1) the raw continuous data with glitches; (2) the deglitched continuous data after the application of glitch removal algorithms; and (3) the data with only detected glitches calculated by the subtraction of (2) from (1). We implemented the ambient noise autocorrelation on the vertical-component recordings of these three datasets to demonstrate the low-frequency autocorrelation signals are the reflection response from deep Mars rather than the recurrence time of quasi-periodic glitches shown in Barkaoui et al. (2021). The synthetic PcP phases for the models in Stähler et al. (2021) were calculated to make comparisons with the observed PcP phase in the autocorrelation of deglitched dataset. The velocity layering model near Martian core-mantle boundary was derived to minimize the misfit between the synthteic and observed PcP phases.

3.2. Data and Methods

The SEIS data were collected with a 10 Hz sampling rate from February to May 2019, and 20Hz sampling rate from June 2019 to December 2021. Prior to the preprocessing, the open-source package SEISglitch (Scholz et al., 2020) were applied to extract and remove the high-amplitude glitches within the raw continuous SEIS waveforms to get deglitched and glitch-only data. Figures 3.1a to 3.1c provide a 1-day example on January 3rd, 2020 to show the comparisons between original and deglitched continuous U-, V- and W-component data. The glitches were mostly detected at night time during periods of relatively low temperature (Figure 1d) and windspeed (Figures 1e) because of the low wind- and pressure-driven noise level during the nighttime (Scholz et al., 2020). Figures A1 and A2 in the appendix designed a test for the parameter selection of glitch detection and removal, which suggest the parameter values of SEISglitch will have modest impact on the final autocorrelation results. The preprocessing procedures included the instrument response removal from the raw, deglitched and glitch-only continuous SEIS data with a broad bandpass filter from 0.01 to 3.5 Hz. The data sampled at 20Hz were then decimated to 10 Hz. The continuous waveforms were cut into 4-hour-long segments and rotated into from U-V-W to orthogonal Z-N-E channels (Compaire et al., 2021). We removed the mean and trend and applied a taper to each 4-hour raw, deglitched and glitch-only data window.

We used the similar workflow as Bensen et al. (2007) to calculate autocorrelations for raw, deglitched and glitch-only data. Temporal balance and spectral

whitening were employed to improve the interpretability of the stacked ambient noise autocorrelations (Bensen et al., 2007; Oren & Nowack, 2017). Each individual 4-hour trace was then filtered between 0.05 and 0.1 Hz. We computed and normalized the vertical component autocorrelograms by the maximum amplitude at zero lag time for each 4-hour-long trace. We applied both linear stacking (LS) and phase-weighted stacking (PWS) (Schimmel & Paulssen, 1997) to stack autocorrelograms. The power of PWS, which defines the significance of coherency measure (Schimmel & Paulssen, 1997), is empirically selected as 2 (Korenaga, 2014; Niu & Chen, 2008; Wookey & Helffrich, 2008).

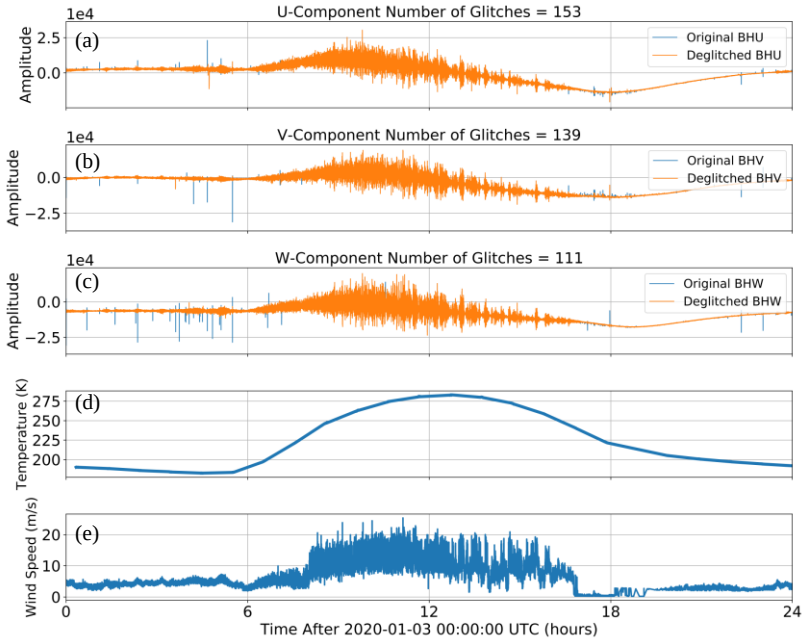

Figure 3.1 - (a) Original (blue) and Deglitched (orange) U-component waveforms on January 3rd, 2020. (b) Same as (a) but for V-component. (c) Same as (a) but for W-

component. (d) The ground temperature data on January 3rd, 2020. (e) The windspeed data on January 3rd, 2020.

3.3. Results and Discussion

3.3.1. Autocorrelation Results

Figure 3.2 compares the LS and PWS stacked autocorrelation of raw, deglitched and glitch-only datasets. Two prominent signals at ~285 s and ~385 s can be clearly observed from the stacked autocorrelation of the deglitched waveform. The arrival times of these two signals are consistent with the prominent phases identified as the P-wave reflection from the olivine-wadsleyite transition and core-mantle boundary reported previously in Deng and Levander (2020). This suggests that these two phases originate from the deep seismic discontinuities in Mars rather than being correlation artifacts from quasi-periodic glitches in the raw SEIS data suggested in Barkaoui et al. (2021) and Kim et al. (2021). The bootstrap calculation also indicates the observation of these two phases is robust (Figure A4). The autocorrelation function of glitch-only data does not show a prominent response at ~285 s or ~385 s. We take this as indicating the reflection responses at ~285 s and ~385 s originate from Martian impedance boundaries. The stacked raw data autocorrelation can also detect the signals at ~285 s and ~385 s, but the reflection pulses are more complicated than the deglitched waveform because they are contaminated by the high-amplitude seismic glitches within the raw data. The PWS

stacked autocorrelation of the deglitched ambient noise data (red curve in Figure 3.2b) will be used for the comparison with the synthetic results since the observed reflection phases are clearer than linear stack.

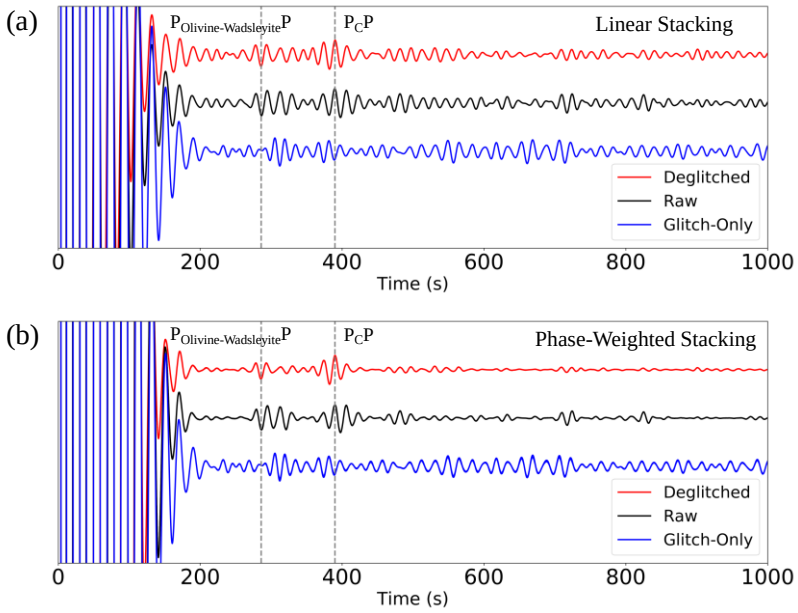

Figure 3.2 - (a) Linearly stacked (LS) vertical-component autocorrelation filtered between 0.05 and 0.1Hz using raw (black), deglitched (red) and glitch-only (blue) data. The gray dashed lines mark the reflection phases from olivine-wadsleyite transition and core-mantle boundary. (b) Same as (a) but for phase-weighted stacking (PWS) (Schimmel & Paulssen, 1997)

3.3.2. Comparison with Synthetic PcP Phases

We simulated the synthetic PcP phases with Thomson-Haskell matrix method (Haskell, 1953; Shearer, 2019) for a set of velocity models (Figure 3.3a) derived from the

probabilistic inversion of seismic traveltimes, Love number k_2 and moment of inertia (Stähler et al., 2021). The comparison between synthetic and real PcP signals are shown in Figure 3.3b, which suggests that the velocity model with 3 standard deviations lower than the mean model of Stähler et al. (2021) best matches with the observed PcP phase. This observation is consistent with the Mars orbiting surface wave results (Deng & Levander, 2022).

We calculated the two-way traveltimes for mean-3σ model and mapped the observed reflection response from olivine-wadsleyite transition to depth (Figure A5). The depth of olivine-wadsleyite transtion is estimated at ~1090km (Figure A5). The depth of olivine-wadsleyite transition is ~2.7 times deeper than the depth on Earth (~410 km), which results from the lower gravity and mean density on Mars in comparison to Earth (Mars gravity: 3.71 m/s^2, mean density: 3.93 g/cm^3; Earth gravity: 9.81 m/s^2, mean density: 5.51 g/cm^3). Our depth estimation of olivine-wadsleyite transition is compatible with the results derived from thermodynamical calculations, which suggest the olivine-wadsleyite transition is near 1100 km depth on Mars (Verhoeven et al., 2005; Yoshizaki & McDonough, 2020).

3.3.3. CMB Transition Zone Modeling to Match with the Observed PcP phase

The CMB transition zone (TZ) velocity $V_{TZ} = \alpha V_{mantle} + (1-\alpha)V_{core}$, where $0 \leq \alpha \leq 1$. If $\alpha = 1$, it is the mean-3σ velocity model shown in Figure 3.3a because it best fits with the observed PcP phase among Stähler et al. (2021) suite of models (Figure

3.3b). We tried to improve the fit between the synthetic and observed PcP phases with 40, 60, 80, 100 and 120km thick 1-layer transition zones. For 40km thick transition zone cases, we made the grid search of CMB transition zone velocity with α ranging from 0.05 to 1 with 0.05 grid size and simulated the synthetic PcP phases by Thomson-Haskell matrix (Haskell, 1953) for all transition zone velocities. Then we calculated the correlation coefficients between the synthetic and observed PcP phases. The model with highest correlation coefficients with be set as the best 40km thick CMB transition zone model. The same procedure will be repeated to find the best CMB transition zone models with 60, 80, 100 and 120km thickness. Figures A6 to A10 showed the correlation coefficients and waveform comparisons with the observed PcP phase for 40, 60, 80, 100 and 120km thick CMB transition zone models, respectively.

Figure 3.4a illustrates the best 40, 60, 80, 100 and 120km thick CMB transition zone models. Figure 3.4b makes the comparisons between the observed PcP phase and synthetic PcP of the velocity models shown in Figure 3.4a. We can see the 60km thick transition zone model (green model in Figure 3.4a) at Martian CMB can best fit the observed PcP phase (Figure 3.4b). We also tried two 60km thick velocity gradient at CMB transition zone and found the correlation coefficients are lower than the best 1-layer 60km thick transition zone model (Figure 3.5). It indicates the Martian CMB is more likely to have a 60km thick 1-layer transition zone rather than a simple sharp velocity drop. Since a 60km thick 1-layer transition zone model has already reached a high correlation coefficient at 0.99 (Figure 3.4b), it's not necessary to add more layers or

increase the model complexity of CMB transition zone to match with the observed PcP phase.

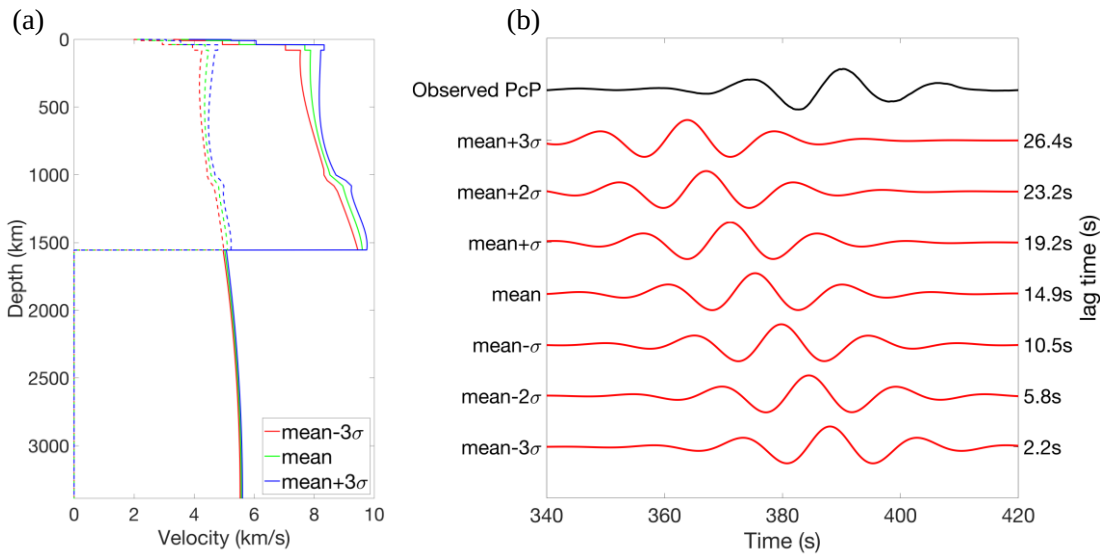

Figure 3.3 – (a) Mean velocity model and 3 standard deviations above and below the mean model in Stähler et al. (2021). The solid lines are P-wave velocity profiles and the dashed lines are S-wave velocity profiles. (b) Comparison between the synthetic PcP phases for the velocity models shown in (a) and the observed PcP phase. The lag time represents the correlation time shift between the synthetic and observed PcP phases, where the positive values represent the observed PcP travels slower than synthetic PcP, and vice versa.

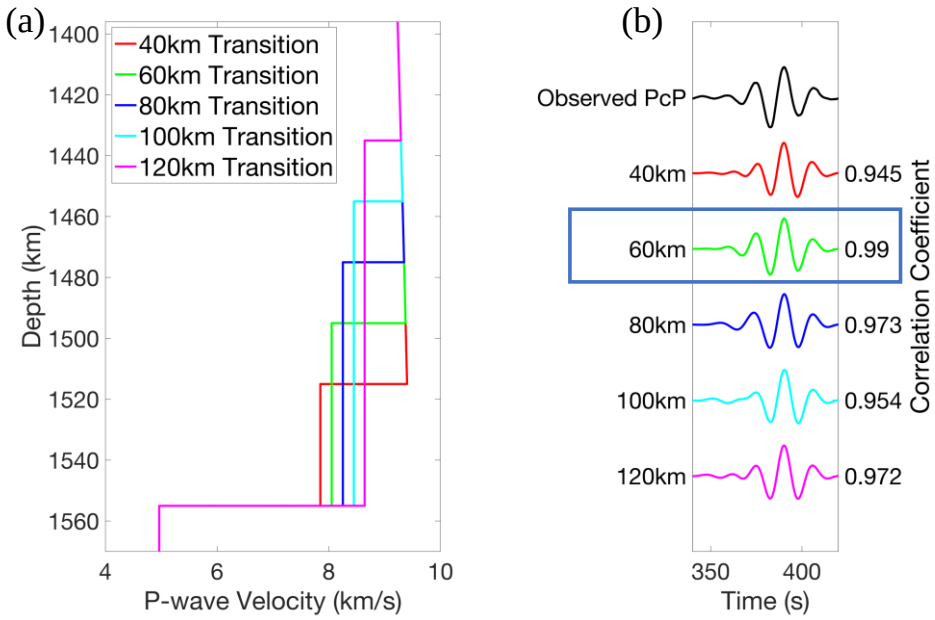

Figure 3.4 – (a) The best models for 40, 60, 80, 100 and 120km thick transition zones. (b) The comparison between the synthetic PcP phase of the velocity models shown in (a) and the observed PcP phase. The correlation coefficients between the synthetic and observed PcP are shown on the right side. The blue box marks the model with highest correlation coefficient among all models shown in (a).

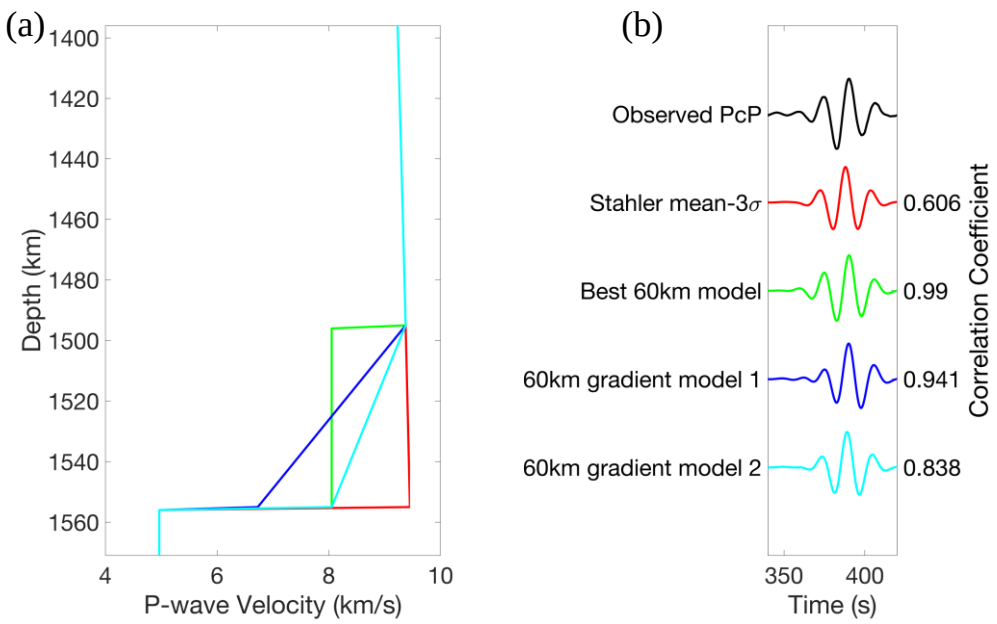

Figure 3.5 – (a) Four velocity models at CMB transition zone. The red one is the velocity that is 3 standard deviations lower than the mean velocity model in Stähler et al. (2021). The green one is the best 60km thick 1-layer transition zone model. The blue and cyan models are two 60km thick gradient velocity models. (b) The comparison between the synthetic PcP phase of the velocity models shown in (a) and the observed PcP phase. The correlation coefficients between the synthetic and observed PcP are shown on the right side. The best 60km thick 1-layer transition zone model provides the best fit among all models shown in (a).

3.4. Conclusion

Kim et al. (2021) and Barkaoui et al. (2021) suggested that the autocorrelation signals identified as the reflection response from olivine-wadsleyite transition and core-mantle boundary (Deng & Levander, 2020) may originate from the quasi-periodic glitches rather than real seismic discontinuities. In this study, we applied the autocorrelation method on raw, deglitched, and glitch-only vertical-component data to

resolve the contradiction. The prominent signals at ~285 s and ~385 s were extracted from the autocorrelation of raw and deglitched waveforms but not from glitch-only data (Figure 3.2). This suggests the signals at ~285 s and ~385 s are the reflection response from deep Mars rather than the recurrence time of high-amplitude glitches within raw SEIS data. We interpreted ~285 s signal as olivine-wadsleyite phase transition and ~385 s signal as core-mantle boundary. The synthetic PcP phases were simulated for a set of velocity models in Stähler et al. (2021) to compare with the observed PcP in the autocorrelation of deglitched dataset (Figure 3.3). We found the Martian velocity is slower than the mean model in Stähler et al. (2021) (Figure 3.3b), consistent with Mars orbiting surface wave results (Deng & Levander, 2022). The grid search was conducted to constrain the 1-layer transition zone velocity models near CMB and improve the fit between observed and synthetic PcP phases (Figure 3.4). A 60km 1-layer velocity transition zone model at Martian CMB is derived to better match with the observed PcP compared with a sharp velocity drop (Figure 3.4b).

Chapter 4

Autocorrelation R_2 on Mars

A purpose of the InSight mission is to reveal the Martian interior structure with seismic data. In this work, ambient noise autocorrelation of the continuously recorded vertical-component seismic signals has extracted the Rayleigh waves that propagate around the Mars for one cycle, R_2. The Mars orbiting surface waves are observed at a lag time of ~6000s in the stacked autocorrelation series filtered between 0.005 and 0.01Hz. Synthetic seismograms from a set of radially concentric velocity models were computed to find the best-fitting one as the starting model for a Monte Carlo inversion. The starting model was randomly perturbed iteratively to increase the correlation coefficients and reduce the absolute time shifts between the synthetic and observed R_2. An S-wave low-velocity layer in the inverted velocity model extends to ~400km depth, consistent with Marsquake observations, geophysical inversion and high-pressure experiments.

4.1. Introduction

The InSight (Interior Exploration Using Seismic Investigations, Geodesy and Heat Transport) spacecraft landed on Mars on November 26, 2018 and installed the seismograph SEIS (Seismic Experiment for Interior Structure) (Lognonné et al., 2019) to record continuous seismic data for approximately 3 years, providing opportunities to investigate another terrestrial planet's interior. A variety of research studies have been conducted recently to analyze the seismic recordings on Mars to monitor the seismicity (Banerdt et al., 2020; Böse et al., 2021; Ceylan et al., 2021; Clinton et al., 2021; Giardini et al., 2020; Knapmeyer et al., 2021), understand the ambient noise characteristics (Stutzmann et al., 2021; Suemoto et al., 2020) and recover the subsurface structures (Compaire et al., 2021; Deng & Levander, 2020; Khan et al., 2021; J. Li et al., 2022; Lognonné et al., 2020; Schimmel et al., 2021; Stähler et al., 2021). A prominent reflection phase is observed at ~11s in the stacked ambient noise autocorrelations, which may correspond to the crust-mantle boundary (Moho) or a mid-crust discontinuity at ~35km (Compaire et al., 2021; Deng & Levander, 2020; Schimmel et al., 2021) and is consistent with the shallow velocity models derived from receiver function analysis (Knapmeyer-Endrun et al., 2021; Lognonné et al., 2020; Schimmel et al., 2021). Moving to the deeper interior of Mars, the core-reflected phases (e.g. PcP, ScS) are observed from the Marsquake recordings (Stähler et al., 2021) and ambient noise autocorrelations (Deng & Levander, 2020), where the radius of Martian core is estimated as ~1830km for both methods (Deng & Levander, 2020; Stähler et al., 2021). However, some researchers have suggested that the observation of PcP phase (Deng & Levander, 2020) may originate

from the quasi-periodic seismic glitches in the continuous SEIS data (Barkaoui et al., 2021; Kim et al., 2021). We comment on this in chapter 3 of this thesis and another paper.

Seismic interferometry has been widely applied to retrieve the empirical Green's functions of surface waves (Berg et al., 2018; Miao et al., 2022; Qiu et al., 2020, 2021; Schimmel et al., 2018; Shen et al., 2013; Yao et al., 2006) and body waves (Clayton, 2020; Feng et al., 2017, 2021; Gorbatov et al., 2013; Kennett, 2015; Oren & Nowack, 2017; She et al., 2022) from the ambient noise auto- and cross-correlations. Many ambient noise surface wave tomography studies on Earth have focused on the calculations of the Rayleigh wave phase velocity to invert for the S-wave velocity of sedimentary basins (Cai et al., 2022; Hannemann et al., 2014; Pan et al., 2016; Qiu et al., 2019; Shirzad & Shomali, 2014), the crust and upper mantle (Hongyi Li et al., 2012; Lin et al., 2014; Nguyen et al., 2022; Yao et al., 2008; Zhang et al., 2018). Global tomography analysis suggested that the long period Rayleigh waves (e.g. >100s) can be recovered by cross-correlations of the Earth's hum (Haned et al., 2016; Nishida et al., 2009). This was subsequently extended to extract the Earth orbiting Rayleigh waves from a single-station-based autocorrelation to constrain the upper mantle velocity models (Hang Li et al., 2020; Schimmel et al., 2018; Jun Xie & Ni, 2019).

The observation of Rayleigh waves traveling around the Earth once, the phase R_2, using low-frequency autocorrelation of background free oscillations suggests the potential for a similar analysis for InSight seismic data (Schimmel et al., 2018), which then can be used to constrain Martian upper mantle velocity structure (Jun Xie & Ni,

2019). Here we followed the processing procedures in Bensen et al. (2007) to compute and stack the vertical-component autocorrelograms of the SEIS ambient noise data, which were bandpass filtered from 0.005 to 0.01Hz to retrieve the R_2 surface waves. The group dispersion curves were extracted by frequency-time analysis (FTAN) (Bensen et al., 2007; Levshin et al., 1992). We then compared observed R_2 to synthetic R_2 waveforms calculated from a suite of 1-D velocity models developed previously from joint inversion of multiple geophysical data types (Stähler et al., 2021). The best fit model from the Stähler et al. (2021) suite of models was used as the starting 1D model in a Monte Carlo inversion. We iteratively adjusted the Martian upper mantle velocity model between 40 and 700km depth to minimize the misfit between synthetic R_2 waveforms and the stacked R_2 autocorrelation.

4.2. Data and Methods

4.2.1. Martian Seismic Data and Glitch Removal

The InSight broadband continuous seismic data (InSight Mars SEIS Data Service, 2019) were obtained from IRIS (Incorporated Research Institutions for Seismology) website in three non-orthogonal channels (U-V-W). The data were sampled at 10Hz between February and May 2019 and at 20Hz between June 2019 and March 2021. The raw continuous signals contain the repeated high-amplitude glitches primarily induced by the stress relaxation of the seismometer (Scholz et al., 2020), which may contaminate

ambient noise autocorrelations (Compaire et al., 2021; Kim et al., 2021). In order to mitigate the effects of these high-amplitude spikes, we applied the open-source Python package SEISglitch (Scholz et al., 2020) to detect and remove the quasi-periodic glitches in the raw SEIS data. Figure 4.1 compares a 1-day record of the original and deglitched U-V-W components; the deglitched waveforms are clearly less spiky than the raw continuous data. We performed tests to determine that the glitch removal method can mitigate the effects of glitches without introducing additional artifacts (Figures 4.2 and 4.3). The instrument responses were deconvolved from the deglitched continuous waveforms, and the data were then bandpass filtered from 0.002 to 3.5Hz. The data with 20Hz sampling rate were downsampled to 10Hz to make sure all ambient noise data have the same sampling rate as 10Hz. We cut the ambient noise data into 584 daily segments and then rotated them to the orthogonal vertical, north and east (Z-N-E) components according to the azimuthal and dip angles of the oblique U-V-W components (Compaire et al., 2021; Suemoto et al., 2020). For each 1-day ambient noise epoch, the mean and linear trend were removed, and a 5% cosine tapered window was applied.

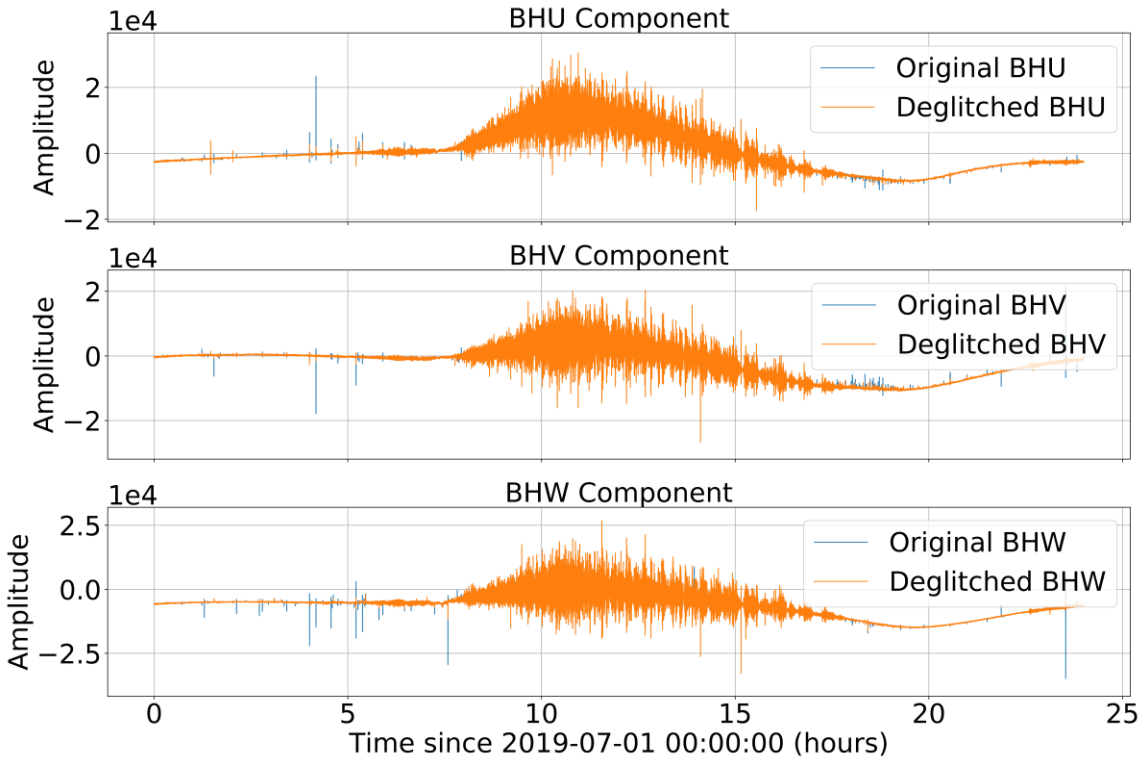

Figure 4.1 - (a) Glitch detection and removal on BHU-component by the Python package SEISglitch (Scholz et al., 2020) on the Martian broadband seismic data recorded on July 1st, 2019. (b) Same as (a) but for BHV-component. (c) Same as (a) but for BHW-component.

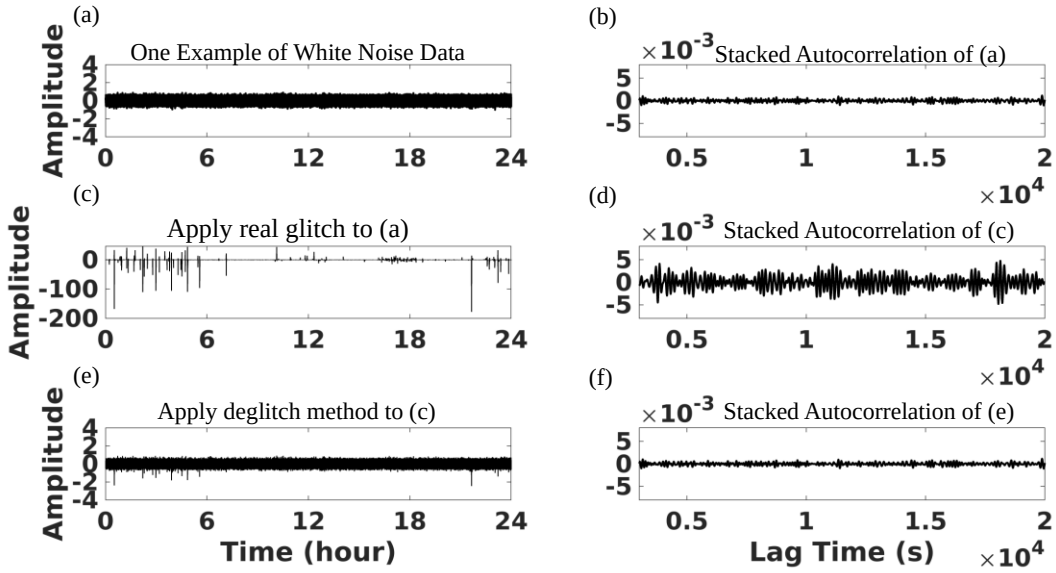

Figure 4.2 - (a) One example of white noise. (b) Stack of 584 autocorrelations using all white noise data as (a). No clear signals are detected from the stacked autocorrelations of white noise. (c) One example of a real glitched record added to (a). (d) Stack of 584 autocorrelations using all data with glitches as (c). Some high-amplitude signals related to the glitches show up. (e) Deglitching applied to the waveform in (c). (f) Stack of 584 autocorrelations using all the deglitched data as (e). The results are identical to (b) where no clear signals are retrieved. Note that (b), (d) and (f) have the same amplitude scales.

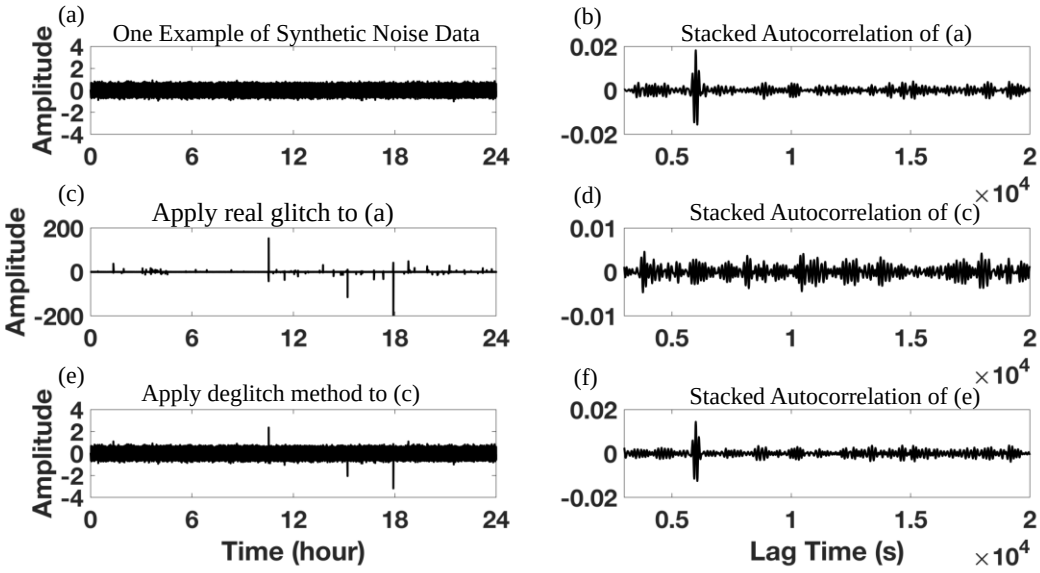

Figure 4.3 - (a) One example of Synthetic Noise Data, which is generated by the convolution of random noise and a synthetic R2 (Dirac function at 6000s). (b) Stack of 584 autocorrelations using all synthetic noise data as (a). The peak at 6000s is the synthetic R2. (c) One example of a real glitched record added to (a). (d) Stack of 584 autocorrelations using all synthetic data with glitches as (c). The R2 signal at 6000s is not clear. (e) Deglitching applied to the waveform in (c). (f) Stack of 584 autocorrelations using all deglitched data as (e). The R2 signal at 6000s can be clearly retrieved.

4.2.2. Calculating and Stacking Autocorrelations

Before the calculation of autocorrelograms, we applied temporal balance and spectral whitening, implemented with the running-absolute-mean normalization method in the time and frequency domains (Bensen et al., 2007) to remove the effects of non-stationary signals in the daily continuous data. The daily autocorrelograms were

computed by inverse Fourier transform of the power spectra of the vertical-component ambient noise signals bandpass filtered from 0.005 to 0.01Hz and normalized to the zero-lag value. The root-mean-square ratio selection (RMSR_S) was used to remove epochs with non-stationary phases (Jinyun Xie et al., 2020), resulting in reduction of the dataset by 9-15% depending on window parameters chosen (Figure 4.4). The signal window was selected as 5600-6400s and the noise window as 4800-5500s. The threshold value G for RMSR_S was set as 1.02. After the application of RMSR_S, 508 autocorrelation functions from a total of 584, i.e., 87%, were included in the final stack. Figure 4.4 shows tests of different signal and noise window selections in RMSR_S and the corresponding binary a^k values. The tests give almost identical results. Finally, the daily autocorrelograms were stacked to retrieve R_2 surface waves using both linear stacking (LS) and time-frequency domain phase-weighted stacking (tf-PWS) (G. Li et al., 2018; Schimmel & Gallart, 2007). In this study, we empirically chose the power of tf-PWS as 2 (Hable et al., 2019; Haned et al., 2016; Schimmel et al., 2011; Yan et al., 2019; Zeng et al., 2017), which is a common selection for Earth data analysis. Figure 4.5 shows tests for different exponents in the tf-PWS. Figure 4.6 is a synthetic test designed to demonstrate the efficiency of tf-PWS to enhance coherent signals.

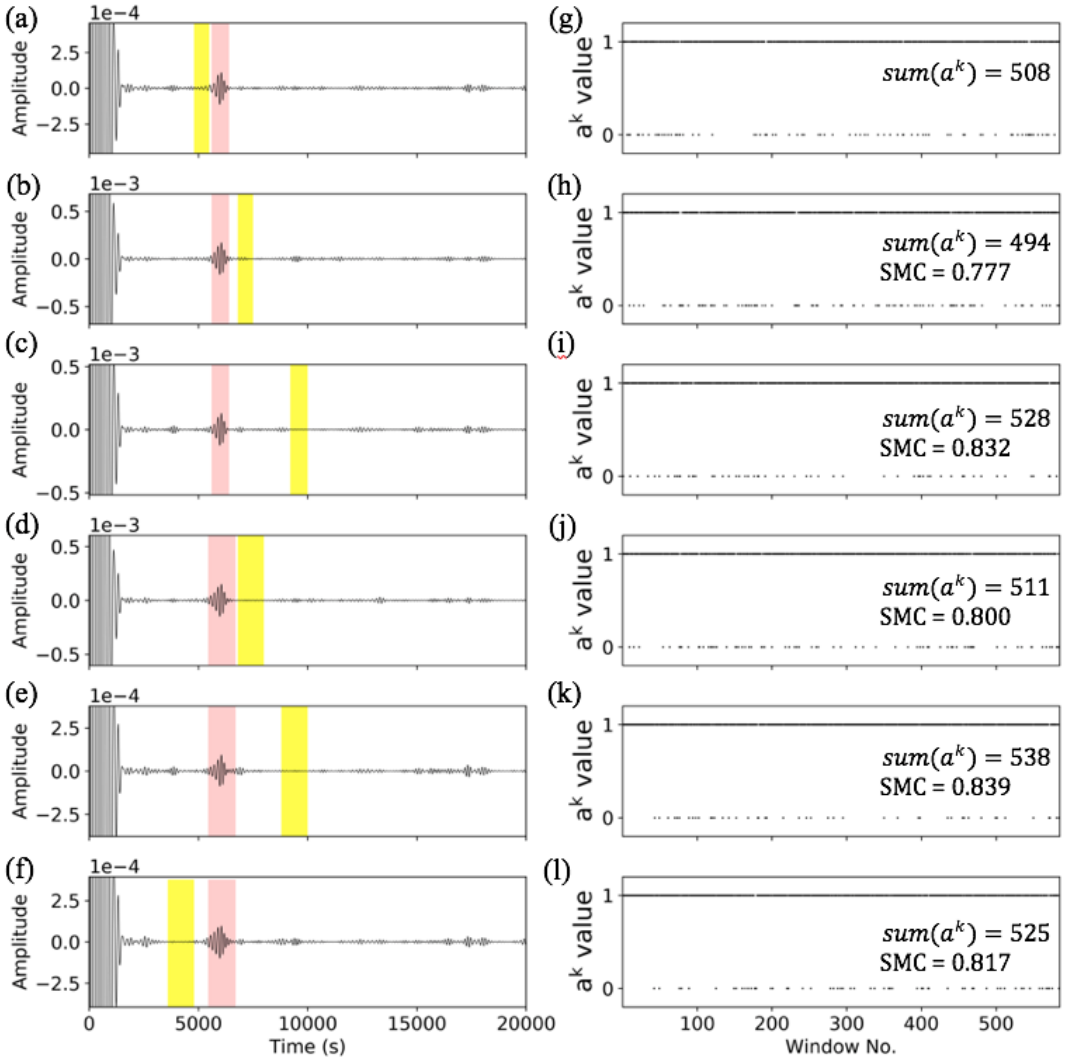

Figure 4.4 - Figures on left show different combinations of signal (pink) and noise (yellow) windows selected for the RMSR_S data selection. Figure (a) shows the windows used in the analysis presented in the paper (same as Figure 4.7g). The right panels show the binary weighting value a^k of all 584 windows for the results in the corresponding left panels (black dots), total number of autocorrelation functions used in the final stack for different signal and noise window selections (i.e., the sum of a^k), and simple matching coefficients (SMC) values compared with the results in (a). The SMC value is the ratio of the identical windows selected resulting from different window choices. For example, the SMC of 0.777 between (g) and (h) indicated that 77.7% of binary a^k values for the results in Figures (a) and (b) are identical. Window selections for RMSR_S are: (a) signal 5600-6400s, noise 4800-

5500s; (b) signal 5600-6400s, noise 6800-7500s; (c) signal 5600-6400s, noise 9200-10000s; (d) signal 5400-6700s, noise 6800-8000s; (e) signal 5400-6700s, noise 8800-10000s; (f) signal 5400-6700s, noise 3600-4800s.

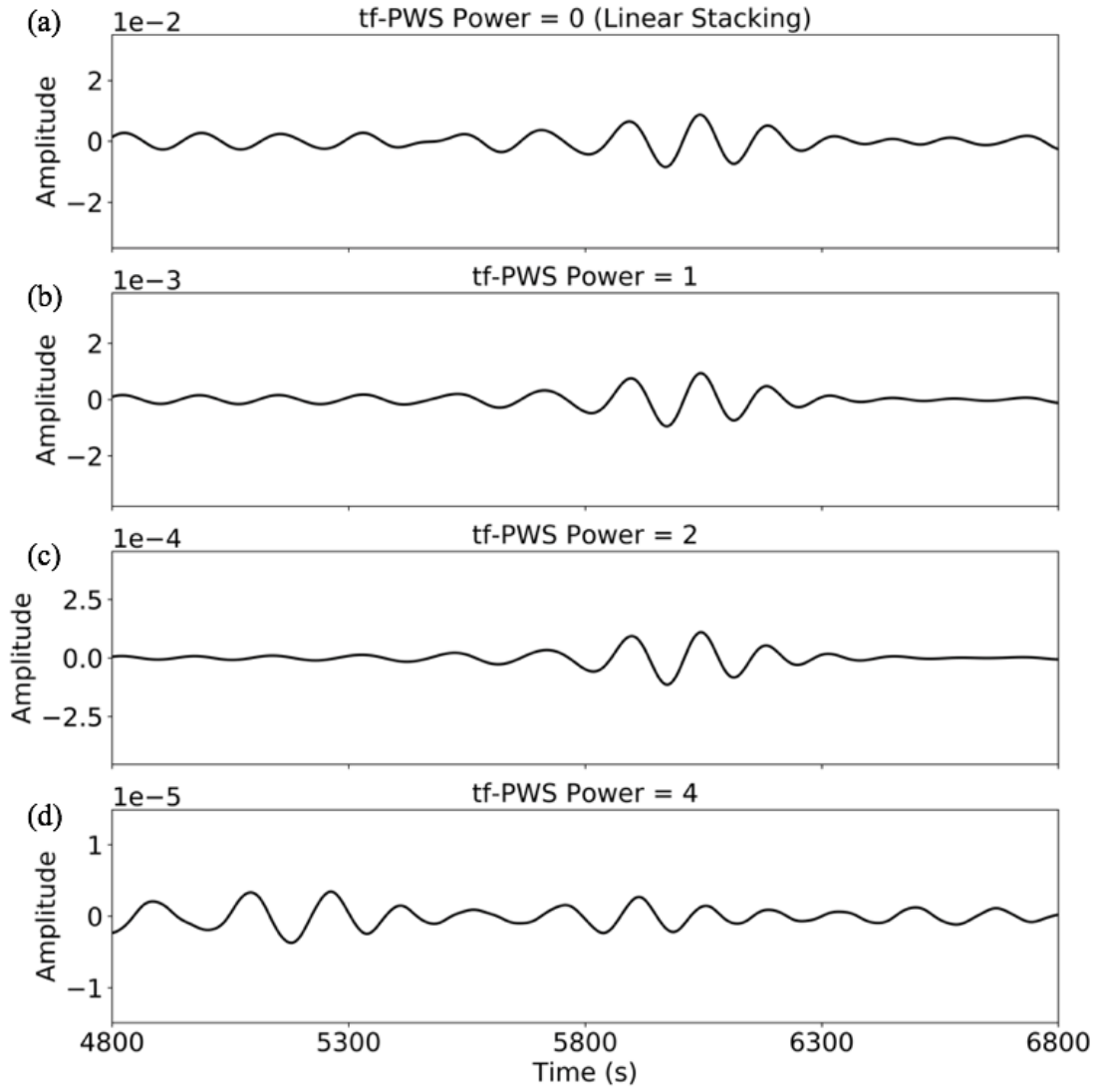

Figure 4.5 - (a) Same as Figure 4.7f, where the power of tf-PWS $\gamma = 0$ (linear stacking). (b) Same as (a) but for $\gamma = 1$. (c) Same as Figure 4.7h, where the power of tf-PWS $\gamma = 2$. (d) Same as (c) but for $\gamma = 4$, which will generate strong waveform distortion.

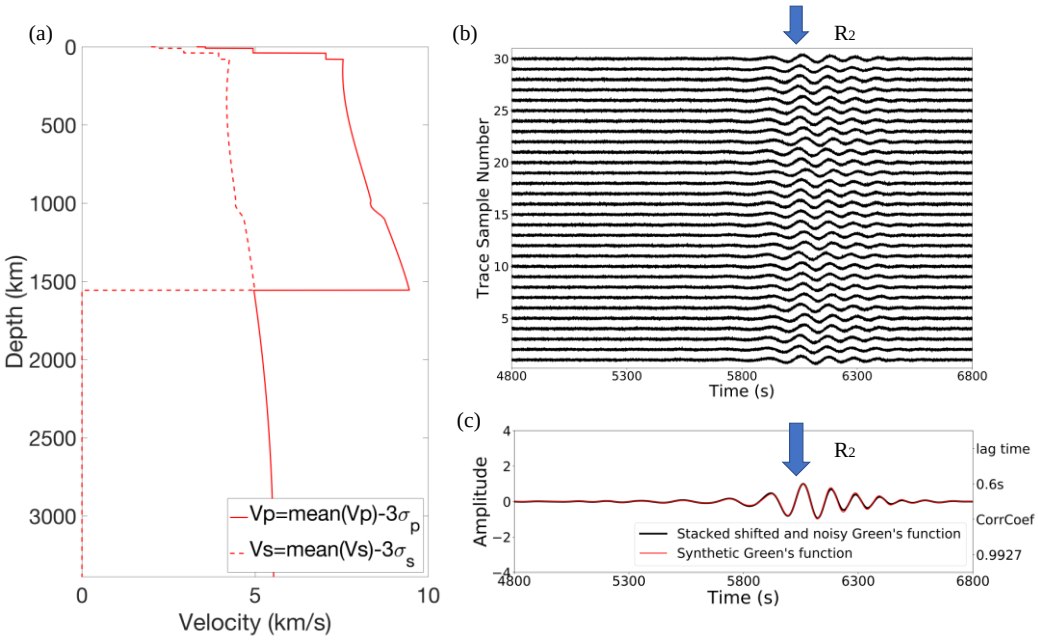

Figure 4.6 - (a) The P- and S-wave velocity model that is 3 standard deviations lower than the mean velocity derived from the probabilistic inversion (red model in Figure 4.9a) (Stähler et al., 2021) (b) 30 examples of a total of 600 shifted and noisy Green's functions of the velocity model in (a). (c) Comparison between the tf-PWS stacked shifted and noisy Green's function and the original synthetic Green's function. The correlation time shift and correlation coefficient between the red and black curve are shown on the right. The positive time shift means the black curve travels slower than the red curve.

4.3. Results and Discussion

4.3.1. Autocorrelation Results of R_2 Surface Waves

A signal that we interpret as the Mars orbiting Rayleigh wave R_2 is prominent at ~6000s in the vertical-component ambient noise autocorrelations filtered between 0.005

and 0.01Hz with both linear (Figures 4.7a and 4.7b) and tf-PWS stacking (Figures 4.7c and 4.7d). With the application of RMSR_S (Jinyun Xie et al., 2020), the R_2 signal is more prominent (Figures 4.7e to 4.7h). Bootstrap calculations using a subset of the whole dataset further suggest the R_2 phase identification is robust (Figure 4.8). In the following, we applied FTAN (Bensen et al., 2007; Levshin et al., 1992) to calculate the group velocities between 115 and 200s (Figures 4.9b and 4.10) for the stacked waveform using both RMSR_S and tf-PWS (Figure 4.7h) and compared these with the synthetic group dispersion curves of several Martian 1-D velocity models (Figure 4.9a; Stähler et al., 2021). Synthetic R_2 seismograms were also generated to compare with the observed R_2 waveform in Figure 4.7h (Figure 4.9c).

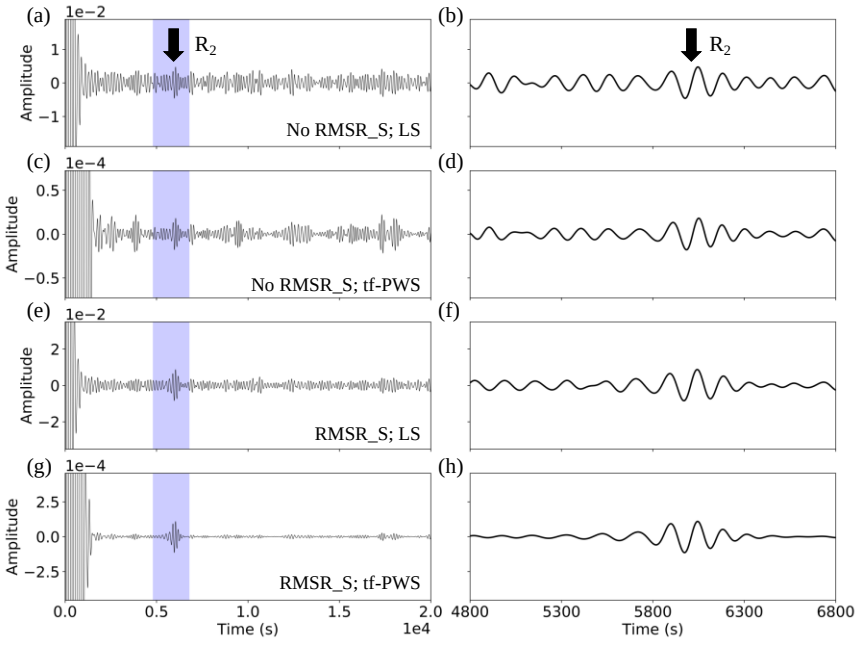

Figure 4.7 - (a) Linearly stacked (LS) autocorrelation filtered between 0.005 and 0.01Hz without the application of root-mean-square ratio selection (RMSR_S). (b) The R_2 signal of (a) between 4800 and 6800s (blue shaded area in (a)). (c) Same as (a) but applying time-frequency domain phase-weighted stacking (tf-PWS). (d) The R_2 signal of (c) between 4800 and 6800s (blue shaded area in (c)). (e) Same as (a) but applying RMSR_S. (f) The R_2 signal of (e) between 4800 and 6800s (blue shaded area in (e)). (g) Same as (e) but applying tf-PWS. (h) The R_2 signal of (g) between 4800 and 6800s (blue shaded area in (g)). The stacked autocorrelation in (g) and (h) show the most prominent R_2 signal and is used to compare with the synthetic results. After the application of RMSR_S, 508 autocorrelation functions among total 584 were maintained for the final stack.

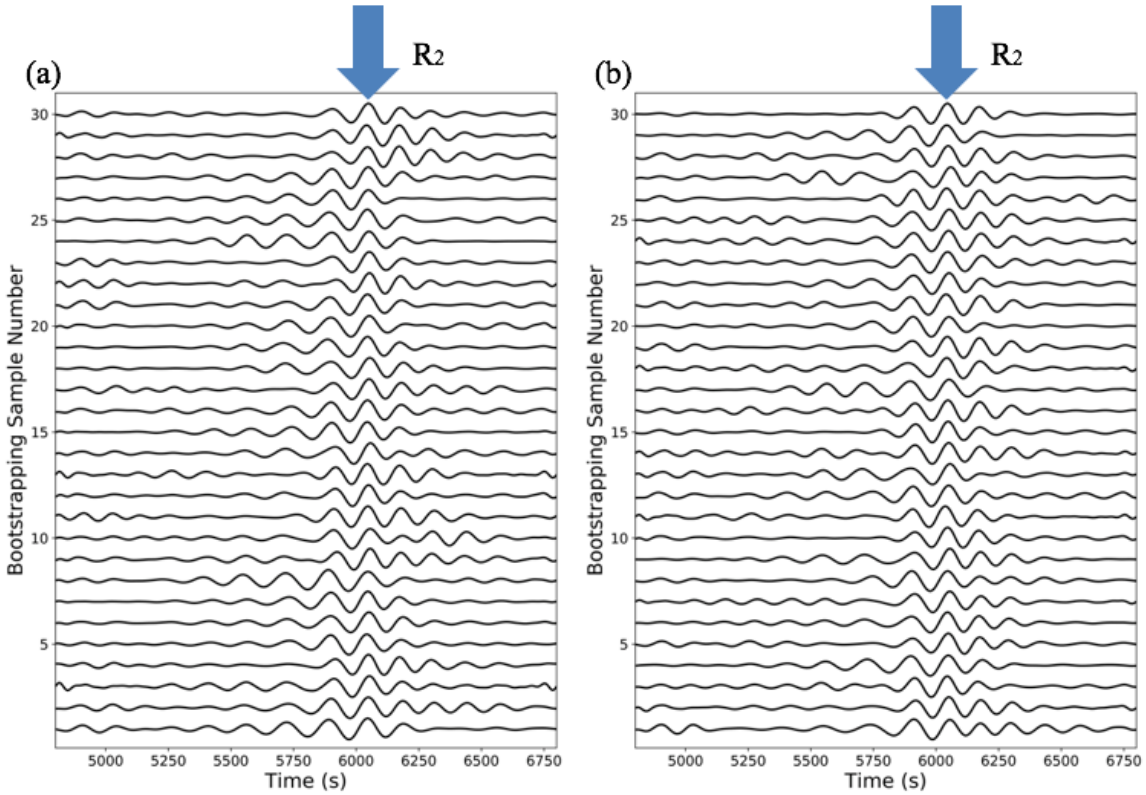

Figure 4.8 - (a) Bootstrap calculations for the autocorrelograms filtered between 0.005 and 0.01Hz without the application of RMSR_S, which followed the same processing steps as Figure 4.7d. (b) Bootstrap calculations for the autocorrelograms

filtered between 0.005 and 0.01Hz with the application of RMSR_S, which followed the same processing steps as Figure 4.7h.

4.3.2. Comparison with the Synthetic Group Dispersion Curves and Seismograms

We calculated synthetic group velocity dispersion curves for a set of velocity models (Figure 4.9a) derived from a probabilistic inversion to fit the tidal Love number k_2, moment of inertia and seismic traveltimes (Stähler et al., 2021) for comparisons to the group velocities (Figure 4.9b) derived from the stacked autocorrelation in Figure 4.7h. The FTAN-measured group velocities are compatible with the velocity model 3 standard deviations lower than the mean velocity of Stähler et al. (2021) (Figure 4.9b).

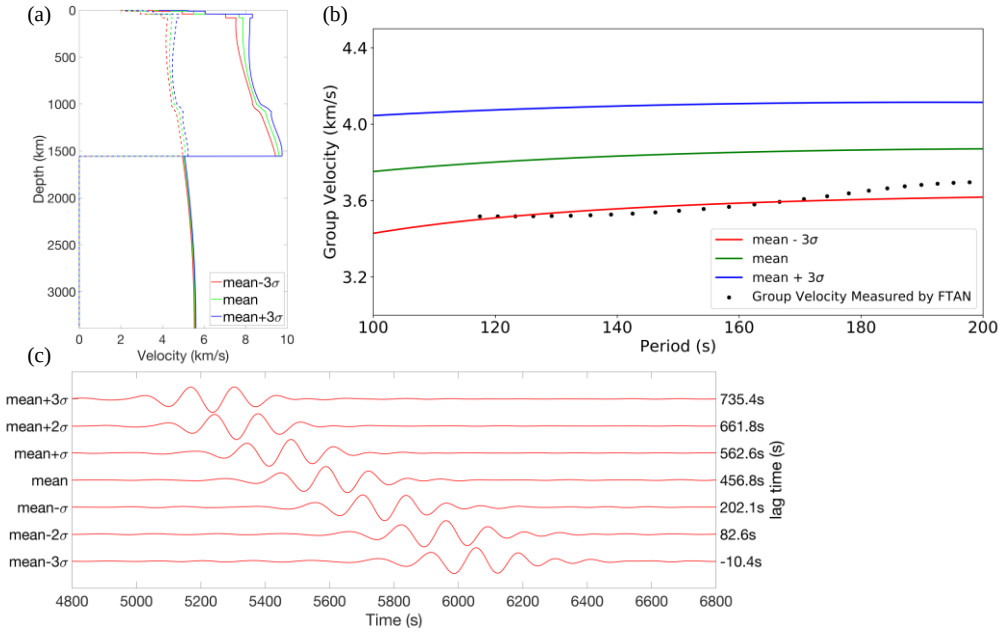

Figure 4.9 - (a) Probabilistic inversion of the Martian velocity models in Stähler et al. (2021). The velocity models range from 3 standard deviations lower to 3 standard

deviations higher than the mean velocity. (b) The group dispersion curves for different velocity models shown in (a) (solid lines) and the group velocities measured by frequency-time analysis (FTAN) of Figure 4.7h (black dots). (c) Synthetic seismograms filtered between 0.005 and 0.01Hz for different velocity models shown in (a). The lag time is the cross-correlation time shift between the synthetic seismograms and the stacked vertical-component autocorrelation shown in Figure 4.7h. The positive lag time means that the observed R_2 phase propagates slower than the synthetics and vice versa.

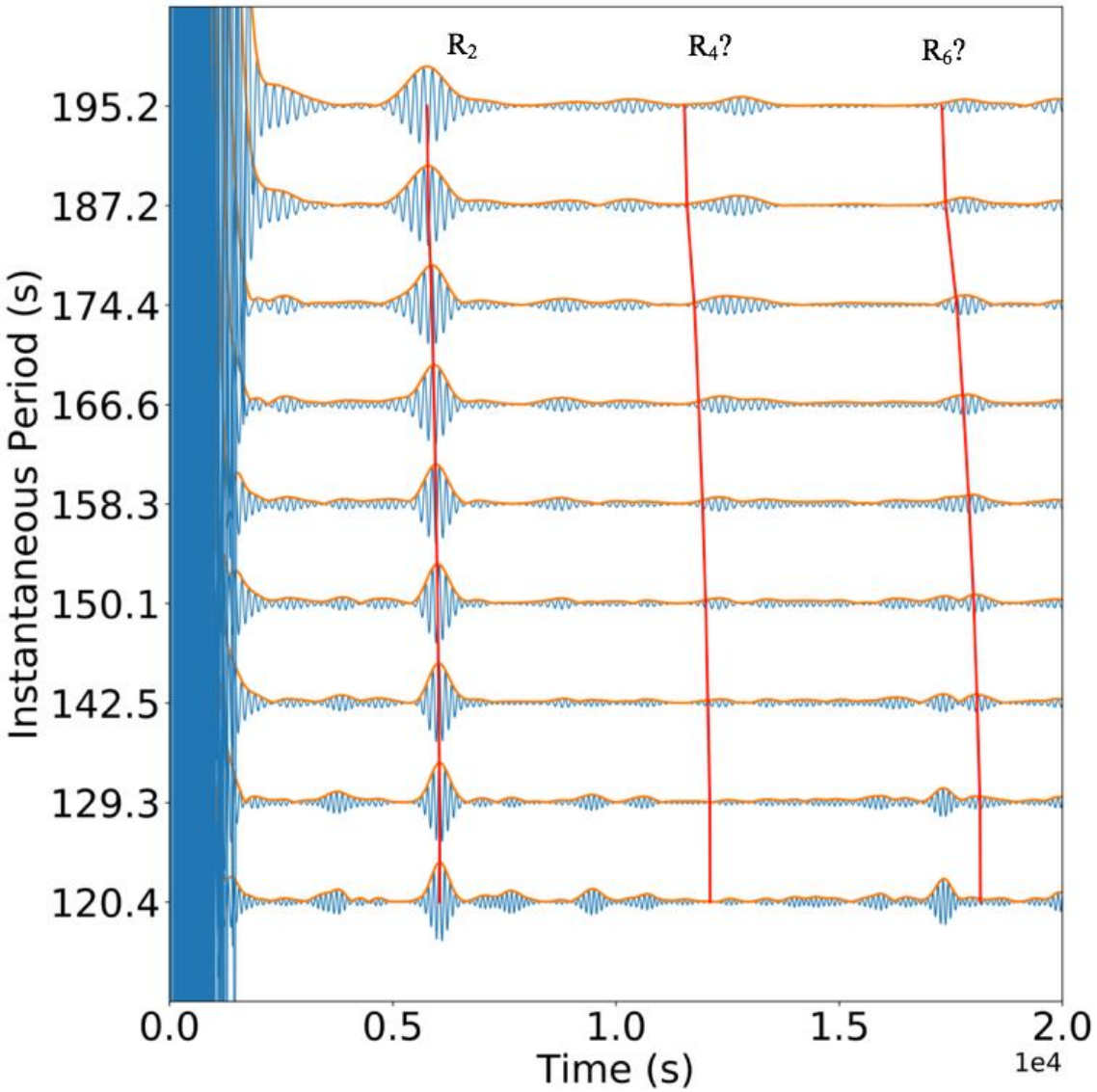

Figure 4.10 - Frequency-Time Analysis (FTAN) for the stacked autocorrelation in Figure 4.7g. The blue waveforms are the narrow bandpass filtered waveforms near the instantaneous periods. The instantaneous periods are listed on the left of each narrow bandpass filtered waveform. The orange waveforms are the envelope functions of the blue waveforms, which are used to determine group arrival times. The red curves mark 1, 2 and 3 times the picked R_2 group arrival time. The locations of expected R_4 and R_6 arrivals are also shown.

The R_2 Rayleigh waves can travel along any or all great circle paths on the Martian surface and possess travel distances that vary due to the planet's ellipticity ($\varepsilon = 0.00589$) (Jun Xie & Ni, 2019). Jun Xie and Ni (2019) discussed the effects of ellipticity on the group velocity estimation of the Earth orbiting surface waves, concluding that the effects are negligible. Accounting for the travel distance variations of R_2 surface waves, we simulated and then calculated a weighted mean of the synthetic Green's functions for a range of radii between the polar and equatorial radius (3376.2 – 3396.2km) using the direct solution method (DSM) software (Geller & Takeuchi, 1995; Kawai et al., 2006; Takeuchi et al., 1996). The mean synthetic was almost identical to the synthetic Green's functions using the mean Martian radius (3389.5km) (Figure 4.11). The synthetic Green's functions were then convolved with a source wavelet (Figure 4.12), estimated from the second zero-crossing of the side lobes of the autocorrelation near zero-lag (Erhan & Nowack, 2020; Yilmaz, 2001), to produce the synthetic R_2 seismograms.

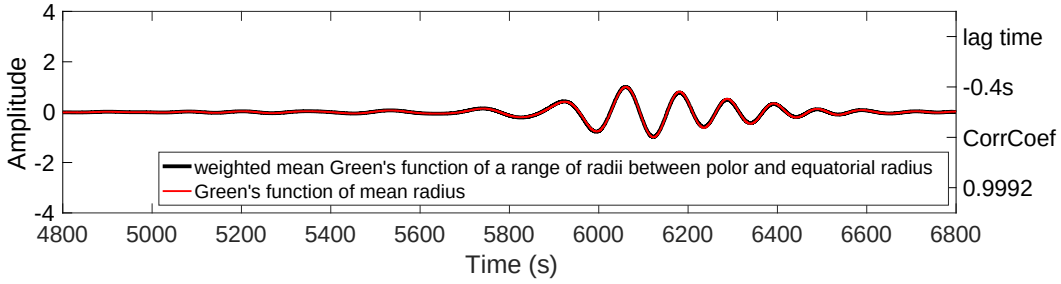

Figure 4.11 - The red curve is the synthetic Green's function with the mean radius (3389.5km), while the black one is the weighted mean Green's function of a range of radii between polar (3376.2km) and equatorial (3396.2km) radius using the velocity model in Figure 4.6a. The correlation time shift and correlation coefficient between the red and black curve are shown on the right. The negative time shift means the black curve travels faster than the red curve.

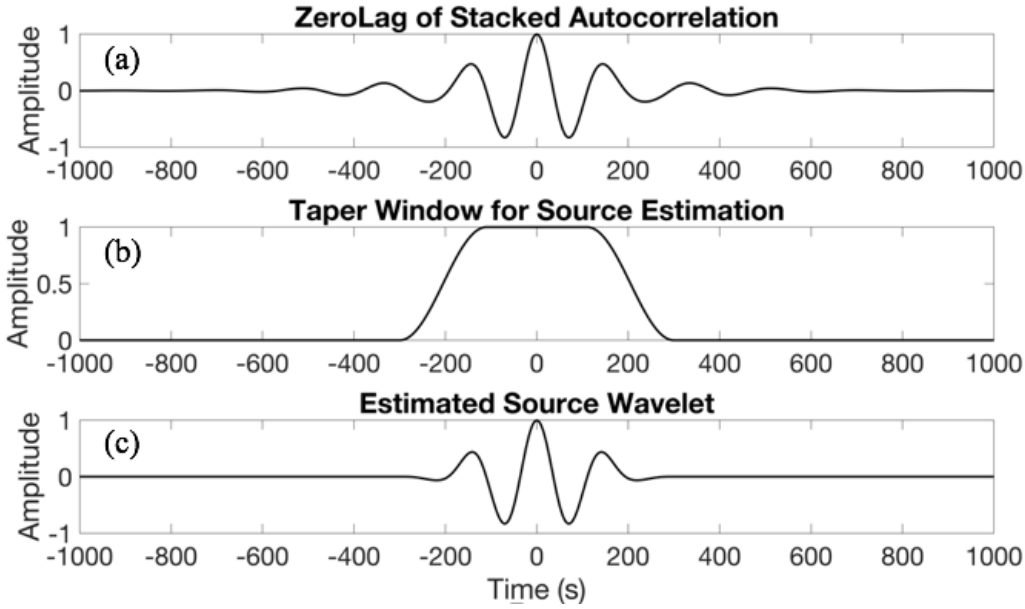

Figure 4.12 - (a) The zero-lag of the stacked autocorrelation shown Figure 4.7g. (b) Taper function used for the source wavelet estimation. (c) Estimated source wavelet obtained by multiplying the waveforms in (a) and (b).

We generated synthetic seismograms for the velocity models (Figure 4.9a) for comparisons to Figure 4.7h (Figure 4.9c). The time lag indicated on Figure 4.9c is the cross-correlation time shift between the observed R_2 (Figure 4.7h) and each individual synthetic seismogram, where positive values correspond to the travel time delays of the observed R_2 Rayleigh waves. The time lags are positive for velocity models from 3 standard deviations above the mean to 2 standard deviations lower than the mean velocity, and change sign at 3 standard deviations lower (Figure 4.9c). The waveform comparison (Figure 4.9c) also suggests that the upper mantle velocity model of Mars may be slightly slower on average than predicted by the mean value of the Stähler et al. (2021) model.

4.3.3. Monte Carlo Inversion for the Martian Upper Mantle Velocity

We employed a Monte Carlo inversion in which we perturbed the velocity in the depth range 40 to 700km, suggested by the Rayleigh wave sensitivity kernels (Figure 4.13), to better constrain the upper mantle seismic structures of Mars. For the starting model, we chose the velocity model from Stähler et al. (2021) that produced the best fit to the observation (Figure 4.7h): This was the model 3σ lower than the mean velocity (Figures 4.9b and 4.9c). For each iteration, we randomly perturbed the starting velocity model 10 times and calculated the DSM (Kawai et al., 2006) synthetic seismograms for these 10 new velocity models. We next computed the correlation time shifts and correlation coefficients between the observed R_2 (Figure 4.7h) and the synthetic R_2

waveforms of these 10 models. The model with smallest absolute correlation time shifts and highest correlation coefficients was used for the next iteration. We repeated the same procedure for three iterations since the misfit increased upon further perturbation of the velocity model.

Figures 4.14a and 4.14b show the upper mantle P- and S-wave velocity model update during each iteration of the Monte Carlo inversion, and the right 4 panels (Figures 4.14c to 4.14f) illustrate the comparisons between the observed R_2 (Figure 4.7h) and the synthetic seismograms of the best model in each iteration. Compared to the starting model, the final upper mantle velocity model after three iterations (black model in Figures 4.14a and 4.14b; Table 1) increases the correlation coefficients and reduces the absolute correlation time shifts between the observed and synthetic R_2 waveforms by a factor of 5 (Figure 4.14f). The model perturbation between the starting and final velocity model is shown in Figure 4.15. Figures 4.16 and 4.17 show that our final model can fit the body-wave traveltime picks derived using different picking methods (Stähler et al., 2021).

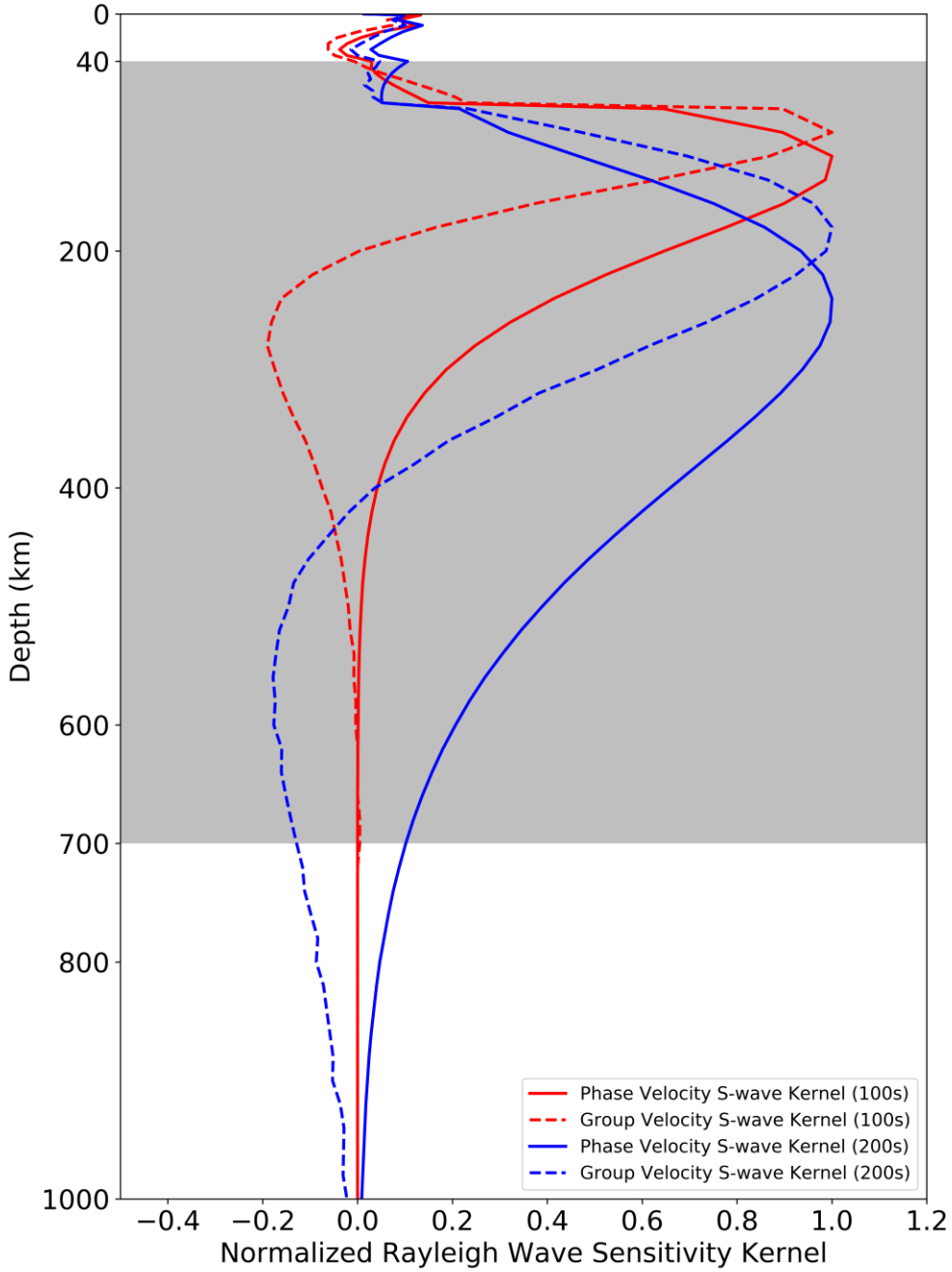

Figure 4.13 - Normalized Rayleigh wave sensitivity kernel of the velocity model in Figure 4.6a for periods of 100s (red curve) and 200s (blue curve). The phase and group velocity sensitivity kernels are plotted in solid and dashed lines, respectively. The gray-shaded area is the depth range that we perturbed during the Monte Carlo inversion.

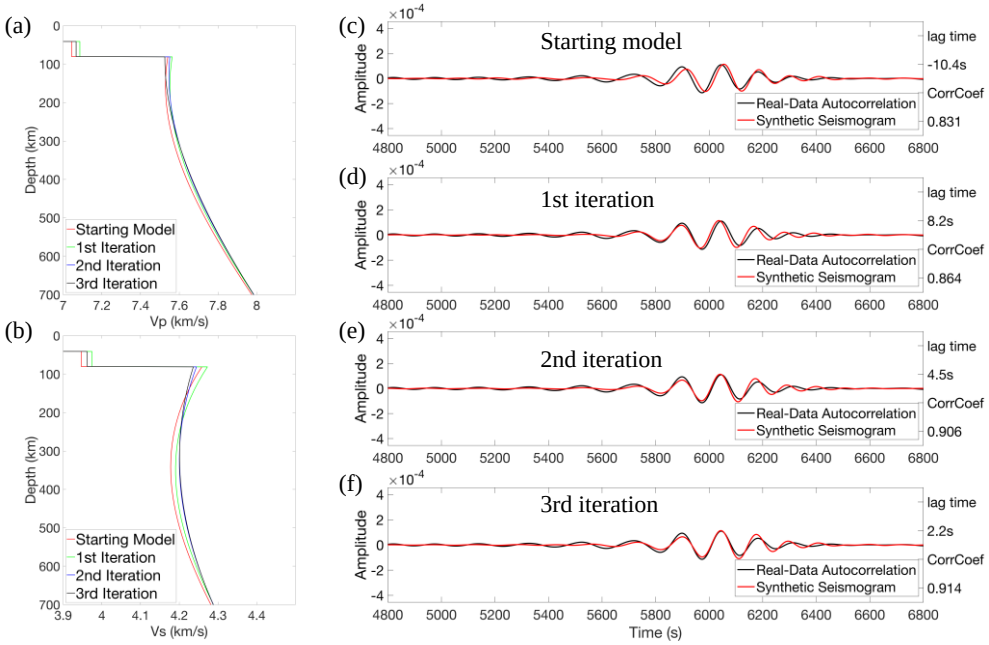

Figure 4.14 - P- and S-wave velocity models of the Martian upper mantle (40-700 km) updated during the Monte Carlo inversion are shown in (a) and (b) respectively. The red curve is the mean-3σ model in Stähler et al. (2021). Comparisons between the synthetic R_2 waveforms and real-data autocorrelation (Figure 4.7h) filtered between 0.005 and 0.01Hz for the starting velocity model (The red model in (a) and (b)) and the velocity models after 1st (The green model in (a) and (b)), 2nd (The blue model in (a) and (b)) and 3rd (The black model in (a) and (b)) iteration are shown in (c) – (f). The correlation time shifts and correlation coefficients between synthetic and observed R_2 waveforms are listed at the right side of (c) – (f). Positive lag time means that the observed R_2 phase propagates slower than synthetics and vice versa.

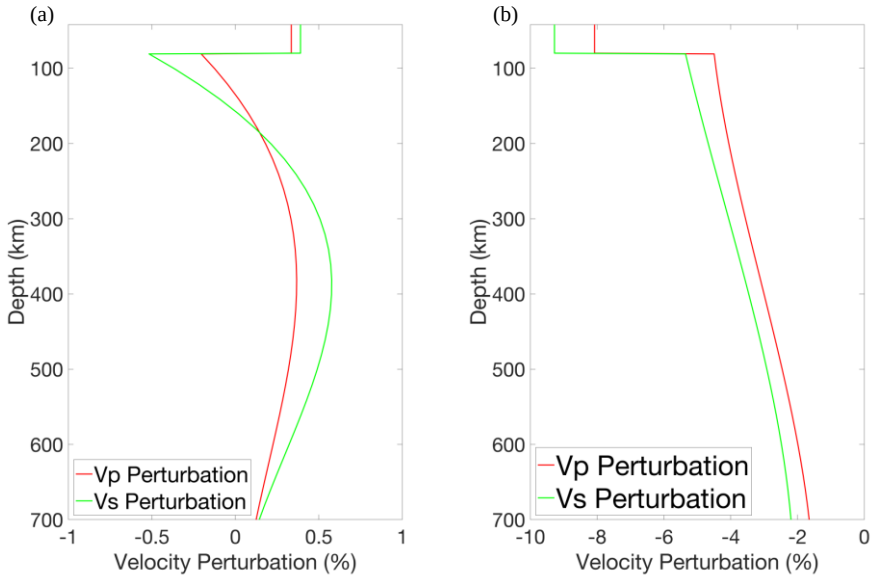

Figure 4.15 - (a) P- and S-wave velocity perturbation between the final model (black model in Figures 4.14a and 4.14b) and starting model (red model in Figures 4.14a and 4.14b) of the Monte Carlo inversion. (b) P- and S-wave velocity perturbation percentage between the final model of the Monte Carlo inversion (black model in Figures 4.14a and 4.14b) and the mean velocity model in Stähler et al. (2021) (green model in Figure 4.9a). At shallower depths (< 40km) there were no perturbations.

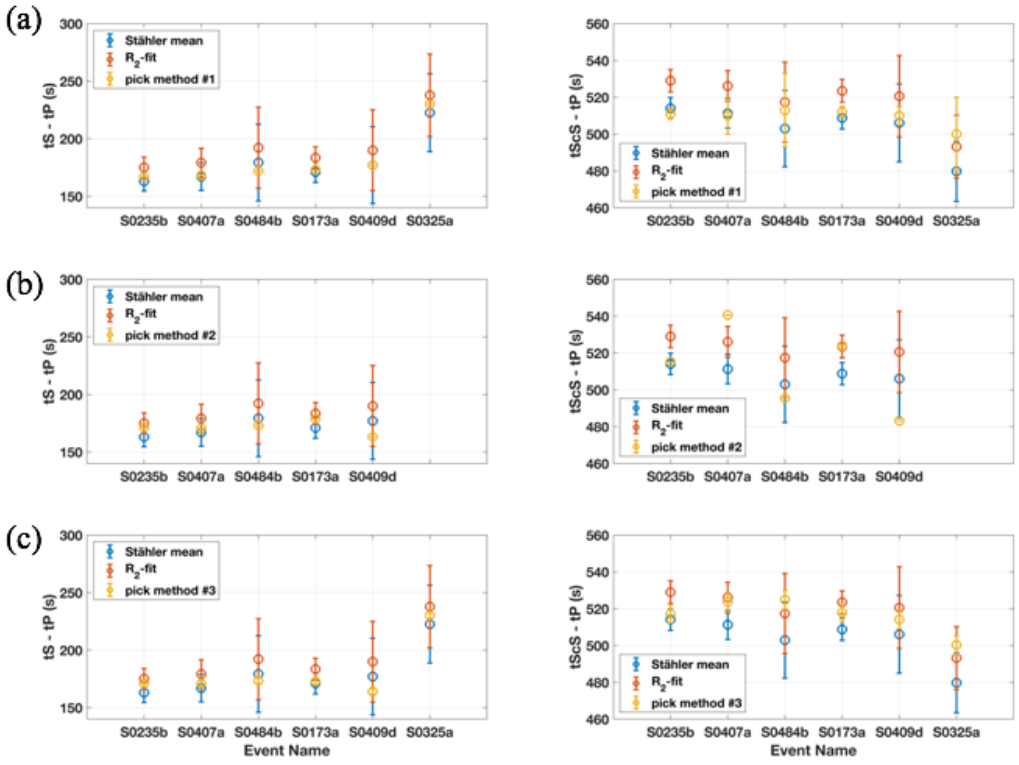

Figure 4.16 - (a) The comparison between body-wave traveltime picks (tS – tP on left and tScS – tP on right) derived from picking method #1 (Time-domain envelope picking) and the synthetic traveltimes of the mean velocity model in Stähler et al. (2021) (green model in Figure 4.9a) and the best model to fit R_2 after Monte Carlo inversion (black model in Figures 4.14a and 4.14b). (b) Same as (a) but the observed body-wave traveltime picks are derived from picking method #2 (Joint SH-correlation and backazimuth analysis). (c) Same as (a) but the observed body-wave traveltime picks are derived from picking method #3 (Vespagram analysis). Our R_2-fit model appears acceptable given the uncertainty in the original picks (see Figure 4.17).

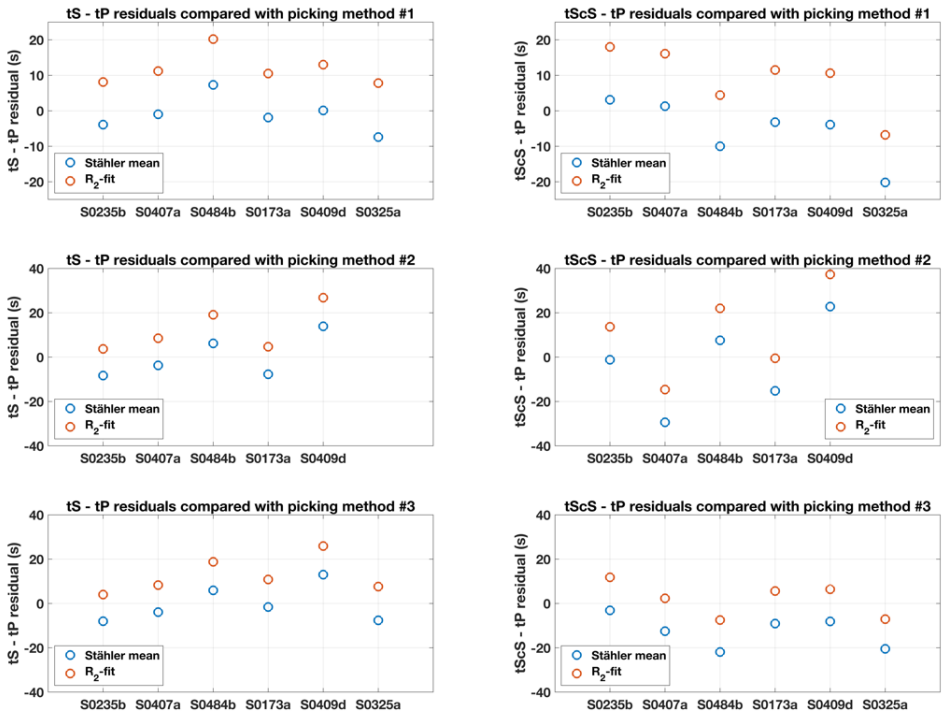

Figure 4.17 - (a) the traveltime residuals of the mean velocity in Stähler et al. (2021) and R2-fit model compared with the observed traveltime picks derived from picking method #1 (Time-domain envelope picking) (b) Same as (a) but compared with the observed body-wave traveltime picks derived from picking method #2 (Joint SH-correlation and backazimuth analysis). (c) Same as (a) but compared with the observed body-wave traveltime picks derived from picking method #3 (Vespagram analysis).

The S-wave low-velocity zone (LVZ), extending to ~400km depth, is clearly observed on the Monte-Carlo inverted S-wave velocity model (Figure 4.14b), but the S-wave velocity has been increased compared to the starting model at depths > 200 km and is reduced at depths < 200 km (Figure 4.15a). Geophysical modeling indicates that the S-wave LVZ may reach depths of 400 to 600km (Khan et al., 2021), and has been predicted

from laboratory measurement of seismic velocity for several representative Martian upper mantle compositions (Xu et al., 2021). The S-wave LVZ is thought to result from the steep thermal gradient in the Martian lithosphere arising from the thick conductive mantle (Khan et al., 2021). Moreover, a weak S-wave shadow zone is observed in epicentral distances range ~40 to 60 degrees, providing independent evidence to support the presence of an S-wave LVZ within the Martian lithosphere (Giardini et al., 2020; Khan et al., 2021; Knapmeyer-Endrun & Kawamura, 2020). No equivalent LVZ is required in the upper mantle P-wave model (Figure 4.14a) as P-wave velocity is much less sensitive to temperature (Khan et al., 2021).

Table 1 - P- and S-wave velocity model after three iterations of Monte Carlo method (black model in Figures 4.14a and 4.14b). The velocity model uncertainty is not available for the depth above 40km because we did not perturb the velocity value in this depth range during Monte Carlo inversion.

Depth Range (km)	P-wave Velocity (km/s)	P-wave Velocity Uncertainty (km/s)	S-wave Velocity (km/s)	S-wave Velocity Uncertainty (km/s)
0 - 1	3.3087	N/A	1.9939	N/A
1 - 9.6	3.5660	N/A	2.1209	N/A
9.6 - 39.8	4.9412	N/A	2.9411	N/A
39.8 - 40.8	6.4184	0.0310	3.9537	0.0089
40.8 - 80	7.0667	0.0354	3.9619	0.0231
80 - 100	7.5489	0.0124	4.2622	0.0059
100 - 120	7.5445	0.0143	4.2509	0.0078
120 - 140	7.5418	0.0160	4.2405	0.0094
140 - 160	7.5407	0.0175	4.2313	0.0109
160 - 180	7.5413	0.0188	4.2230	0.0122
180 - 200	7.5433	0.0199	4.2157	0.0133
200 - 220	7.5469	0.0209	4.2093	0.0143
220 - 240	7.5518	0.0216	4.2039	0.0152
240 - 260	7.5582	0.0223	4.1994	0.0159
260 - 280	7.5660	0.0227	4.1957	0.0165
280 - 300	7.5750	0.0231	4.1929	0.0169
300 - 320	7.5853	0.0233	4.1909	0.0172
320 - 340	7.5969	0.0234	4.1898	0.0174
340 - 360	7.6096	0.0233	4.1894	0.0175
360 - 380	7.6234	0.0232	4.1898	0.0175
380 - 400	7.6382	0.0229	4.1909	0.0175
400 - 420	7.6541	0.0226	4.1927	0.0173
420 - 440	7.6710	0.0222	4.1952	0.0170
440 - 460	7.6888	0.0217	4.1983	0.0167
460 - 480	7.7075	0.0211	4.2021	0.0163
480 - 500	7.7270	0.0204	4.2065	0.0159
500 - 520	7.7474	0.0197	4.2115	0.0154
520 - 540	7.7684	0.0190	4.2170	0.0148
540 - 560	7.7902	0.0182	4.2231	0.0142
560 - 580	7.8126	0.0174	4.2297	0.0136
580 - 600	7.8356	0.0166	4.2368	0.0130
600 - 620	7.8591	0.0157	4.2443	0.0123
620 - 640	7.8832	0.0149	4.2523	0.0116
640 - 660	7.9077	0.0140	4.2607	0.0110
660 - 680	7.9327	0.0132	4.2695	0.0103
680 - 700	7.9580	0.0124	4.2787	0.0096

4.4. Conclusion

We applied the autocorrelation method to the InSight continuous vertical-component seismic data to provide the R_2 Rayleigh waves that propagate around Mars for one cycle. The R_2 surface waves are identified at ~6000s in the autocorrelations in the frequency band 0.005 to 0.01Hz (Figure 4.7). Comparing synthetic group dispersion curves (Figure 4.9b) and seismograms (Figure 4.9c) from a set of Martian velocity models in Figure 4.9a, we found that the upper mantle shear velocity structure is slower than the mean model derived from the joint inversion of multiple geophysical datasets (Stähler et al., 2021). A Monte Carlo inversion was employed to perturb the velocity model 3 standard deviations lower than the mean velocity model of Stähler et al. (2021). We obtained a model that better fits the observed R_2 Rayleigh waves than the starting model (Figure 4.14f). The R_2 model is different from the mean-3σ model in Stähler et al. (2021) with velocities slower at depths < 200 km and faster at depths > 200 km (Figures 4.14b and 4.15). The S-wave LVZ extends to a depth of ~400km in the Martian upper mantle (Figure 4.14b), consistent with the S-body wave shadow zone observed in the Marsquake data (Giardini et al., 2020; Khan et al., 2021; Knapmeyer-Endrun & Kawamura, 2020), geophysical inversion (Khan et al., 2021) and high-pressure laboratory experiments (Xu et al., 2021).

Chapter 5

Conclusion

In this thesis, the autocorrelation analysis was applied to the continuous ambient noise data recorded by InSight seismic station to reconstruct the subsurface structure of Mars. In Chapter 2, we showed the autocorrelation reflectivity in different frequency bands using the data recorded from February to August 2019. From high frequency (0.625-2.5Hz) autocorrelation series, we can observe P-wave and S-wave reflection at Moho. The estimated Moho depth is ~35km, which agrees with the results from gravity inversion (Zuber, 2000). The Vp/Vs ratio is ~1.83, suggesting the Martian crust is made of basaltic or andesitic rocks. The P-wave reflection responses from olivine-wadsleyite transition and core-mantle boundary were recovered from low frequency ambient noise autocorrelation. The ringwoodite-perovskite transition is not observed as the temperature and pressure condition at Martian core-mantle boundary cannot trigger this phase transition. Given several reference velocity models (Khan et al., 2018; Panning et al.,

2017; Yoshizaki & McDonough, 2020), The depths of olivine-wadsleyite transition and core-mantle boundary are put at 1110-1170km and 1520-1600km, respectively.

However, Kim et al. (2021) and Barkaoui et al. (2021) pointed out that the observed signals in Deng and Levander (2020) are from quasi-periodic glitches rather than real reflection responses from seismic discontinuities. In Chapter 3, we calculated and stacked the autocorrelations using three types of datasets: (1) raw ambient noise data; (2) deglitched ambient noise data and (3) glitch-only data. The signals at ~285s and ~385s can be clearly retrieved from deglitched dataset but cannot be retrieved from glitch-only dataset. In raw data autocorrelation, these two signals can also be observed but the waveform is complicated as it is contaminated by the high-amplitude glitches. The autocorrelation test demonstrated the observation of the reflection response from deep Mars (e.g., olivine-wadsleyite transition and core-mantle boundary) was robust. The grid search was conducted to constrain the velocity models near CMB and improve the fit between observed and synthetic PcP phases (Figure 3.4). A 60km 1-layer velocity transition zone near Martian core-mantle boundary is derived to better match with the observed PcP compared with a sharp velocity drop (Figure 3.4).

In Chapter 4, we employed the ambient noise autocorrelation to derive another type of seismic wave, the surface wave that travels around the planet for one cycle (R_2). The synthetic group velocities and R2 waveforms were simulated for the reference velocity models in Stähler et al. (2021) to compare with the observed Mars orbiting surface wave. We found that the real upper mantle velocity structure of Mars maybe slightly slower than the mean model in Stähler et al. (2021). The Monte Carlo inversion

was applied to refine the upper mantle structure of Mars (40-700km), where an S-wave LVZ is observed in the final velocity model. The S-wave LVZ extends to a depth of ~400km in the Martian upper mantle (Figure 4.14b), consistent with the S-body wave shadow zone observed in the Marsquake data (Giardini et al., 2020; Khan et al., 2021; Knapmeyer-Endrun & Kawamura, 2020), geophysical inversion (Khan et al., 2021) and high-pressure laboratory experiments (Xu et al., 2021).

References

Anderson, D. L., Miller, W. F., Latham, G. V., Nakamura, Y., Toksöz, M. N., Dainty, A. M., et al. (1977). Seismology on Mars. *Journal of Geophysical Research*. https://doi.org/10.1029/js082i028p04524

Banerdt, W. B., Smrekar, S. E., Banfield, D., Giardini, D., Golombek, M., Johnson, C. L., et al. (2020). Initial results from the InSight mission on Mars. *Nature Geoscience*, *13*(3), 183–189. https://doi.org/10.1038/s41561-020-0544-y

Barkaoui, S., Lognonné, P., Kawamura, T., Stutzmann, É., Seydoux, L., de Hoop, M. V., et al. (2021). Anatomy of continuous mars seis and pressure data from unsupervised learning. *Bulletin of the Seismological Society of America*, *111*(6), 2964–2981. https://doi.org/10.1785/0120210095

Becker, G., & Knapmeyer-Endrun, B. (2018). Crustal thickness across the Trans-European Suture Zone from ambient noise autocorrelations. *Geophysical Journal International*. https://doi.org/10.1093/gji/ggx485

Becker, G., & Knapmeyer-Endrun, B. (2019). Crustal thickness from horizontal component seismic noise auto- and cross-correlations for stations in Central and Eastern Europe. *Geophysical Journal International*. https://doi.org/10.1093/gji/ggz164

Bensen, G. D., Ritzwoller, M. H., Barmin, M. P., Levshin, A. L., Lin, F., Moschetti, M. P., et al. (2007). Processing seismic ambient noise data to obtain reliable broad-band

surface wave dispersion measurements. *Geophysical Journal International*. https://doi.org/10.1111/j.1365-246X.2007.03374.x

Berg, E. M., Lin, F. C., Allam, A., Qiu, H., Shen, W., & Ben-Zion, Y. (2018). Tomography of Southern California Via Bayesian Joint Inversion of Rayleigh Wave Ellipticity and Phase Velocity From Ambient Noise Cross-Correlations. *Journal of Geophysical Research: Solid Earth*, *123*(11), 9933–9949. https://doi.org/10.1029/2018JB016269

Bertka, C. M., & Fei, Y. (1997). Mineralogy of the Martian interior up to core-mantle boundary pressures. *Journal of Geophysical Research: Solid Earth*. https://doi.org/10.1029/96jb03270

Böse, M., Stähler, S. C., Deichmann, N., Giardini, D., Clinton, J., Lognonné, P., et al. (2021). Magnitude Scales for Marsquakes Calibrated from InSight Data. *Bulletin of the Seismological Society of America*. https://doi.org/10.1785/0120210045

Breuer, D., Zhou, H., Yuen, D. A., & Spohn, T. (1996). Phase transitions in the Martian mantle: Implications for the planet's volcanic history. *Journal of Geophysical Research E: Planets*. https://doi.org/10.1029/96JE00117

Cai, A., Qiu, H., & Niu, F. (2022). Semi-Supervised Surface Wave Tomography With Wasserstein Cycle-Consistent GAN: Method and Application to Southern California Plate Boundary Region. *Journal of Geophysical Research: Solid Earth*, *127*(3), e2021JB023598. https://doi.org/10.1029/2021jb023598

Ceylan, S., Clinton, J. F., Giardini, D., Böse, M., Charalambous, C., Driel, M. van, et al. (2021). Companion guide to the marsquake catalog from InSight, Sols 0–478: Data content and non-seismic events. *Physics of the Earth and Planetary Interiors*, *310*(August 2020), 106597. https://doi.org/10.1016/j.pepi.2020.106597

Christensen, N. I. (1996). Poisson's ratio and crustal seismology. *Journal of Geophysical Research: Solid Earth*. https://doi.org/10.1029/95jb03446

Claerbout, J. F. (1968). Synthesis of a Layered Medium From its Acoustic Transmission Response. *Geophysics*. https://doi.org/10.1190/1.1439927

Clayton, R. W. (2020). Imaging the Subsurface with Ambient Noise Autocorrelations. *Seismological Research Letters*. https://doi.org/10.1785/0220190272

Clinton, J. F., Ceylan, S., van Driel, M., Giardini, D., Stähler, S. C., Böse, M., et al. (2021). The Marsquake catalogue from InSight, sols 0–478. *Physics of the Earth and Planetary Interiors*, *310*, 106595. https://doi.org/10.1016/j.pepi.2020.106595

Compaire, N., Margerin, L., Garcia, R. F., Pinot, B., Calvet, M., Orhand-Mainsant, G., et al. (2021). Autocorrelation of the Ground Vibrations Recorded by the SEIS-InSight Seismometer on Mars. *Journal of Geophysical Research: Planets*, *126*(4), 1–20. https://doi.org/10.1029/2020JE006498

Delph, J. R., Levander, A., & Niu, F. (2019). Constraining Crustal Properties Using Receiver Functions and the Autocorrelation of Earthquake-Generated Body Waves. *Journal of Geophysical Research: Solid Earth*.

https://doi.org/10.1029/2019JB017929

Deng, S., & Levander, A. (2020). Autocorrelation Reflectivity of Mars. *Geophysical Research Letters*, *47*(16). https://doi.org/10.1029/2020GL089630

Deng, S., & Levander, A. (2022). Autocorrelation R2 on Mars. *Geophysical Research Letters*, *49*(17), e2022GL099580. https://doi.org/10.1029/2022GL099580

Erhan, E., & Nowack, R. L. (2020). Application of non-stationary iterative time-domain deconvolution. *Studia Geophysica et Geodaetica*, *64*(1), 76–99. https://doi.org/10.1007/s11200-019-1165-z

Fei, Y. (2013). Simulation of the planetary interior differentiation processes in the laboratory. *Journal of Visualized Experiments : JoVE*. https://doi.org/10.3791/50778

Feng, J., Yao, H., Poli, P., Fang, L., Wu, Y., & Zhang, P. (2017). Depth variations of 410 km and 660 km discontinuities in eastern North China Craton revealed by ambient noise interferometry. *Geophysical Research Letters*. https://doi.org/10.1002/2017GL074263

Feng, J., Yao, H., Wang, Y., Poli, P., & Mao, Z. (2021). Segregated oceanic crust trapped at the bottom mantle transition zone revealed from ambient noise interferometry. *Nature Communications*, *12*(1), 1–8. https://doi.org/10.1038/s41467-021-22853-2

Frasier, C. W. (1970). Discrete Time Solution of Plane P-SV Waves in a Plane Layered Medium. *Geophysics*. https://doi.org/10.1190/1.1440085

Geller, R. J., & Takeuchi, N. (1995). A new method for computing highly accurate DSM synthetic seismograms. *Geophysical Journal International*, *123*(2), 449–470. https://doi.org/10.1111/j.1365-246X.1995.tb06865.x

Genova, A., Goossens, S., Lemoine, F. G., Mazarico, E., Neumann, G. A., Smith, D. E., & Zuber, M. T. (2016). Seasonal and static gravity field of Mars from MGS, Mars Odyssey and MRO radio science. *Icarus*. https://doi.org/10.1016/j.icarus.2016.02.050

Giardini, D., Lognonné, P., Banerdt, W., Pike, W., Christensen, U., Ceylan, S., et al. (2020). The Seismicity of Mars. *Nature Geoscience*. https://doi.org/10.1038/s41561-020-0539-8

Golombek, M., Warner, N. H., Grant, J. A., Hauber, E., Ansan, V., Weitz, C. M., et al. (2020). Geology of the InSight landing site on Mars. *Nature Communications*, *11*(1), 1–11. https://doi.org/10.1038/s41467-020-14679-1

Gorbatov, A., Saygin, E., & Kennett, B. L. N. (2013). Crustal properties from seismic station autocorrelograms. *Geophysical Journal International*. https://doi.org/10.1093/gji/ggs064

Grott, M., & Breuer, D. (2010). On the spatial variability of the martian elastic lithosphere thickness: Evidence for mantle plumes? *Journal of Geophysical Research*. https://doi.org/10.1029/2009JE003456

Hable, S., Sigloch, K., Stutzmann, E., Kiselev, S., & Barruol, G. (2019). Tomography of

crust and lithosphere in the western Indian Ocean from noise cross-correlations of land and ocean bottom seismometers. *Geophysical Journal International*, *219*(2), 924–944. https://doi.org/10.1093/gji/ggz333

Haned, A., Stutzmann, E., Schimmel, M., Kiselev, S., Davaille, A., & Yelles-Chaouche, A. (2016). Global tomography using seismic hum. *Geophysical Journal International*, *204*(2), 1222–1236. https://doi.org/10.1093/gji/ggv516

Hannemann, K., Papazachos, C., Ohrnberger, M., Savvaidis, A., Anthymidis, M., & Lontsi, A. M. (2014). Three-dimensional shallow structure from high-frequency ambient noise tomography: New results for the Mygdonia basin-Euroseistest area, northern Greece. *Journal of Geophysical Research: Solid Earth*, *119*(6), 4979–4999. https://doi.org/10.1002/2013JB010914

Haskell, N. A. (1953). The dispersion of surface waves on multilayered media*. *Bulletin of the Seismological Society of America*, *43*(1), 17–34. https://doi.org/10.1785/bssa0430010017

Herrmann, R. B. (2013). Computer programs in seismology: An evolving tool for instruction and research. *Seismological Research Letters*, *84*(6), 1081–1088. https://doi.org/10.1785/0220110096

Horleston, A. C., Clinton, J. F., Ceylan, S., Giardini, D., Charalambous, C., Irving, J. C. E., et al. (2022). The Far Side of Mars: Two Distant Marsquakes Detected by InSight. *The Seismic Record*, *2*(2), 88–99. https://doi.org/10.1785/0320220007

Jacob, A., Plasman, M., Perrin, C., Fuji, N., Lognonné, P., Xu, Z., et al. (2022). Seismic sources of InSight marsquakes and seismotectonic context of Elysium Planitia, Mars. *Tectonophysics*, *837*, 229434. https://doi.org/10.1016/j.tecto.2022.229434

Karakostas, F., Schmerr, N., Maguire, R., Huang, Q., Kim, D., Lekic, V., et al. (2021). Scattering Attenuation of the Martian Interior through Coda-Wave Analysis. *Bulletin of the Seismological Society of America*, *111*(6), 3035–3054. https://doi.org/10.1785/0120210253

Kawai, K., Takeuchi, N., & Geller, R. J. (2006). Complete synthetic seismograms up to 2 Hz for transversely isotropic spherically symmetric media. *Geophysical Journal International*, *164*(2), 411–424. https://doi.org/10.1111/j.1365-246X.2005.02829.x

Kennett, B. L. N. (2015). Lithosphere-asthenosphere P-wave reflectivity across Australia. *Earth and Planetary Science Letters*. https://doi.org/10.1016/j.epsl.2015.09.039

Kennett, B. L. N., & Sippl, C. (2018). Lithospheric discontinuities in Central Australia. *Tectonophysics*. https://doi.org/10.1016/j.tecto.2018.06.008

Khan, A., & Connolly, J. A. D. (2008). Constraining the composition and thermal state of Mars from inversion of geophysical data. *Journal of Geophysical Research E: Planets*. https://doi.org/10.1029/2007JE002996

Khan, A., Liebske, C., Rozel, A., Rivoldini, A., Nimmo, F., Connolly, J. A. D., et al. (2018). A Geophysical Perspective on the Bulk Composition of Mars. *Journal of Geophysical Research: Planets*. https://doi.org/10.1002/2017JE005371

Khan, A., Ceylan, S., van Driel, M., Giardini, D., Lognonné, P., Samuel, H., et al. (2021). Upper mantle structure of Mars from InSight seismic data. *Science*, *373*(6553), 434–438. https://doi.org/10.1126/science.abf2966

Kiefer, W. S., Bills, B. G., & Steven Nerem, R. (1996). An inversion of gravity and topography for mantle and crustal structure on Mars. *Journal of Geophysical Research E: Planets*. https://doi.org/10.1029/95JE03699

Kim, D., Davis, P., Lekić, V., Maguire, R., Compaire, N., Schimmel, M., et al. (2021). Potential Pitfalls in the Analysis and Structural Interpretation of Mars' Seismic Data from InSight. *Bulletin of the Seismological Society of America*, 1–21. https://doi.org/10.1785/0120210123

Knapmeyer-Endrun, B., & Kawamura, T. (2020). NASA's InSight mission on Mars—first glimpses of the planet's interior from seismology. *Nature Communications*, *11*(1), 1–4. https://doi.org/10.1038/s41467-020-15251-7

Knapmeyer-Endrun, B., Panning, M. P., Bissig, F., Joshi, R., Khan, A., Kim, D., et al. (2021). Thickness and structure of the martian crust from InSight seismic data. *Science*, *373*(6553), 438–443. https://doi.org/10.1126/science.abf8966

Knapmeyer, M., Stähler, S. C., Daubar, I., Forget, F., Spiga, A., Pierron, T., et al. (2021). Seasonal seismic activity on Mars. *Earth and Planetary Science Letters*, *576*, 117171. https://doi.org/10.1016/j.epsl.2021.117171

Korenaga, J. (2014). Teleseismic migration with dual bootstrap stack. *Geophysical*

Journal International, *196*(3), 1706–1723. https://doi.org/10.1093/gji/ggt475

Krischer, L., Megies, T., Barsch, R., Beyreuther, M., Lecocq, T., Caudron, C., & Wassermann, J. (2015). ObsPy: A bridge for seismology into the scientific Python ecosystem. *Computational Science and Discovery*, *8*(1), 014003. https://doi.org/10.1088/1749-4699/8/1/014003

Levshin, A., Ratnikova, L., & Berger, J. (1992). Peculiarities of surface-wave propagation across central Eurasia. *Bulletin - Seismological Society of America*, *82*(6), 2464–2493. https://doi.org/10.1785/bssa0820062464

Li, G., Niu, F., Yang, Y., & Xie, J. (2018). An investigation of time-frequency domain phase-weighted stacking and its application to phase-velocity extraction from ambient noise's empirical Green's functions. *Geophysical Journal International*, *212*(2), 1143–1156. https://doi.org/10.1093/gji/ggx448

Li, Hang, Xu, J., Chen, X., Sun, H., Zhang, M., & Zhang, L. (2020). Extracting long-period surface waves and free oscillations using ambient noise recorded by global distributed superconducting gravimeters. *Seismological Research Letters*, *91*(4), 2234–2246. https://doi.org/10.1785/0220190166

Li, Hongyi, Li, S., Song, X. D., Gong, M., Li, X., & Jia, J. (2012). Crustal and uppermost mantle velocity structure beneath northwestern China from seismic ambient noise tomography. *Geophysical Journal International*, *188*(1), 131–143. https://doi.org/10.1111/j.1365-246X.2011.05205.x

Li, J., Beghein, C., Wookey, J., Davis, P., Lognonné, P., Schimmel, M., et al. (2022). Evidence for crustal seismic anisotropy at the InSight lander site. *Earth and Planetary Science Letters, 593*. https://doi.org/10.1016/j.epsl.2022.117654

Lin, F. C., & Tsai, V. C. (2013). Seismic interferometry with antipodal station pairs. *Geophysical Research Letters*. https://doi.org/10.1002/grl.50907

Lin, F. C., Tsai, V. C., Schmandt, B., Duputel, Z., & Zhan, Z. (2013). Extracting seismic core phases with array interferometry. *Geophysical Research Letters*. https://doi.org/10.1002/grl.50237

Lin, F. C., Tsai, V. C., & Schmandt, B. (2014). 3-D crustal structure of the western United States: Application of Rayleigh-wave ellipticity extracted from noise cross-correlations. *Geophysical Journal International*, *198*(2), 656–670. https://doi.org/10.1093/gji/ggu160

Lognonné, P., Banerdt, W. B., Giardini, D., Pike, W. T., Christensen, U., Laudet, P., et al. (2019). SEIS: Insight's Seismic Experiment for Internal Structure of Mars. *Space Science Reviews*. https://doi.org/10.1007/s11214-018-0574-6

Lognonné, P., Banerdt, W., Pike, W. T., Giardini, D., Christensen, U., Garcia, R. F., et al. (2020). Constraints on the shallow elastic and anelastic structure of Mars from InSight seismic data. *Nature Geoscience*. https://doi.org/10.1038/s41561-020-0536-y

McSween, H. Y., Grove, T. L., & Wyatt, M. B. (2003). Constraints on the composition

and petrogenesis of the Martian crust. *Journal of Geophysical Research E: Planets*. https://doi.org/10.1029/2003je002175

McSween, H. Y., Jeffrey Taylor, G., & Wyatt, M. B. (2009). Elemental composition of the martian crust. *Science*. https://doi.org/10.1126/science.1165871

Miao, W., Niu, F., Li, G., & Levander, A. (2022). Sedimentary and crustal structure of the US Gulf Coast revealed by Rayleigh wave and teleseismic P coda data with implications for continent rifting. *Earth and Planetary Science Letters*, *577*, 117257. https://doi.org/10.1016/j.epsl.2021.117257

Neumann, G. A., Zuber, M. T., Wieczorek, M. A., McGovern, P. J., Lemoine, F. G., & Smith, D. E. (2004). Crustal structure of Mars from gravity and topography. *Journal of Geophysical Research E: Planets*. https://doi.org/10.1029/2004JE002262

Nguyen, L. C., Levander, A., Niu, F., Morgan, J., & Li, G. (2022). Seismic evidence for lithospheric boudinage and its implications for continental rifting. *Geology*. https://doi.org/10.1130/g50046.1

Nishida, K., Montagner, J. P., & Kawakatsu, H. (2009). Global surface wave tomography using seismic hum. *Science, 326*(5949), 112. https://doi.org/10.1126/science.1176389

Nishitsuji, Y., Rowe, C. A., Wapenaar, K., & Draganov, D. (2016). Reflection imaging of the Moon's interior using deep-moonquake seismic interferometry. *Journal of Geophysical Research E: Planets*, *121*(4), 695–713.

https://doi.org/10.1002/2015JE004975

Nishitsuji, Y., Ruigrok, E., & Draganov, D. (2020). Azimuthal Anisotropy of the Megaregolith at the Apollo 14 Landing Site. *Journal of Geophysical Research: Planets*, *125*(5), e2019JE006126. https://doi.org/10.1029/2019JE006126

Niu, F., & Chen, Q. F. (2008). Seismic evidence for distinct anisotropy in the innermost inner core. *Nature Geoscience*, *1*(10), 692–696. https://doi.org/10.1038/ngeo314

Oren, C., & Nowack, R. L. (2017). Seismic body-wave interferometry using noise autocorrelations for crustal structure. *Geophysical Journal International*. https://doi.org/10.1093/gji/ggw394

Pan, Y., Xia, J., Xu, Y., Xu, Z., Cheng, F., Xu, H., & Gao, L. (2016). Delineating shallow S-wave velocity structure using multiple ambient-noise surface-wave methods: An example from Western Junggar, China. *Bulletin of the Seismological Society of America*, *106*(2), 327–336. https://doi.org/10.1785/0120150014

Panning, M. P., Lognonné, P., Bruce Banerdt, W., Garcia, R., Golombek, M., Kedar, S., et al. (2017). Planned Products of the Mars Structure Service for the InSight Mission to Mars. *Space Science Reviews*. https://doi.org/10.1007/s11214-016-0317-5

Parro, L. M., Jiménez-Díaz, A., Mansilla, F., & Ruiz, J. (2017). Present-day heat flow model of Mars. *Scientific Reports*. https://doi.org/10.1038/srep45629

Phạm, T. S., & Tkalčić, H. (2017). On the feasibility and use of teleseismic P wave coda autocorrelation for mapping shallow seismic discontinuities. *Journal of Geophysical*

Research: Solid Earth, *122*(5), 3776–3791. https://doi.org/10.1002/2017JB013975

Phạm, T. S., & Tkalčić, H. (2018). Antarctic Ice Properties Revealed From Teleseismic P Wave Coda Autocorrelation. *Journal of Geophysical Research: Solid Earth*. https://doi.org/10.1029/2018JB016115

Phạm, T. S., & Tkalčić, H. (2021). Constraining Floating Ice Shelf Structures by Spectral Response of Teleseismic P-Wave Coda: Ross Ice Shelf, Antarctica. *Journal of Geophysical Research: Solid Earth*, *126*(4), e2020JB021082. https://doi.org/10.1029/2020JB021082

Qin, L., Ben-Zion, Y., Bonilla, L. F., & Steidl, J. H. (2020). Imaging and Monitoring Temporal Changes of Shallow Seismic Velocities at the Garner Valley Near Anza, California, Following the M7.2 2010 El Mayor-Cucapah Earthquake. *Journal of Geophysical Research: Solid Earth*, *125*(1). https://doi.org/10.1029/2019JB018070

Qiu, H., Lin, F. C., & Ben-Zion, Y. (2019). Eikonal Tomography of the Southern California Plate Boundary Region. *Journal of Geophysical Research: Solid Earth*, *124*(9), 9755–9779. https://doi.org/10.1029/2019JB017806

Qiu, H., Hillers, G., & Ben-Zion, Y. (2020). Temporal changes of seismic velocities in the San Jacinto Fault zone associated with the 2016 Mw 5.2 Borrego Springs earthquake. *Geophysical Journal International*, *220*(3), 1536–1554. https://doi.org/10.1093/gji/ggz538

Qiu, H., Niu, F., & Qin, L. (2021). Denoising Surface Waves Extracted From Ambient

Noise Recorded by 1-D Linear Array Using Three-Station Interferometry of Direct Waves. *Journal of Geophysical Research: Solid Earth*, *126*(8), e2021JB021712. https://doi.org/10.1029/2021JB021712

Rivoldini, A., Van Hoolst, T., Verhoeven, O., Mocquet, A., & Dehant, V. (2011). Geodesy constraints on the interior structure and composition of Mars. *Icarus*. https://doi.org/10.1016/j.icarus.2011.03.024

Romero, P., & Schimmel, M. (2018). Mapping the Basement of the Ebro Basin in Spain With Seismic Ambient Noise Autocorrelations. *Journal of Geophysical Research: Solid Earth*, *123*(6), 5052–5067. https://doi.org/10.1029/2018JB015498

Schimmel, M., & Gallart, J. (2007). Frequency-dependent phase coherence for noise suppression in seismic array data. *Journal of Geophysical Research: Solid Earth*, *112*(4), 1–14. https://doi.org/10.1029/2006JB004680

Schimmel, M., & Paulssen, H. (1997). Noise reduction and detection of weak, coherent signals through phase-weighted stacks. *Geophysical Journal International*. https://doi.org/10.1111/j.1365-246X.1997.tb05664.x

Schimmel, M., Stutzmann, E., & Gallart, J. (2011). Using instantaneous phase coherence for signal extraction from ambient noise data at a local to a global scale. *Geophysical Journal International*, *184*(1), 494–506. https://doi.org/10.1111/j.1365-246X.2010.04861.x

Schimmel, M., Stutzmann, E., & Ventosa, S. (2018). Low-frequency ambient noise

autocorrelations: Waveforms and normal modes. *Seismological Research Letters*, *89*(4), 1488–1496. https://doi.org/10.1785/0220180027

Schimmel, M., Stutzmann, E., Lognonné, P., Compaire, N., Davis, P., Drilleau, M., et al. (2021). Seismic Noise Autocorrelations on Mars. *Earth and Space Science*, *8*(6), 1–22. https://doi.org/10.1029/2021EA001755

Scholz, J. R., Widmer-Schnidrig, R., Davis, P., Lognonné, P., Pinot, B., Garcia, R. F., et al. (2020). Detection, Analysis, and Removal of Glitches From InSight's Seismic Data From Mars. *Earth and Space Science*, *7*(11), e2020EA001317. https://doi.org/10.1029/2020EA001317

Schumacher, S., & Breuer, D. (2006). Influence of a variable thermal conductivity on the thermochemical evolution of Mars. *Journal of Geophysical Research E: Planets*. https://doi.org/10.1029/2005JE002429

She, Y., Yao, H., Yang, H., Wang, J., & Feng, J. (2022). Constraining the depth extent of low-velocity zone along the Chenghai Fault by dense array ambient noise interferometry and horizontal-to-vertical spectral ratio. *Tectonophysics*, *827*, 229265. https://doi.org/10.1016/j.tecto.2022.229265

Shearer, P. M. (2019). *Introduction to Seismology*. *Introduction to Seismology*. https://doi.org/10.1017/9781316877111

Shen, W., Ritzwoller, M. H., & Schulte-Pelkum, V. (2013). A 3-D model of the crust and uppermost mantle beneath the Central and Western US by joint inversion of receiver

functions and surface wave dispersion. *Journal of Geophysical Research: Solid Earth*, *118*(1), 262–276. https://doi.org/10.1029/2012JB009602

Shirzad, T., & Shomali, Z. H. (2014). Shallow crustal radial anisotropy beneath the Tehran basin of Iran from seismic ambient noise tomography. *Physics of the Earth and Planetary Interiors*, *231*, 16–29. https://doi.org/10.1016/j.pepi.2014.04.001

Smrekar, S. E., Lognonné, P., Spohn, T., Banerdt, W. B., Breuer, D., Christensen, U., et al. (2019). Pre-mission InSights on the Interior of Mars. *Space Science Reviews*. https://doi.org/10.1007/s11214-018-0563-9

Sohl, F., & Spohn, T. (1997). The interior structure of Mars: Implications from SNC meteorites. *Journal of Geophysical Research E: Planets*. https://doi.org/10.1029/96JE03419

Stähler, S. C., Khan, A., Bruce Banerdt, W., Lognonné, P., Giardini, D., Ceylan, S., et al. (2021). Seismic detection of the martian core. *Science*, *373*(6553), 443–448. https://doi.org/10.1126/science.abi7730

Stewart, A. J., Schmidt, M. W., Van Westrenen, W., & Liebske, C. (2007). Mars: A new core-crystallization regime. *Science*. https://doi.org/10.1126/science.1140549

Stutzmann, E., Schimmel, M., Lognonné, P., Horleston, A., Ceylan, S., van Driel, M., et al. (2021). The Polarization of Ambient Noise on Mars. *Journal of Geophysical Research: Planets*, *126*(1), 1–27. https://doi.org/10.1029/2020JE006545

Suemoto, Y., Ikeda, T., & Tsuji, T. (2020). Temporal Variation and Frequency

Dependence of Seismic Ambient Noise on Mars From Polarization Analysis. *Geophysical Research Letters*, *47*(13), 1–9. https://doi.org/10.1029/2020GL087123

Sun, W., & Tkalčić, H. (2022). Repetitive marsquakes in Martian upper mantle. *Nature Communications*, *13*(1). https://doi.org/10.1038/s41467-022-29329-x

Takeuchi, N., Geller, R. J., & Cummins, P. R. (1996). Highly accurate P-SV complete synthetic seismograms using modified DSM operators. *Geophysical Research Letters*, *23*(10), 1175–1178. https://doi.org/10.1029/96GL00973

Thurber, C. H., & Toksöz, M. N. (1978). Martian lithospheric thickness from elastic flexure theory. *Geophysical Research Letters*. https://doi.org/10.1029/GL005i011p00977

Tibuleac, I. M., & von Seggern, D. (2012). Crust-mantle boundary reflectors in Nevada from ambient seismic noise autocorrelations. *Geophysical Journal International*. https://doi.org/10.1111/j.1365-246X.2011.05336.x

Tkalčić, H., & Pham, T. S. (2018). Shear properties of Earth's inner core constrained by a detection of J waves in global correlation wavefield. *Science*. https://doi.org/10.1126/science.aau7649

Verhoeven, O., Rivoldini, A., Vacher, P., Mocquet, A., Choblet, G., Menvielle, M., et al. (2005). Interior structure of terrestrial planets: Modeling Mars' mantle and its electromagnetic, geodetic, and seismic properties. *Journal of Geophysical Research E: Planets*. https://doi.org/10.1029/2004JE002271

Wang, T., Song, X., & Xia, H. H. (2015). Equatorial anisotropy in the inner part of Earth's inner core from autocorrelation of earthquake coda. *Nature Geoscience*. https://doi.org/10.1038/ngeo2354

Wookey, J., & Helffrich, G. (2008). Inner-core shear-wave anisotropy and texture from an observation of PKJKP waves. *Nature*, *454*(7206), 873–876. https://doi.org/10.1038/nature07131

Xie, Jinyun, Yang, Y., & Luo, Y. (2020). Improving cross-correlations of ambient noise using an rms-ratio selection stacking method. *Geophysical Journal International*, *222*(2), 989–1002. https://doi.org/10.1093/gji/ggaa232

Xie, Jun, & Ni, S. (2019). Imaging 3D upper-mantle structure with autocorrelation of seismic noise recorded on a transportable single station. *Seismological Research Letters*, *90*(2 A), 708–715. https://doi.org/10.1785/0220180260

Xu, F., Siersch, N. C., Gréaux, S., Rivoldini, A., Kuwahara, H., Kondo, N., et al. (2021). Low Velocity Zones in the Martian Upper Mantle Highlighted by Sound Velocity Measurements. *Geophysical Research Letters*, *48*(19), e2021GL093977. https://doi.org/10.1029/2021gl093977

Yan, P., Li, Z., Li, F., Yang, Y., & Hao, W. (2019). Antarctic ice-sheet structures retrieved from P-wave coda autocorrelation method and comparisons with two other single-station passive seismic methods. *Journal of Glaciology*, *66*(255), 153–165. https://doi.org/10.1017/jog.2019.95

Yao, H., van der Hilst, R. D., & de Hoop, M. V. (2006). Surface-wave array tomography in SE Tibet from ambient seismic noise and two-station analysis - I. Phase velocity maps. *Geophysical Journal International*, *166*(2), 732–744. https://doi.org/10.1111/j.1365-246X.2006.03028.x

Yao, H., Beghein, C., & Van Der Hilst, R. D. (2008). Surface wave array tomography in SE Tibet from ambient seismic noise and two-station analysis - II. Crustal and upper-mantle structure. *Geophysical Journal International*, *173*(1), 205–219. https://doi.org/10.1111/j.1365-246X.2007.03696.x

Yilmaz, Ö. (2001). *Seismic Data Analysis*. *Seismic Data Analysis* (Vol. 10). https://doi.org/10.1190/1.9781560801580

Yoder, C. F., Konopliv, A. S., Yuan, D. N., Standish, E. M., & Folkner, W. M. (2003). Fluid core size of Mars from detection of the solar tide. *Science*. https://doi.org/10.1126/science.1079645

Yoshizaki, T., & McDonough, W. F. (2020). The composition of Mars. *Geochimica et Cosmochimica Acta*, *273*, 137–162. https://doi.org/10.1016/j.gca.2020.01.011

Zeng, X., Lancelle, C., Thurber, C., Fratta, D., Wang, H., Lord, N., et al. (2017). Properties of noise cross-correlation functions obtained from a distributed acoustic sensing array at Garner Valley, California. *Bulletin of the Seismological Society of America*, *107*(2), 603–610. https://doi.org/10.1785/0120160168

Zhan, Z., Ni, S., Helmberger, D. V., & Clayton, R. W. (2010). Retrieval of Moho-

reflected shear wave arrivals from ambient seismic noise. *Geophysical Journal International*. https://doi.org/10.1111/j.1365-246X.2010.04625.x

Zhang, Y., Yao, H., Yang, H. Y., Cai, H. T., Fang, H., Xu, J., et al. (2018). 3-D Crustal Shear-Wave Velocity Structure of the Taiwan Strait and Fujian, SE China, Revealed by Ambient Noise Tomography. *Journal of Geophysical Research: Solid Earth*, *123*(9), 8016–8031. https://doi.org/10.1029/2018JB015938

Zharkov, V. N., Gudkova, T. V., & Molodensky, S. M. (2009). On models of Mars' interior and amplitudes of forced nutations. 1. The effects of deviation of Mars from its equilibrium state on the flattening of the core-mantle boundary. *Physics of the Earth and Planetary Interiors*. https://doi.org/10.1016/j.pepi.2008.10.009

Zhou, J., & Zhang, W. (2021). Extracting Reliable P-Wave Reflections From Teleseismic P Wave Coda Autocorrelation. *Journal of Geophysical Research: Solid Earth*, *126*(11). https://doi.org/10.1029/2021JB022064

Zuber, M. T. (2000). Internal structure and early thermal evolution of Mars from Mars global surveyor topography and gravity. *Science*, *287*(5459), 1788–1793. https://doi.org/10.1126/science.287.5459.1788

Zuber, M. T. (2001). The crust and mantle of Mars. *Nature*. https://doi.org/10.1038/35084163

InSight Mars SEIS Data Service. (2019). SEIS raw data, Insight Mission. IPGP, JPL, CNES, ETHZ, ICL, MPS, ISAE-Supaero, LPG, MFSC.

https://doi.org/10.18715/SEIS.INSIGHT.XB_2016

Appendix A: Supporting Information for Chapter 3

Text A1 - Parameter Test for Glitch Detection and Removal

We applied the open-source software SEISglitch (Scholz et al., 2020) to detect and remove the high-amplitude glitches within the raw InSight (Interior Exploration Using Seismic Investigations, Geodesy and Heat Transport) seismic data. The stacked autocorrelation of the deglitched waveform can clearly recover the body-wave reflection responses from olivine-wadsleyite transition and core-mantle boundary (Figure A2). Here we designed a parameter test of the SEISglitch software to demonstrate the robustness of the data processing procedures.

Two SEISglitch parameters, glitch-detection amplitude threshold (hereafter referred as “threshold”) and minimum glitch polarization value (hereafter referred as “glitch_min_polarization”), were tuned to compare with the autocorrelation results in Figure A2. The details of threshold and glitch_min_polarization are shown in Scholz et al. (2020) and SEISglitch webpage (https://seisglitch.readthedocs.io/en/latest/index.html). When threshold and glitch_min_polarization are small, it represents more lax parameter settings and more glitches will be detected, and vice versa. Here we set relatively lower threshold and glitch_min_polarization values (Table A1) to detect ~40% - 100% more glitches than the results shown in Figure 3.1. Figure A1 illustrates the raw and deglitched waveforms with more lax parameter settings. Then we followed the same processing steps shown in the main article to calculate each 4-hour autocorrelogram and sum them

together with both linear stacking (LS) and phase-weighted stacking (PWS) (Schimmel & Paulssen, 1997). Figure A2 compares the LS and PWS stacked autocorrelation of raw, deglitched and glitch-only datasets with laxer SEISglitch parameter settings. Two clear signals at ~285 s and ~385 s can be observed on the autocorrelation of deglitched waveforms but cannot be observed on the autocorrelation of glitch-only waveforms. The results shown in Figure A2 are almost identical as Figure 3.2, which suggests the impact of SEISglitch parameter selection can be negligible.

	threshold (m/s^3)	glitch_min_polarization
Figure 1	0.25×10^{-9}	0.91
Figure S1	0.1×10^{-9}	0.87

Table A1. Threshold and glitch_min_polarization values used for the glitch detection and removal shown in Figures 3.1 and A1

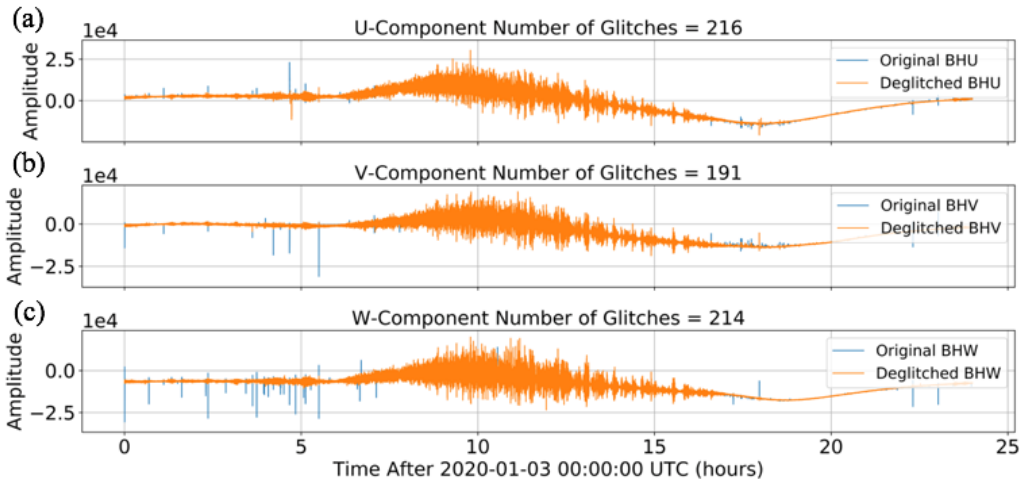

Figure A1. (a) Comparison between the original and deglitched BHU-component recordings on January 3rd, 2020. Same as Figure 1a but with laxer SEISglitch parameter selections (Table A1). (b) Same as (a) but for BHV-component. (c) Same as (a) but for BHW-component.

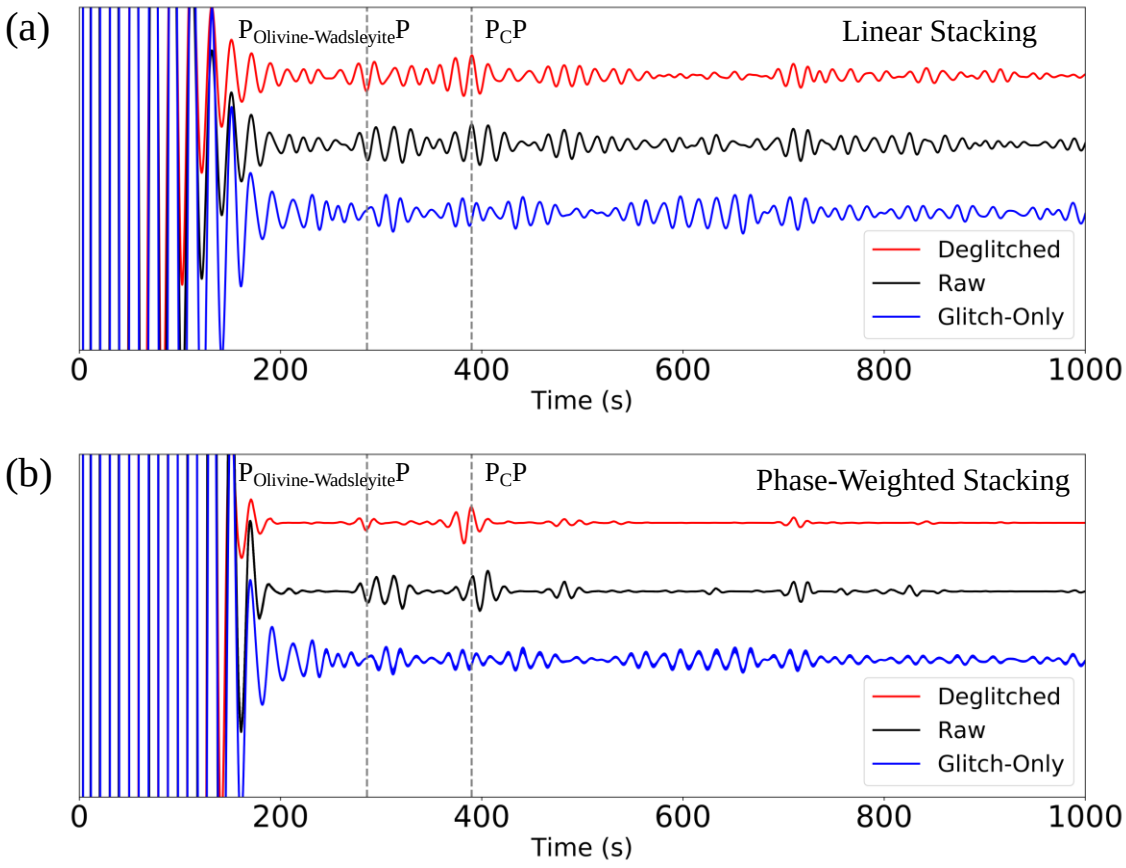

Figure A2. (a) Linearly stacked (LS) vertical-component autocorrelation filtered between 0.05 and 0.1Hz using raw (black), deglitched (red) and glitch-only (blue) data. Same as Figure 3.2a but with laxer SEISglitch parameter selections (Table A1). (b) Same as (a) but for phase-weighted stacking (PWS) (Schimmel & Paulssen, 1997)

Text A2 - Comparison with the stacked autocorrelation using daytime and nighttime ambient noise data

We divided the deglitched data into two subsets, daytime and nighttime deglitched ambient noise recordings. In most cases, the nighttime data are quieter than the daytime data as the wind-generated noise is strong during daytime (Scholz et al., 2020). We followed the same autocorrelation method in the main article to process two deglitched subsets independently and compared the results (Figure A3). Two prominent phases at ~285 and ~385s can be clearly retrieved by both subsets (Figure A3), which indicate the robustness of the processing method.

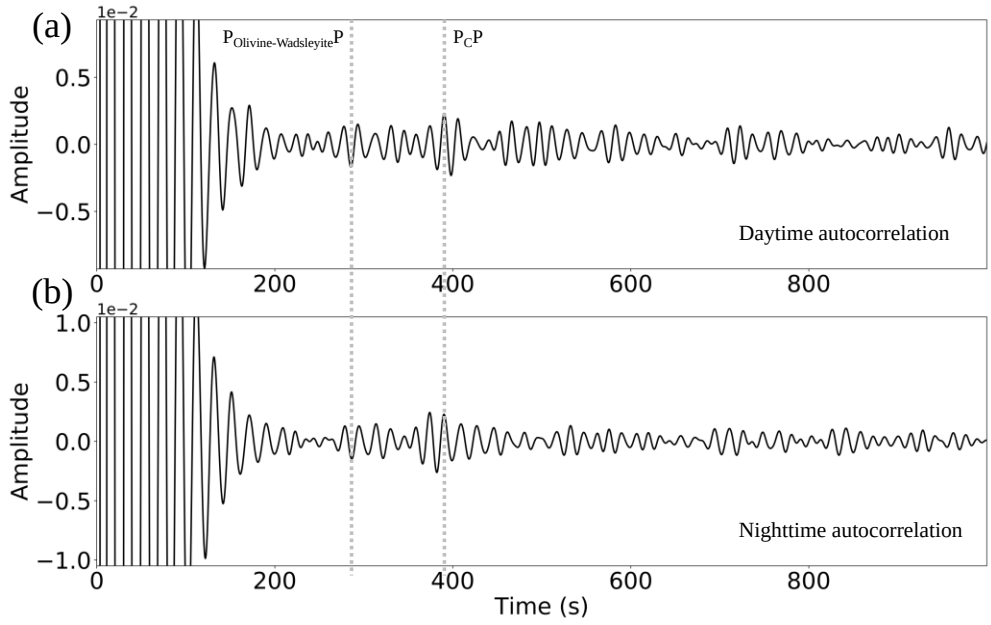

Figure A3. (a) Linearly stacked autocorrelation of the deglitched ambient noise data recorded during Martian daytime. (b) Linearly stacked autocorrelation of the deglitched ambient noise data recorded during Martian nighttime. Two signals at ~285s and ~385s, interpreted as the P-wave reflection response from olivine-

wadsleyite transition and core-mantle boundary, can be clearly retrieved by two subsets.

Text A3 – Bootstrap Calculations

We performed the bootstrap calculations for the autocorrelograms of deglitched ambient noise data to determine whether the results are robust or not. We randomly selected ~80% of 6190 4-hour autocorrelograms of deglitched waveforms (4950 4-hour autocorrologrames) and followed the same data processing procedures as Figure 2b to derive autocorrelation reflectivity series. This step will be repeated for 30 times. Figure S4 shows the PWS stacked autocorrelations using 30 different subsets, where the reflection signals from olivine-wadsleyite transition and core-mantle boundary can be clearly retrieved for all subsets. It further proves our autocorrelation processing is not biased.

Figure A4. Bootstrap calculations for the autocorrelograms of deglitched ambient noise recordings filtered between 0.05 and 0.1 Hz, which followed the same processing steps as Figure 2b. Each bootstrap sample takes around 80% of whole dataset (4950 4-hour autocorrelograms of deglitched waveforms). The gray dashed lines mark the location of interpreted P-wave reflection signals from olivine-wadsleyite transition and core-mantle boundary

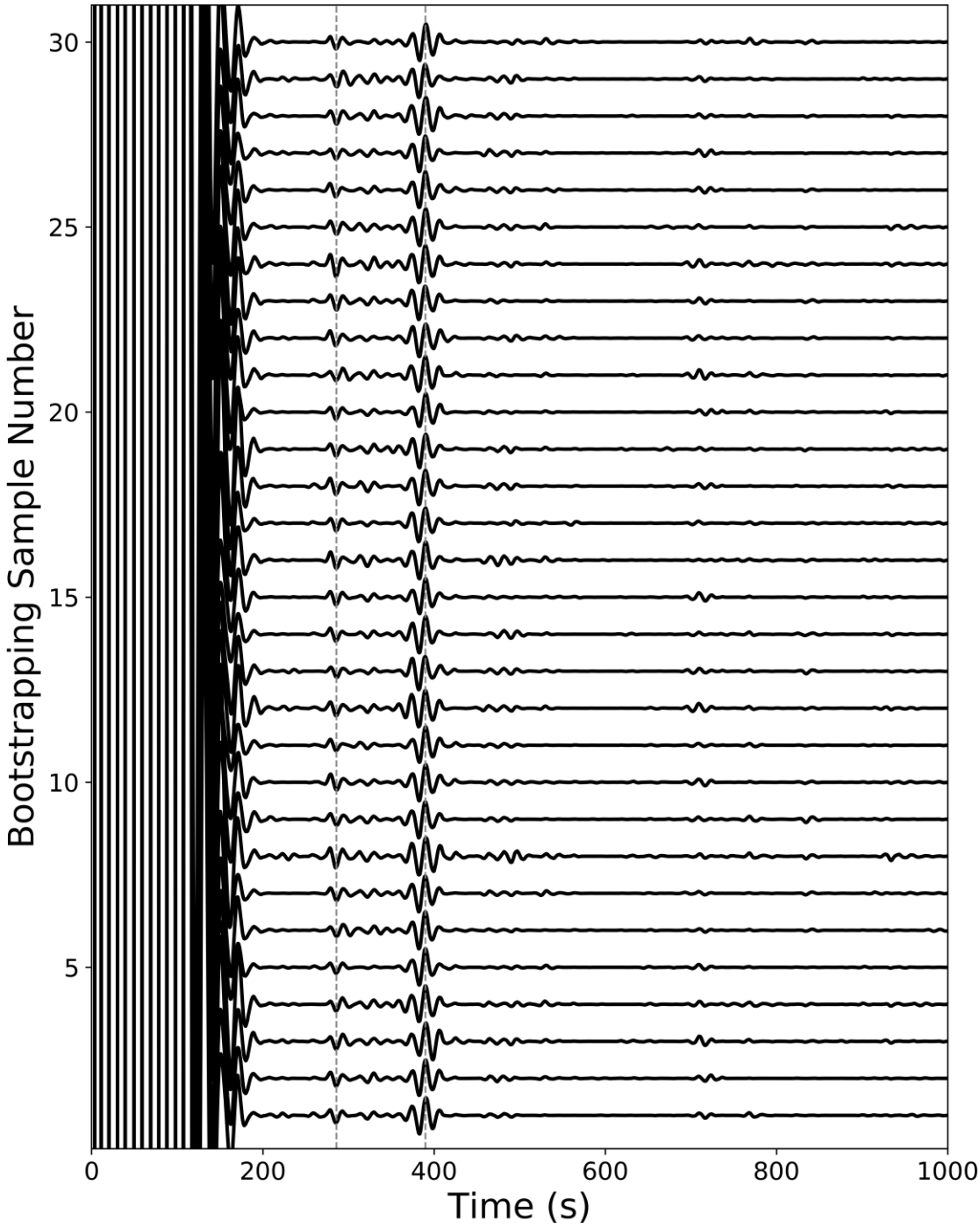
Bootstrapping Sample Number
30
25
20
15
10
5
0
200
400
600
800
1000
Time (s)

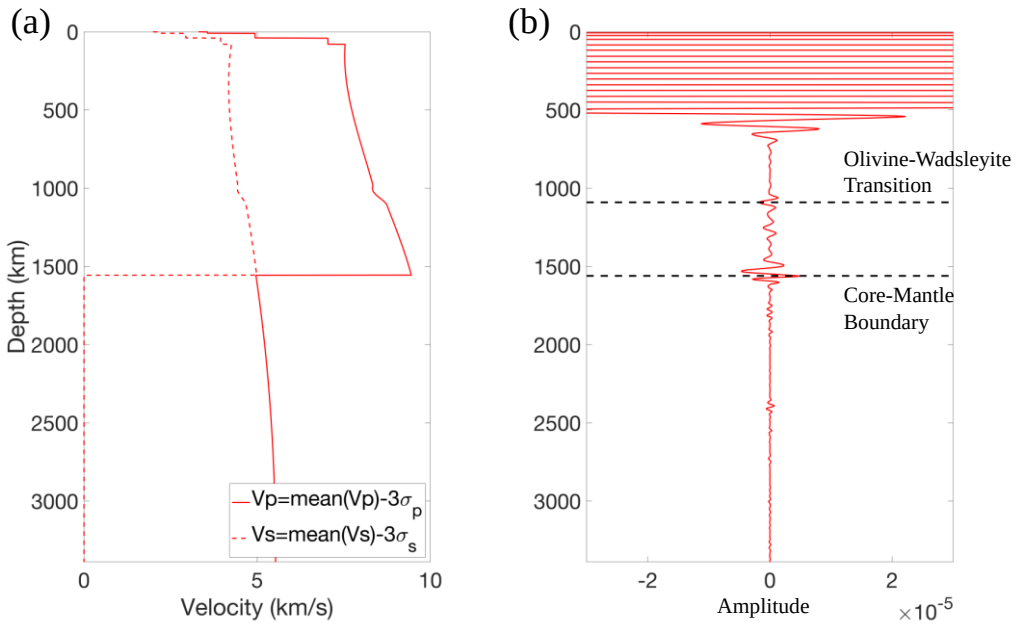

Figure A5. (a) The velocity model that is 3 standard deviations lower than the mean model of Stähler et al. (2021), which is the best fit model for the observed PcP phase among Stähler et al. (2021) suite of models (Figure 3.3b). (b) Depth conversion of the autocorrelation of deglitched ambient noise data (Red trace in Figure 3.2b). The black dashed lines mark the depth location of interpreted olivine-wadsleyite transition and core-mantle boundary. The depth of olivine-wadsleyite transition is mapped at ~1090km.

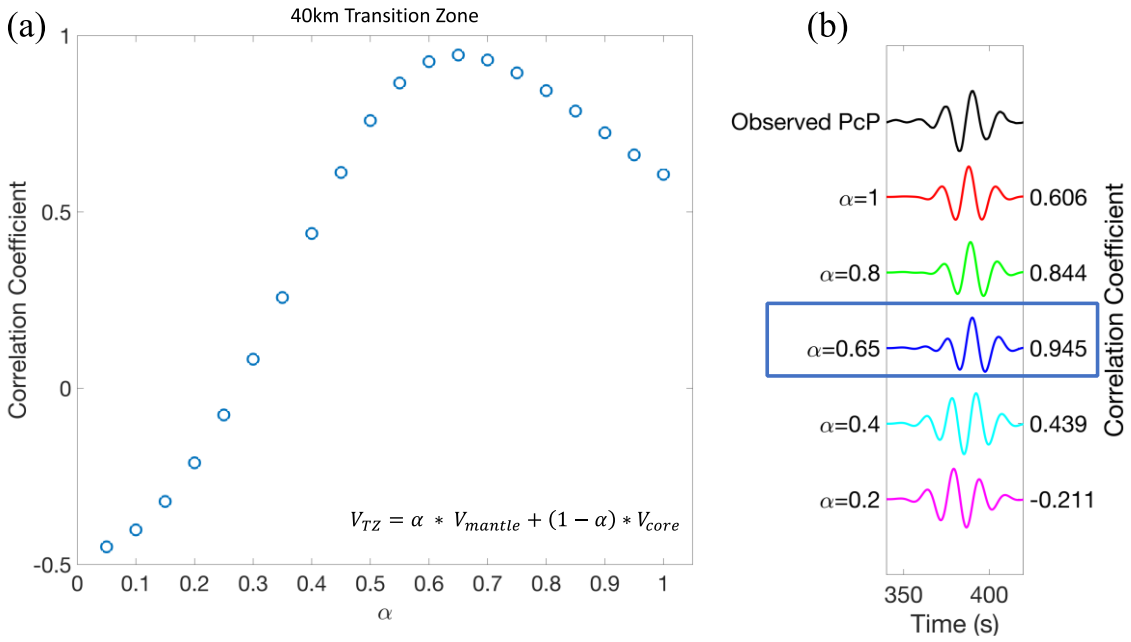

Figure A6. (a) Correlation Coefficient between the observed PcP phase (Red curve in Figure 3.2b) and synthetic PcP phase for different transition zone velocities V_{TZ} of 40km thick CMB transition zone model. (b) The comparison between the synthetic PcP phase of the velocity models shown in (a) and the observed PcP phase. The correlation coefficients between the synthetic and observed PcP are shown on the right side. The blue box marks the model with highest correlation coefficient among all models shown in (a).

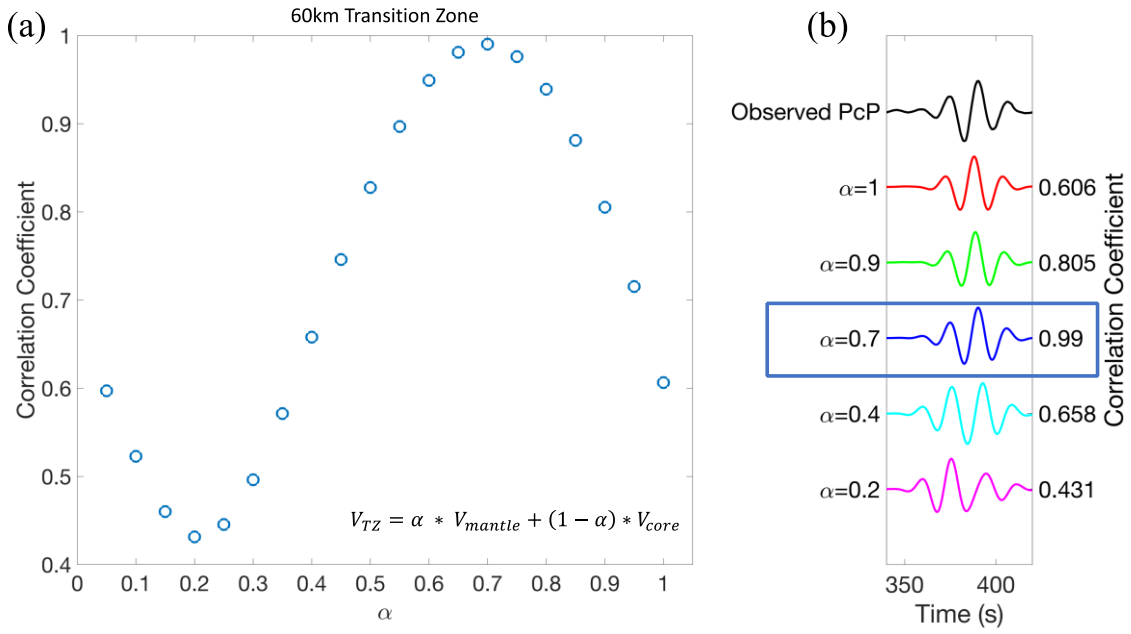

Figure A7. (a) Correlation Coefficient between the observed PcP phase (Red curve in Figure 3.2b) and synthetic PcP phase for different transition zone velocities V_{TZ} of 60km thick CMB transition zone model. (b) The comparison between the synthetic PcP phase of the velocity models shown in (a) and the observed PcP phase. The correlation coefficients between the synthetic and observed PcP are shown on the right side. The blue box marks the model with highest correlation coefficient among all models shown in (a).

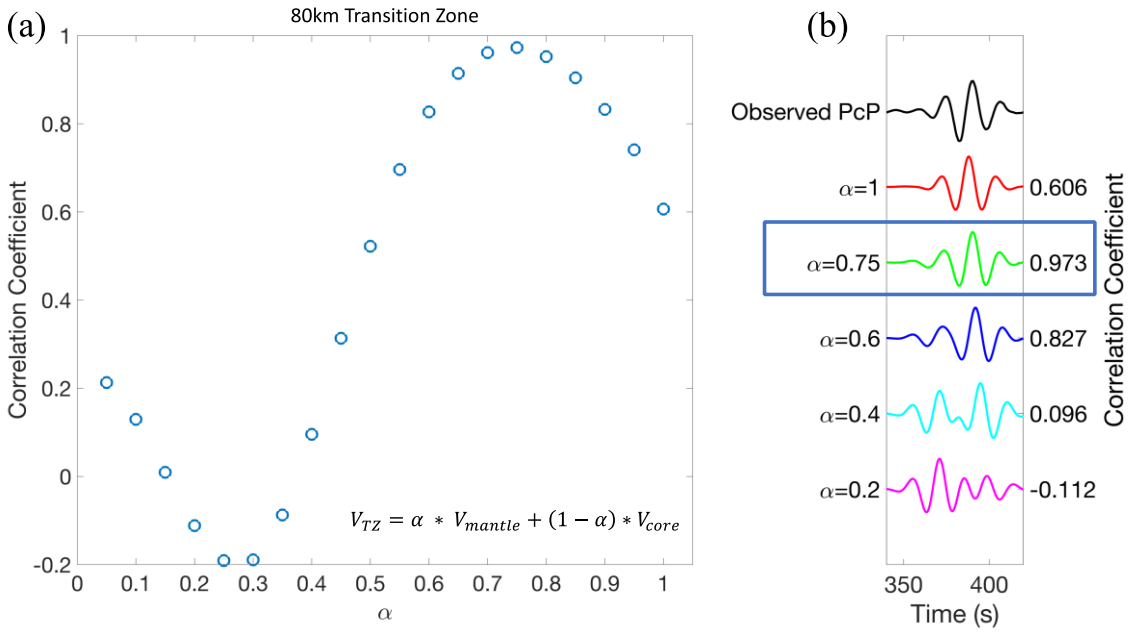

Figure A8. (a) Correlation Coefficient between the observed PcP phase (Red curve in Figure 3.2b) and synthetic PcP phase for different transition zone velocities V_{TZ} of 80km thick CMB transition zone model. (b) The comparison between the synthetic PcP phase of the velocity models shown in (a) and the observed PcP phase. The correlation coefficients between the synthetic and observed PcP are shown on the right side. The blue box marks the model with highest correlation coefficient among all models shown in (a).

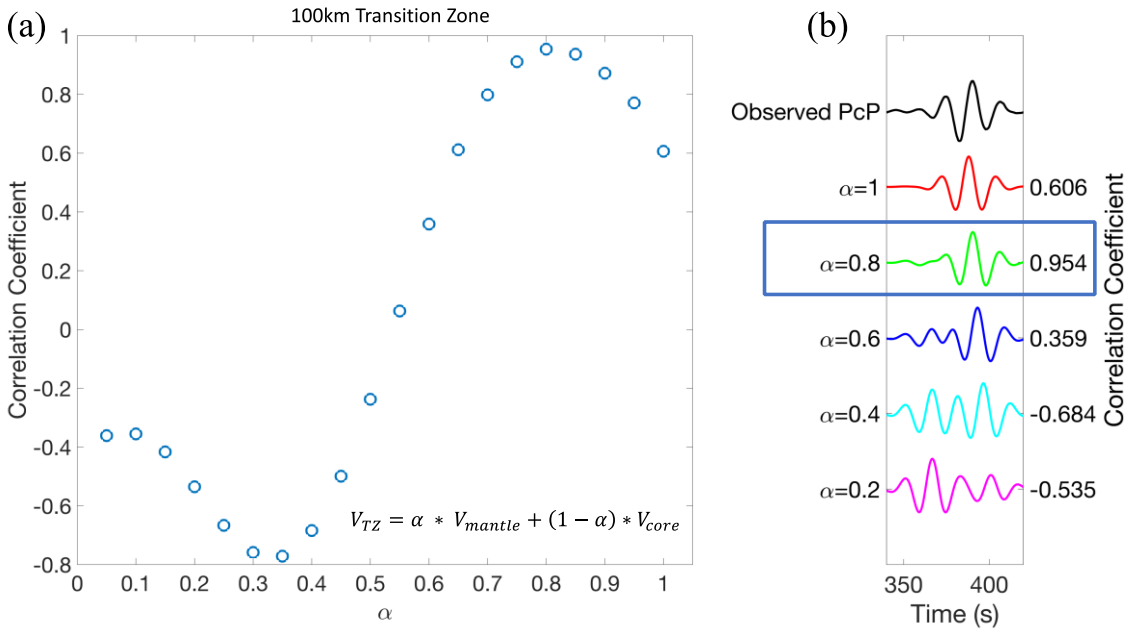

Figure A9. (a) Correlation Coefficient between the observed PcP phase (Red curve in Figure 3.2b) and synthetic PcP phase for different transition zone velocities V_{TZ} of 100km thick CMB transition zone model. (b) The comparison between the synthetic PcP phase of the velocity models shown in (a) and the observed PcP phase. The correlation coefficients between the synthetic and observed PcP are shown on the right side. The blue box marks the model with highest correlation coefficient among all models shown in (a).

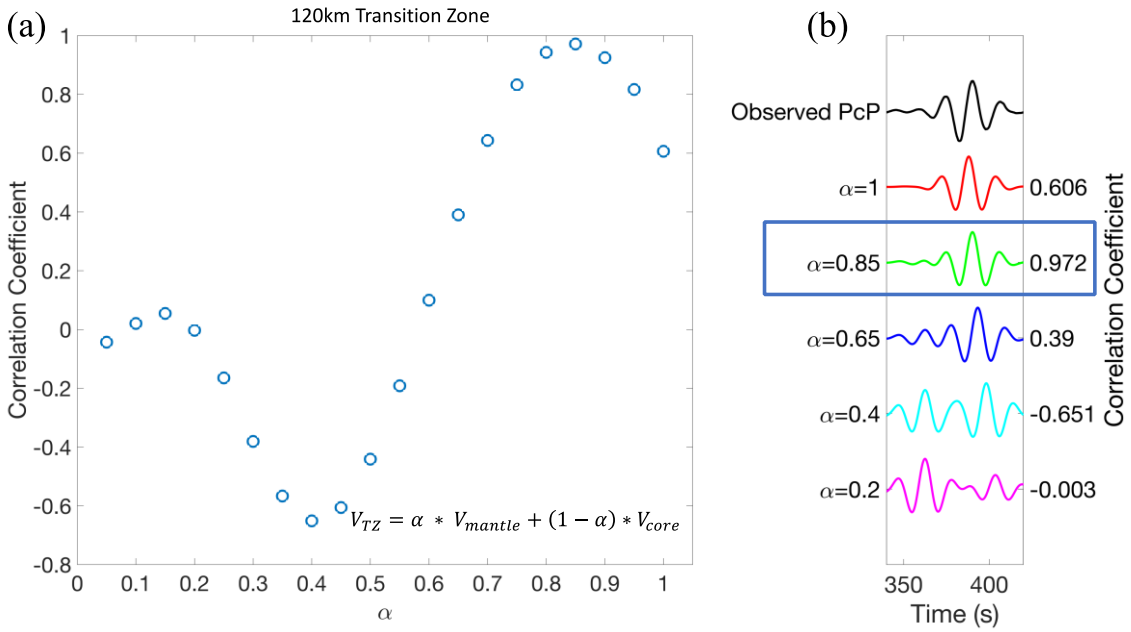

Figure A10. (a) Correlation Coefficient between the observed PcP phase (Red curve in Figure 3.2b) and synthetic PcP phase for different transition zone velocities V_{TZ} of 120km thick CMB transition zone model. (b) The comparison between the synthetic PcP phase of the velocity models shown in (a) and the observed PcP phase. The correlation coefficients between the synthetic and observed PcP are shown on the right side. The blue box marks the model with highest correlation coefficient among all models shown in (a).

Data Availability Statement

The InSight seismic data (InSight Mars SEIS Data Service, 2019) used in this thesis are available on IRIS (Incorporated Research Institutions for Seismology) data center (https://www.iris.edu/hq/sis/insight). The open-source Python package SEISglitch (Scholz et al., 2020) can be installed following the instructions (https://seisglitch.readthedocs.io/en/latest/). The temperature data on Mars were downloaded from The Geosciences Node of NASA's Planetary Data System (PDS) website (https://pds-geosciences.wustl.edu/insight/urn-nasa-pds-insight_rad/data_derived/). The windspeed data were acquired from InSight weather station page (https://atmos.nmsu.edu/data_and_services/atmospheres_data/INSIGHT/insight.html). The synthetic group dispersion curves of spherically symmetric velocity models were calculated by Computer Programs in Seismology (CPS) (Herrmann, 2013). The direct solution method (DSM) software (Kawai et al., 2006) can be accessed at the following URL (http://www-solid.eps.s.u-tokyo.ac.jp/~dsm/software/software.htm). Several procedures used Obspy (Krischer et al., 2015) to process the seismic data.